HUHEPL-19

Measurement of Neutral B Meson Properties

A Ph.D. Thesis by
Michael Stephen Saulnier

Harvard University
High Energy Physics Laboratory
Cambridge, Massachusetts
May 1995

Measurements of Neutral B Meson Properties

A thesis presented

by

Michael Stephen Saulnier

to

The Department of Physics

in partial fulfillment of the requirements

for the degree of

Doctor of Philosophy

in the subject of

Physics

Harvard University

Cambridge, Massachusetts

May 1995

Measurements of Neutral B Meson Properties

by Michael Stephen Saulnier

Under the supervision of Professor Kay Kinoshita

ABSTRACT

Using data recorded by the CLEO II detector operating at the $\Upsilon(4S)$ resonance at the Cornell Electron Storage Ring, two properties of the neutral B_d meson are measured using a partially reconstructed tag of the decay mode $\overline{B_d^0} \rightarrow D^{*+}\ell^-\bar{\nu}$. Using 951 pb^{-1} of on-resonance data, the B_d^0 mixing parameter is found to be $\chi_d = 0.149 \pm 0.023 \pm 0.019 \pm 0.010$ where the third error is due to the uncertainty in the relative contributions of charged and neutral B events to the data sample. With a larger dataset of 1350 pb^{-1}, the B_d^0 semileptonic branching fraction is measured to be $(10.5 \pm 0.8 \pm 1.3)\%$. This result is combined with other similarly tagged semileptonic branching fraction measurements from CLEO, yielding a lifetime ratio $\tau^+/\tau^0 = 0.93 \pm 0.18 \pm 0.12$, assuming equality of semileptonic partial widths.

This one's for Hashi.

Acknowledgements

The author of this thesis is a member of a collaborative experiment. The results presented here are the fruits of the labors of many, not simply his own. Here credit is given to those whose perspiration directly contributed to the results presented herein.

Prof. Kay Kinoshita conceived the mixing analysis of Chapter 4. This measurement was made earlier in the author's graduate career, and both her insight and oversight were essential in order to see the result to completion. Much of the treatment of the systematic errors of the Chapter 4 resulted from the careful scrutinization of the analysis by Prof. Ed Thorndike. The author is grateful to Prof. Ritchie Patterson for supplying the code to create Figure 4.19.

The $\overline{B^0}$ semileptonic branching fraction measurement of Chapter 5 can be more appropriately identified as the results of the author's own hand. Dr. Roy Wang played a crucial role having done the difficult work of determining the lepton fake rates, generating the theoretical spectra, and writing the code to calculate the lepton efficiencies. Dr. Gerald Eigen is to be credited with the recognition of the tagging efficiency bias, and Dr. Peter Kim with proposing the method of quantifying the size of the effect in Monte Carlo. Dr. Mark Lambrecht and Dr. Georges Vasseur cannot be thanked enough for their assistance in unifying the results of the tagged

semileptonic branching fraction measurements, long after they had each moved on to new endeavors in their lives.

Contents

List of Tables

List of Figures

Chapter 1

Introduction

This thesis presents measurements of two different properties of an object called the neutral B meson. The purpose of this introductory chapter is to first present some of the fundamental ideas of particle physics, to then describe what a neutral B meson is, and finally to explain why the two properties are interesting.

1.1 Fundamental Particles

All matter in the universe – the stars above, the earth below, the paper upon which these words are written, and even the person now reading them – are composed of only a few fundamental building blocks.

Electrons (e^-), familiar negatively charged particles which constitute the outermost portion of atoms, are a member of a class of fundamental particles called *leptons*. There also exist two heavier versions of the electron, the muon (μ^-) and the tau (τ^-) which, aside from their larger masses, are identical in all respects to the electron. Three additional leptons with zero electric charge, the neutrinos complete the family of six leptons. Each neutrino is associated with one of the three charged leptons, and are given the names ν_e, ν_μ and ν_τ. The neutrinos appear to be massless and there is currently no direct evidence to suggest otherwise. These six leptons are grouped into three doublets, or generations

$$\begin{pmatrix} \nu_e \\ e \end{pmatrix} \begin{pmatrix} \nu_\mu \\ \mu \end{pmatrix} \begin{pmatrix} \nu_\tau \\ \tau \end{pmatrix} . \tag{1.1}$$

The proton and the neutron, known to compose the nuclei of atoms, are *not* fundamental particles themselves, but are composed of entities called *quarks*. Like the leptons, there are six varieties of quarks which can also be grouped into three doublets with progressively larger masses

$$\begin{pmatrix} u \\ d \end{pmatrix} \begin{pmatrix} c \\ s \end{pmatrix} \begin{pmatrix} t \\ b \end{pmatrix} . \tag{1.2}$$

The up and down quarks comprise the first generation doublet, the charm and strange quarks the second, and the top and bottom quarks comprise the third doublet. The upper member of each quark doublet carries an electric charge equal to $+\frac{2}{3}|e|$, where $|e|$ is the magnitude of the electron charge. The lower members have charge $-\frac{1}{3}|e|$.

Both leptons and quarks are *fermions*, particles which have an intrinsic angular momentum, or spin, of $n\hbar/2$. For quarks and leptons, $n = 1$. Tables 1.1 and 1.2 summarize the charges and masses of the leptons and quarks.

Lepton	Symbol	Charge $Q/\|e\|$	Mass MeV/c^2
Electron	e^-	-1	0.511
Muon	μ^-	-1	105.7
Tau	τ^-	-1	1777
Electron neutrino	ν_e	0	$< 7.0 \times 10^{-6}$
Muon neutrino	ν_μ	0	< 0.27
Tau neutrino	ν_τ	0	< 31

Table 1.1: The six leptons

Quark	Symbol	Charge $Q/\|e\|$	Mass MeV/c^2
Down	d	$-1/3$	4
Up	u	$+2/3$	7
Strange	s	$-1/3$	300
Charm	c	$+2/3$	1300
Bottom (Beauty)	b	$-1/3$	4800
Top (Truth)	t	$+2/3$	174000

Table 1.2: The six quarks

Force	Boson	Symbol	Charge $Q/\|e\|$	Mass (GeV/c^2)
Strong	Gluon	g	0	0
Electromagnetic	Photon	γ	0	0
Weak	W	$W^{\pm}$	± 1	80.2
	Z	Z	0	91.2
Gravitational	Graviton	G	0	0

Table 1.3: The force-mediating intermediate vector bosons

1.2 Fundamental Forces

The quarks and the leptons interact with one other through the exchange of intermediate vector bosons. Such interactions give rise to the four known fundamental forces, the strong, the weak, the electromagnetic, and the gravitational. Each force has one or more intermediate vector bosons which are responsible for its mediation, and they are summarized in Table 1.3.

A quite successful theory, the Standard Model, describes the interactions of the strong, weak and electromagnetic forces, but makes no attempt to account for the gravitational force.[1] The theory is based on the gauge group $SU(3)_{\mathrm{color}} \otimes SU(2)_{\mathrm{L}} \otimes U(1)_{\mathrm{Y}}$. The quarks and leptons are grouped into lefthanded weak-isospin doublets and righthanded singlets.

$$\begin{pmatrix} \nu_e \\ e \end{pmatrix}_L, \begin{pmatrix} \nu_\mu \\ \mu \end{pmatrix}_L, \begin{pmatrix} \nu_\tau \\ \tau \end{pmatrix}_L \quad , \quad e_R,\ \mu_R,\ \tau_R$$

$$\begin{pmatrix} u \\ d' \end{pmatrix}_L, \begin{pmatrix} c \\ s' \end{pmatrix}_L, \begin{pmatrix} t \\ b' \end{pmatrix}_L \quad , \quad u_R,\ c_R,\ t_R,\ d'_R,\ s'_R,\ b'_R.$$

---

[1] The gravitational force has a negligible effect on the results presented in this thesis and it will not be discussed again.

The meaning of the primed quarks d', s' and b' will be explained shortly.

We focus here on the $SU(2)_{\rm L} \otimes U(1)_{\rm Y}$ portion of the gauge group which describes the unified electroweak force acting upon the left-handed doublets. The gauge bosons W^1_μ, W^2_μ and W^3_μ are introduced for $SU(2)_{\rm L}$ and the gauge boson B_μ for $U(1)_{\rm Y}$. The four gauge bosons couple to a scalar Higgs field. Through a spontaneous symmetry breaking mechanism, linear combinations of these massless bosons become the massive W^-, W^+ and Z^0, and also the massless γ. The relationships between the fields are

$$W^\pm_\mu = \frac{1}{\sqrt{2}}(W^1_\mu \pm iW^2_\mu) \tag{1.3}$$

$$Z_\mu = W^3_\mu \cos\theta_W - B_\mu \sin\theta_W \tag{1.4}$$

$$A_\mu = W^3_\mu \sin\theta_W + B_\mu \cos\theta_W \tag{1.5}$$

where θ_W is the Weinberg angle, a fundamental parameter of the electroweak theory.

The portion of the Lagrangian which describes the electroweak interactions can be written as

$$\mathcal{L}^{\rm EW}_{\rm int} = \frac{g_W}{\sqrt{2}}(J^+_\mu W^{+\mu} + J^-_\mu W^{-\mu}) + g_Z(J^0_\mu - \sin^2\theta_W J^{\rm EM}_\mu)Z^\mu + eJ^{\rm EM}_\mu A^\mu \tag{1.6}$$

with

$$g_W = \frac{e}{\sin\theta_W} \tag{1.7}$$

and

$$g_Z = \frac{e}{\sin\theta_W \cos\theta_W} \tag{1.8}$$

where e is the magnitude of the electron's electric charge.

In this thesis, we will be concerned mainly with the physics of the weak charged current, namely those interactions involving the $W^\pm$ bosons. The explicit form for the weak charged current is given for leptons by

$$J^+_\mu = (\bar{\nu}_e, \bar{\nu}_\mu, \bar{\nu}_\tau)\frac{1}{2}\gamma_\mu(1-\gamma^5)\begin{pmatrix} e \\ \mu \\ \tau \end{pmatrix} \tag{1.9}$$

and for quarks by

$$J_\mu^+ = (\bar{u}, \bar{c}, \bar{t})\frac{1}{2}\gamma_\mu(1-\gamma^5)V \begin{pmatrix} d \\ s \\ b \end{pmatrix}. \tag{1.10}$$

where

$$V = \begin{pmatrix} V_{ud} & V_{us} & V_{ub} \\ V_{cd} & V_{cs} & V_{cb} \\ V_{td} & V_{ts} & V_{tb} \end{pmatrix} \tag{1.11}$$

The primed quarks from equation 1.3 are defined as

$$\begin{pmatrix} d' \\ s' \\ b' \end{pmatrix} = V \begin{pmatrix} d \\ s \\ b \end{pmatrix}. \tag{1.12}$$

The matrix V is called the Cabibbo-Kobayashi-Maskawa (CKM) quark mixing matrix. The CKM matrix is not diagonal and therefore allows for interactions between quarks from different generations, unlike the case for leptons. The CKM matrix can be parameterized in terms of four rotation angles θ_1, θ_2, θ_3 and δ as

$$V = \begin{pmatrix} c_1 & -s_1c_3 & -s_1s_3 \\ s_1c_2 & c_1c_2c_3 - s_2s_3e^{i\delta} & c_1c_2s_3 + s_2c_3e^{i\delta} \\ s_1s_2 & c_1s_2c_3 + c_2s_3e^{i\delta} & c_1s_2s_3 - c_2c_3e^{i\delta} \end{pmatrix} \tag{1.13}$$

where $c_i = \cos\theta_i$ and $s_i = \sin\theta_i$[1]. A popular approximation to the CKM matrix is given by

$$\begin{pmatrix} 1-\lambda^2/2 & \lambda & A\lambda^3(\rho - i\eta) \\ -\lambda & 1-\lambda^2/2 & A\lambda^2 \\ A\lambda^3(1-\rho-i\eta) & -A\lambda^2 & 1 \end{pmatrix} \tag{1.14}$$

and is called the Wolfenstein parameterization[2]. The strength of the quark couplings between generations can be understood in terms of powers of the constant $\lambda \simeq 0.22$. The quark couplings are strongest within the same generation, suppressed by a factor of λ between the 2^{nd} and 1^{st} generation, suppressed further as λ^2 between 3^{rd} and 2^{nd} generations, and the weakest λ^3 coupling is between the 3^{rd} and 1^{st} generation quarks.

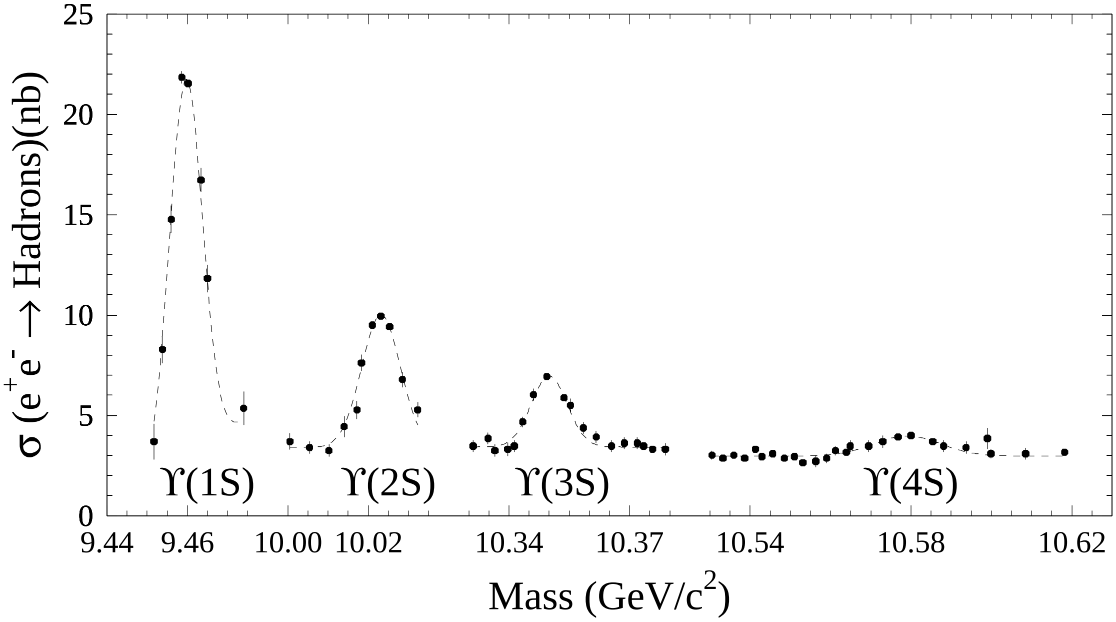

Figure 1.1: The Upsilon Resonances

Based on a global fit to all available data and assuming unitarity of the matrix, the 90% confidence level ranges for the magnitudes of the matrix elements are[3]

$$\begin{pmatrix} 0.9747 & \text{to} & 0.9759 & 0.218 & \text{to} & 0.24 & 0.002 & \text{to} & 0.005 \\ 0.218 & \text{to} & 0.224 & 0.9738 & \text{to} & 0.9752 & 0.032 & \text{to} & 0.048 \\ 0.004 & \text{to} & 0.015 & 0.030 & \text{to} & 0.048 & 0.998 & \text{to} & 0.9995 \end{pmatrix}. \tag{1.15}$$

1.3 B mesons

A B meson is a bound state of a quark-antiquark pair with a bottom quantum number of ±1. The lightest two varieties are the neutral $\overline{B^0}$ composed of a $b\bar{d}$ quark-antiquark pair, and the charged B^- composed of a $b\bar{u}$ pair. A slightly more massive neutral B meson, the B_s ($b\bar{s}$) has been observed at higher energy experiments, but will not be discussed in any great detail in this thesis.

B mesons can be produced by colliding e^+ and e^- at a center of mass energy corresponding to the fourth of the Υ bottomonium ($b\bar{b}$) resonances. Figure 1.1 shows the cross section for the process $e^+e^- \to$ hadrons in the energy region of 10 GeV[4]. The Υ(1S), Υ(2S), and Υ(3S) are relatively narrow resonances corresponding to the $N = 1$, 2 and 3 S-wave states of the bottomonium system. Each of these three resonances is quite narrow, decaying primarily through OZI-suppressed strong decays[5].

The Υ(4S) at 10.58 GeV is the first bottomonium resonance with a mass greater than twice the mass of the $\overline{B^0}$ or the B^- (but not the B_s) meson. Consequently, the reaction

$$e^+e^- \to \gamma^* \to \Upsilon(4\mathrm{S}) \to \overline{B^0}B^0 \text{ or } B^-B^+$$

is allowed to take place, broadening the resonance significantly. The cross section for the above process is approximately 1 nb.

At the energy of the Υ(4S) the virtual photon may not decay to a $b\bar{b}$ pair, but may instead decay into lighter quark-antiquark pair

$$e^+e^- \to \gamma^* \to c\bar{c} \text{ or } s\bar{s} \text{ or } u\bar{u} \text{ or } d\bar{d}$$

which has a cross section of approximately 3 nb. The nonresonant production of light quarks is referred to as *continuum* production. For studies of B mesons, the continuum events are considered to be background. To account for this background, the CLEO experiment operates not only at a center of mass energy of 10.58 GeV, referred to as ON running conditions, but also collects data at an energy about 60 MeV below the Υ(4S), called OFF running conditions. CLEO spends approximately 2/3 of the time collecting ON data, and 1/3 collecting OFF data. After scaling the OFF data by a factor to correct for the differences in energy and integrate luminosity, the OFF results are subtracted from the ON.

B mesons decay through the quark-level transition $b \to cW^-$ or the more suppressed transition $b \to uW^-$. The first-order feynman diagrams are shown in Fig-

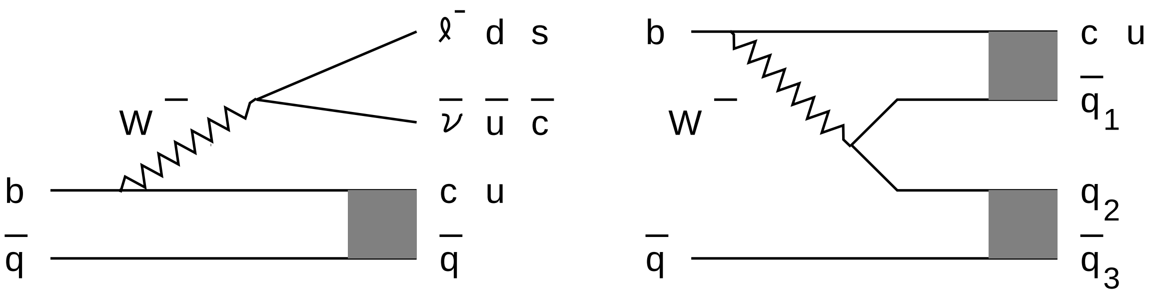

(a) Spectator

(b) Color Mixed

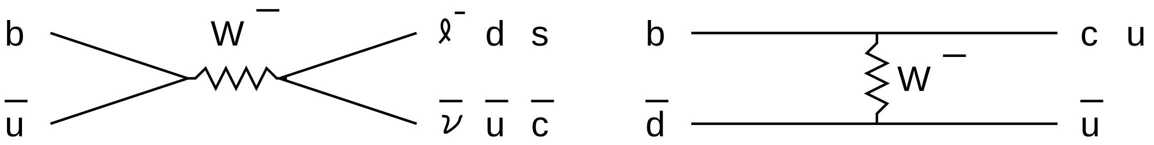

(c) Annihilation

(d) Exchange

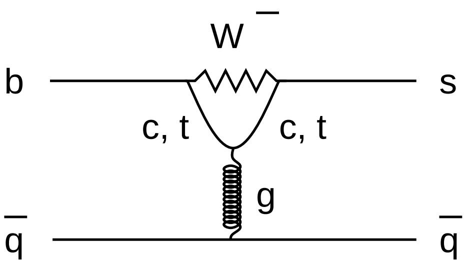

(e) Penguin

Figure 1.2: Some feynman diagrams describing B meson decay

ures 1.2(a), (b), (c) and (d). More complicated amplitudes are of course possible. For example, Figure 1.2(e) shows an example of a penguin decay.

The most important diagram for this thesis is the spectator process of Figure 1.2(a), which is expected to be the dominant process in B decay. The W^- can decay either to a lepton-antineutrino pair, called *semileptonic* B decay, or the W^- can decay to a quark-antiquark pair, called *hadronic* B decay. In hadronic decay, the W^- may materialize into a number of hadrons if fragmentation causes extra quark-antiquark pairs to be popped from the vacuum. The semileptonic decay is particularly interesting for two reasons. Firstly, the leptons from the W^- do not interact with the hadrons from the lower vertex, which makes this decay mode easier to understand. Secondly, the charge of the lepton from the W^- indicates the flavor of the b quark within the B meson.

In this thesis, semileptonic decays will be used to measure two properties of the $\overline{B^0}$ meson. For both measurements, a sample of events enriched in $\overline{B^0}$ will be obtained using a technique called $\overline{B^0}$ *tagging*. We present a measurements of the $\overline{B^0} - B^0$ mixing parameter χ_d and the neutral B semileptonic branching fraction $\mathrm{Br}(\overline{B^0} \to X\ell^-\overline{\nu})$. Using common tools and techniques, these measurements investigate two complementary aspects of $\overline{B^0}$ decay. The mixing measurement is a probe of the fundamental parameters ρ and η of the CKM matrix describing weak decays of quarks, while the semileptonic branching fraction measurement is a probe of our understanding of the hadronic width of B decays, in effect an examination of QCD calculations and thus an investigation of the strong force.

The remainder of this thesis is organized as follows. In Chapter 2, the physical processes of B mixing and of B semileptonic decay will be discussed. Chapter 3 presents the measurement of $\overline{B^0} - B^0$ mixing using neutral B tags, and describes the tagging technique that will be used for both measurements. The measurement of the $\overline{B^0}$ semileptonic branching fraction is described in Chapter 5, including a discussion of the CLEO Collaboration's measurement of the B lifetime ratio. Finally, Chapter 6 will summarize the results presented in this thesis.

Chapter 2

Physical Processes

2.1 Mixing

The phenomenon of the spontaneous transformation of a particle into its own antiparticle is known as mixing, or particle-antiparticle oscillation. Gell-Mann and Pais predicted in 1955 that mixing should occur in the neutral kaon system[6]. The prediction was confirmed by experiment in 1957 with the observation of the effects of K^0-$\overline{K^0}$ mixing[7]. Neutral kaons are not the only particles expected to oscillate. For example, in the neutral charm meson system, D^0-$\overline{D^0}$ mixing is expected to occur as well, but at a very small rate according to the Standard Model. D^0-$\overline{D^0}$ mixing has yet to be experimentally observed[8]. Additionally, there exist two types of neutral bottom mesons, B_d ($\bar{b}d$) and the more massive B_s ($\bar{b}s$). In both systems, mixing is substantial. The ARGUS Collaboration first observed the effects of B_d^0 - $\overline{B}_d^0$ mixing in 1987[9], and evidence exists for oscillations of B_s[10]. For the remaining discussion, we will restrict our attention to the B_d system.

The Hamiltonian matrix describing the system's evolution in the basis of flavor eigenstates is

$$H\begin{pmatrix} B^0 \\ \overline{B^0} \end{pmatrix} = \begin{pmatrix} M - \frac{1}{2}i\Gamma & M_{12} - \frac{1}{2}i\Gamma_{12} \\ M_{12}^* - \frac{1}{2}i\Gamma_{12}^* & M - \frac{1}{2}i\Gamma \end{pmatrix}\begin{pmatrix} B^0 \\ \overline{B^0} \end{pmatrix}. \tag{2.1}$$

The diagonal terms describe the mass M and the decay width Γ of the flavor eigenstates, the nonzero off-diagonal terms are responsible for mixing between the eigenstates. The factor M_{12} arises from virtual transitions between B^0 and $\overline{B^0}$. Long distance effects due to common decay modes of the eigenstates contribute to Γ_{12}. Decays to these common modes such as $\pi^+\pi^-$ are CKM suppressed, and so the long distance effects are expected to be small in the bottom system[11]. Consequently, the Γ_{12} term is small and usually neglected.

If the above matrix is diagonalized, one obtains the physical states $|B_1>$ and $|B_2>$ with masses M_1, M_2 and widths Γ_1, Γ_2. In the absence of CP violation, the physical states are orthogonal and can be expressed in terms of the flavor eigenstates as

$$|B_1>= \frac{1}{\sqrt{2}}(|B^0> + |\overline{B^0}>), \tag{2.2}$$

$$|B_2>= \frac{1}{\sqrt{2}}(|B^0> - |\overline{B^0}>). \tag{2.3}$$

The frequency of B^0-$\overline{B^0}$ oscillations is driven by the size of the mass difference

$$\Delta M = M_2 - M_1 = 2\mathrm{Re}\sqrt{(M_{12}^* - i\Gamma_{12}^*/2)(M_{12} - i\Gamma_{12}/2)} \simeq 2|M_{12}|. \tag{2.4}$$

If a meson is created at time $t = 0$ in a $|B^0>$ state, then the probability that it will be $|B^0>$ at a later time t is

$$P(t)^{\text{unmixed}}| < B^0(t)|B^0 > |^2 = \frac{1}{2}\exp[-\Gamma t(1 + \cos(\Delta M t))] \tag{2.5}$$

and the probability that it will instead be in a state $|\overline{B^0}>$ is

$$P(t)^{\text{mixed}} = | < \overline{B^0}(t)|B^0 > |^2 = \frac{1}{2}\exp[-\Gamma t(1 - \cos(\Delta M t))]. \tag{2.6}$$

Integrating the above time-dependent probabilities over the entire lifetime of the meson, one obtains the fraction of the time that the meson will decay in the state $|B^0>$ or $|\overline{B^0}>$ as

$$N(B^0) = \int_0^\infty P(t)^{\text{unmixed}} = \frac{1}{2}\left[\frac{1}{\Gamma} + \frac{\Gamma}{\Gamma^2 + (\Delta M)^2}\right] \tag{2.7}$$

$$N(\overline{B^0}) = \int_0^\infty P(t)^{\text{mixed}} = \frac{1}{2}\left[\frac{1}{\Gamma} - \frac{\Gamma}{\Gamma^2 + (\Delta M)^2}\right]. \tag{2.8}$$

Thus, the probability that a state created as $|B^0>$ will decay as $|\overline{B^0}>$ is given by

$$\chi_d = \frac{N(\overline{B^0})}{N(B^0) + N(\overline{B^0})} = \frac{x_d^2}{2(1 + x_d^2)} \tag{2.9}$$

where

$$x_d \equiv \Delta M/\Gamma. \tag{2.10}$$

(Here, the subscript d is explicitly written to avoid confusion with the similarly defined quantities in the literature for the B_s meson.)

Mixing occurs through a second order weak transition, and is described by the two box diagrams shown in Figure 2.1. The off-diagonal mass term in the Hamiltonian M_{12} is calculated from these diagrams[11]. Neglecting QCD corrections, the expression for the mass difference takes the general form

$$\Delta M = \frac{G_F^2 M_W^2}{8\pi^2} < \overline{B^0}|j_\mu^{V-A} j^{V-A,\mu}|B^0 > \sum_{u,c,t} \lambda_i \lambda_j A_{ij} \tag{2.11}$$

where λ_i is given by the CKM matrix elements

$$\lambda_i = V_{ib}^* V_{id} \tag{2.12}$$

for $i = u, c, t,\ j = u, c, t$ and the terms A_{ij} are the results of loop integrals which are functions of the mass of the virtual quarks and of the W. Although each of the virtual quarks inside the loop can be either u, c, or t, the dominant contribution is

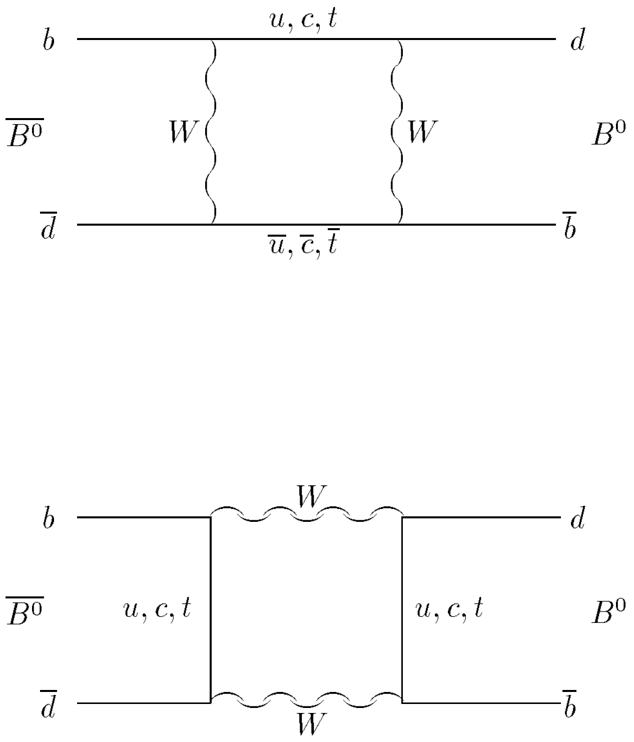

Figure 2.1: Box diagrams for B_d mixing

when both quarks are top[11]. The vacuum insertion approximation is used to solve the matrix element

$$\begin{aligned} < \overline{B^0} | j_\mu^{V-A} j^{V-A,\mu} | B^0 > &= < \overline{B^0} | [\bar{b}\gamma_\mu(1-\gamma_5)d][\bar{b}\gamma_\mu(1-\gamma_5)d] | B^0 > \\ &= B < \overline{B^0} | [\bar{b}\gamma_\mu(1-\gamma_5)d] | 0 >< 0 | [\bar{b}\gamma_\mu(1-\gamma_5)d] | B^0 > \\ &= B \tfrac{4}{3} f_B^2 m_B. \end{aligned} \tag{2.13}$$

Here B is the bag parameter arising from this approximation, f_B is the B^0 decay constant, and m_B is the mass of the meson. B describes the degree to which the box diagrams of Figure 2.1 dominate the mixing, and estimates are that the value lies close to 1.0[12].

Perturbative QCD corrections to the box diagrams are able to be summarized in an overall multiplicative factor η_{QCD} [13, 14]. Calculations indicate[15]

$$\eta_{\mathrm{QCD}} \simeq 0.55. \tag{2.14}$$

The final expression for ΔM then takes the form

$$\Delta M = \frac{G_F^2}{6\pi^2} B f_B^2 m_B m_W^2 \eta_{\mathrm{QCD}} F(m_t) |(V_{tb}^* V_{td})^2| \tag{2.15}$$

where

$$F(m_t) \simeq \frac{m_t^2}{m_W^2} f(\frac{m_t^2}{m_W^2}) \tag{2.16}$$

and

$$f(x) = \frac{1}{4} + \frac{9}{4(1-x)} - \frac{3}{2}\frac{1}{(1-x)^2} - \frac{3}{2}\frac{x^2 \ln x}{(1-x)}. \tag{2.17}$$

In this expression G_F is the Fermi coupling constant, m_t and m_W are the top quark and W boson masses. The function $F(m_t^2/m_W^2)$ changes slowly for a range of top masses, with $F(0) = 1$ and $F(1) = 0.75$.

There is a substantial uncertainty on the value of the decay constant f_B which limits the precision with which one can measure V_{td}. The decay constant can be

Group	$\sqrt{B} f_B$/MeV	Reference
BLS	$187 \pm 10 \pm 37$	[16]
UKQCD	$160 \,^{+6}_{-6}\,^{+53}_{-19}$	[17]
PWCD	180 ± 50	[18]
ELC	205 ± 40	[19]
Hashimoto	$171 \pm 22 \,^{+19}_{-45}$	[20]
FNAL	$188 \pm 23 \,^{+34}_{-21}$	[21]
APE	$290 \pm 15 \pm 45$	[22]

Table 2.1: Calculations of the B decay constant

measured through the channel $B^- \to \ell^- \, \bar{\nu}_\ell$ but current experimental limits are considerably larger than theoretical expectation. CLEO[23] has set an upper limit of 2.2×10^{-3} for $B(B^- \to \tau^- \, \bar{\nu}_\tau)$ corresponding to an upper limit of 6.8 MeV on the product $f_B |V_{ub}|$. Taking $|V_{ub}/V_{cb}| = 0.08$ and $|V_{cb}| = 0.04$, this implies an upper limit on f_B of approximately 2 GeV. Clearly, it will be some time before f_B will ever be measured by experiment. Consequently, the only information about f_B comes from theoretical calculations, summarized in Table 2.1. Most make the assumption that $B = 1$. For this thesis, we take $\sqrt{B} f_B = 180 \pm 50$ MeV, following the example of Reference [24]. The assigned uncertainty of 50 MeV is to be taken with caution, and may be an underestimate.

There is some hope that feedback from experiment can aid in the narrowing of these predictions. CLEO[25] has measured the D_s decay constant via the channel $D_s \to \mu^+ \, \nu_\mu$, finding $f_{D_s} = 344 \pm 37 \pm 67$. This measurement can be compared with lattice calculations of f_{D_s}. What is learned can strengthen confidence in the f_B calculations. Additionally, the ratio f_B / f_{D_s} may be determined with better precision than f_B alone.

A measurement of ΔM in turn yields information about standard model parame-

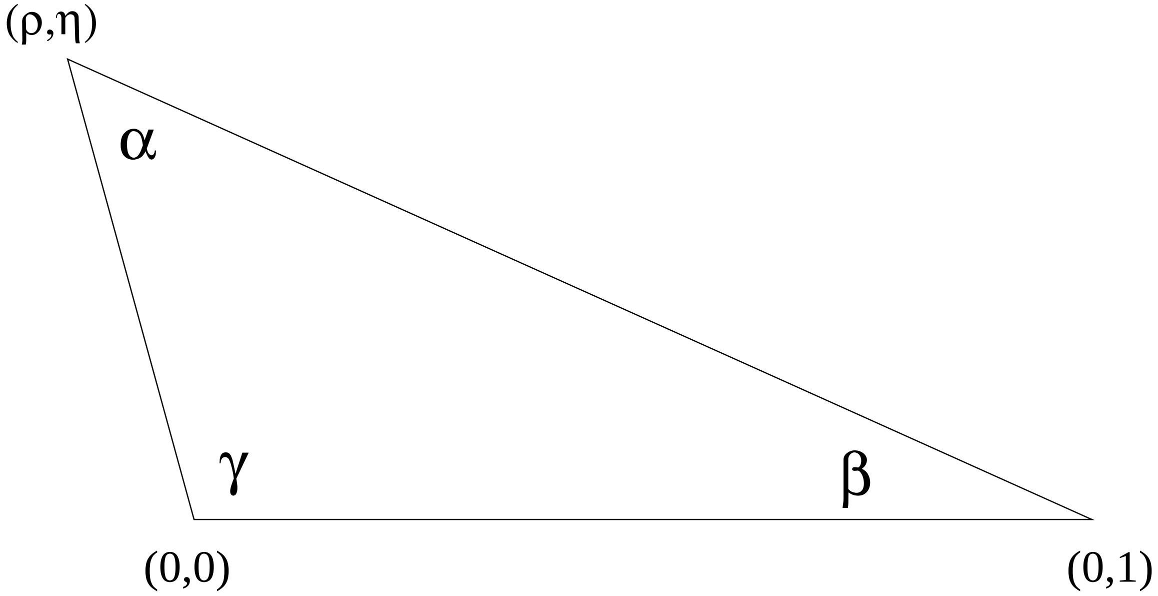

Figure 2.2: One of six unitarity triangles

ters. Unitarity of the CKM matrix implies that any two rows or any two columns are orthogonal, six conditions in all. We examine the condition which combines elements from the first and third columns

$$V_{ud}V_{ub}^* + V_{cd}V_{cb}^* + V_{td}V_{tb}^* = 0. \tag{2.18}$$

This can be rewritten in the Wolfenstein parameterization as

$$\frac{V_{ub}^*}{\lambda V_{cb}} + \frac{V_{td}^*}{\lambda V_{cb}} = 1 \tag{2.19}$$

which describes a triangle in the complex plane with vertices at $(0,0)$, $(0,1)$ and (ρ,η), shown in Figure 2.2. Since

$$|V_{td}| \simeq A\lambda^3\sqrt{(1-\rho)^2+\eta^2}, \tag{2.20}$$

a measurement of ΔM therefore gives information about the quantities ρ and η, constraining an annular region in the $\rho-\eta$ plane centered about $(0,1)$. Other constraints can be determined from measurement of the Cabibbo-suppressed rate $b \rightarrow u\ell\nu$, and from measurement of the parameter $|\epsilon|$ in CP-violating neutral kaon decays. Thus, $\overline{B^0} - B^0$ mixing plays an important role in the determination of the fundamental parameters ρ and η of the CKM matrix.

2.2 Semileptonic Branching Fraction

One of the outstanding problems in heavy quark physics is the apparent discrepancy between the measured and the predicted values for the B meson semileptonic branching fraction. This is a question of the relative sizes of the semileptonic and hadronic B decay widths. Although both widths must be calculated to arrive at the B semileptonic branching fraction, the hadronic portion is the more difficult to determine. Thus, comparison of theory and experiment is effectively a probe of the hadronic portion of the the total B decay width, and a useful tool to aid in our understanding of QCD.

Predictions for Total Rate

Semileptonic B decay proceeds through a coupling of the b quark to a c- or u-quark and, via W^-, to a $l^-\overline{\nu}$ pair. The accompanying quark plays no direct role and is known as the spectator. The semileptonic branching fraction is defined here to be

$$\mathrm{Br}(\overline{B} \to X\ell^-\bar{\nu}_\ell) = \frac{\Gamma(\overline{B} \to X\ell^-\bar{\nu}_\ell)}{\Gamma(\overline{B} \to \mathrm{All})} \tag{2.21}$$

where

$$\mathrm{Br}(\overline{B} \to X\ell^-\bar{\nu}_\ell) = \mathrm{Br}(\overline{B} \to Xe^-\bar{\nu}_e) = \mathrm{Br}(\overline{B} \to X\mu^-\bar{\nu}_\mu). \tag{2.22}$$

The τ lepton is not included in this equality because its large mass reduces the available phase space, resulting in a smaller decay rate.

The rate for such semileptonic decays can be naïvely calculated in the spectator model by simply accounting for all possible decay products of the W and ask which fraction are electrons (or muons). First, accounting for all possible decay products, one finds that the overall B decay width is

$$\Gamma_B = \frac{G_F^2 |V_{cb}|^2 m_b^5}{192\pi^3} \eta_{\mathrm{QCD}} (5r_c + 3r_{cc} + r_{\tau c}) \tag{2.23}$$

and the semileptonic width is

$$\Gamma_e = \frac{G_F^2 |V_{cb}|^2 m_b^5}{192\pi^3} \eta_{\mathrm{QCD}} r_c \tag{2.24}$$

In these expressions, the small contribution from $b \to u$ transitions has been neglected. The correction factor[1] η_{QCD} is approximately 0.94[26, 27]. The quantities r account for different phase space factors depending on the mass of the final decay products of the W. We take $r_c = 0.45$, and $r_{cc} = r_{\tau c} = 0.12$[28]. In this view, the semileptonic branching fraction is given as

$$\mathrm{Br}(\overline{B} \to X \ell^- \bar{\nu}_\ell) = \frac{\Gamma_e}{\Gamma_B} = \frac{r_c}{5r_c + 3r_{cc} + r_{\tau c}} = 16.5\%. \tag{2.25}$$

This picture is not entirely accurate, however. Effects of hard gluon exchange and gluon radiation increase the hadronic width[29, 30]. The nonleptonic width is enhanced by the factors η and J where

$$\eta = \frac{c_-^2 + 2c_+^2}{3} \tag{2.26}$$

and c_+ and c_- are the Wilson coefficients given by

$$c_\pm = \left[\frac{\alpha_s(\mu)}{\alpha_s(M_W)}\right]^{d_\pm} \tag{2.27}$$

with $d_+ = -\frac{6}{23}$ and $d_- = \frac{12}{23}$. Gluons with momenta in the range μ to M_W are considered in this calculation. The additional factor J accounts for soft gluons below

---

[1] Here, η_{QCD} is different from the quantity presented previously in the mixing discussion.

the momentum cutoff μ. The product of the factors is approximately $\eta J = 1.27$, but this number is sensitive to a number of quantities including the quark masses, and a color matching factor ξ not shown explicitly in the expression for η. In the asymptotic limit, ξ equals 1/3, but in other theories of QCD ξ equals 0[31, 32]. After perturbative QCD corrections, the semileptonic branching fraction becomes

$$\mathrm{Br}(\overline{B} \to X\ell^- \bar{\nu}_\ell) = \frac{\Gamma_e}{\Gamma_B} = \frac{r_c}{2r_c + \eta J(r_c + r_{cc}) + r_{\tau c}}. \tag{2.28}$$

For reasonable ranges of quark masses, the perturbative corrections lower the semileptonic branching fraction into the range $12.2 - 14.4\%$[33].

Calculations of the nonperturbative QCD corrections have been recently improved through the advent of the Heavy Quark Expansion[34, 35]. Up to order $1/m_b^2$, the corrections have been found to decrease the semileptonic branching fraction, but only by a mere 2% of it's value. Additionally, corrections to order $1/m_b^3$ have been studied are expected to be quite small[36]. The effects of nonperturbative corrections to the semileptonic branching fraction are therefore usually ignored. After most effects are taken into account, the prevailing view has recently been that the prediction for the B semileptonic branching fraction is not lower than approximately 12.5%[36].

One Exclusive and One Inclusive Model

One can examine not only the overall semileptonic decay rate Γ_{sl} but also the lepton energy spectrum $\mathrm{d}\Gamma_{\mathrm{sl}}/\mathrm{d}E$. There exist a number of models which describe semileptonic B decay, each with a unique lepton energy spectrum. It is *not* the purpose of this thesis to examine the measured quantity $\mathrm{d}\Gamma_{\mathrm{sl}}/\mathrm{d}E$ in order to distinguish among these models. Rather, a model for $\mathrm{d}\Gamma_{\mathrm{sl}}/\mathrm{d}E$ will be chosen in order to arrive at a value of Γ_{sl}. It is for that reason that the subject will now be briefly discussed.

These models of semileptonic B decay can be broken down into two general categories - inclusive and exclusive. Inclusive models treat the quarks as free objects, while exclusive models consider the decay to each final state meson (D, D^*, D^{**}) separately. Here only one model of each type will be summarized, the inclusive model of Altarelli *et al.* and the exclusive model of Isgur *et al.*

In the model of Altarelli, Cabibbo, Corbò, Maiani and Martinelli (ACCMM) [37], the spectator quark is taken to have a random Fermi momentum p given by

$$f(p) = \frac{4p^2}{\sqrt{\pi}p_f^3}\exp(-p^2/p_f^2). \tag{2.29}$$

In this model, p_f is a free parameter. To conserve energy and momentum, the b quark is assigned an off-shell mass squared

$$m_b^2 = m_B^2 + m_{\rm sp}^2 - 2m_B\sqrt{p^2 + m_{\rm sp}^2} \tag{2.30}$$

where $m_{\rm sp}$ is the mass of the spectator quark and m_B is the mass of the B meson. This is convoluted with the semileptonic partial width

$$\frac{{\rm d}\Gamma_{\rm sl}}{{\rm d}x} = \frac{G_F^2 V_{cb}^2 m_b^5}{96\pi^3}[\Phi(x,\epsilon) - G(x,\epsilon)] \tag{2.31}$$

to arrive at the lepton energy spectrum. Here $x = 2E_\ell/m_b$ and $\epsilon = m_c/m_b$. The function $\Phi(x,\epsilon)$ accounts for the phase space and the $V-A$ structure of the $b \to cW^-$ current and has the form[38]

$$\Phi(x,\epsilon) = \frac{x^2(1-\epsilon^2-x)^2}{(1-x)^3}[(1-x)(3-2x)+(3-x)\epsilon^2]. \tag{2.32}$$

The function $G(x,\epsilon)$ accounts for the effects of gluon radiation and is not shown explicitly here. It is effectively independent of the lepton energy and is important only at the spectrum endpoint. One attraction of this model is that it avoids the explicit m_b^5 dependence which carries a substantial uncertainty due to lack of knowledge of the b quark mass. Instead, this dependence is absorbed in the less-sensitive parameter p_f which is determined from fitting the shape of the spectrum.

The exclusive models assume that the semileptonic decays proceed dominantly to single body resonant final states such as D and D^*. The hadronic currents can be expressed as

$$< D|A_\mu|\overline{B} >= 0 \tag{2.33}$$

$$< D|V_\mu|\overline{B} >= f_+(p_B + p_D)_\mu + f_-(p_B - p_D)_\mu \tag{2.34}$$

$$< D^*|A_\mu|\overline{B} >= f\epsilon^*_\mu + a_+(\epsilon^*\dot{p}_B)(p_B + p_{D^*})_\mu + a_-(\epsilon^*\dot{p}_B)(p_B - p_{D^*})_\mu \tag{2.35}$$

$$< D^*|V_\mu|\overline{B} >= ig\epsilon_{\mu\mu\rho\sigma}\epsilon^{*\nu}(p_B + p_D)^\rho(p_B + p_{D^*})^\sigma \tag{2.36}$$

where the quantities a, f and g are the form factors which each model must determine. The form factors f_- and a_- are unimportant because they multiply terms which are proportional to lepton mass and therefore negligible.

The exclusive model of Isgur, Scora, Grinstein and Wise (ISGW)[39] calculates these form factors by determining them first for the largest lepton momentum transfers, known as q^2_{max} where the final state meson is at rest with respect to the parent meson frame. Next, the form factors are extrapolated to the kinematic regime where the charm meson becomes relativistic. The form factors are calculated from Schrödinger's equation with a Coulomb plus linear potential of the form

$$V(r) = -\frac{4\alpha_s}{3r} + br + c \tag{2.37}$$

with $\alpha_s = 0.5$, $b = 0.18$ GeV^2, $c = -0.84$ GeV. The resulting form factors have the form

$$F(q^2) \propto F(q^2_{\text{max}})\text{exp}\left(\frac{q^2_{\text{max}} - q^2}{\kappa q^2_{\text{max}}}\right) \tag{2.38}$$

where the factor κ is an ad-hoc constant which accounts for relativistic effects. From the measured pion form factor, Isgur *et al.* find $\kappa = 0.7$. The final state charm mesons considered in the ISGW model are the D, D^* and four D^{**} states. The default relative abundances of $D/D^*/D^{**}$ are 27/62/11.

The Ratio of Lifetimes

Non-spectator diagrams can contribute differently to the hadronic width of $\overline{B^0}$ and B^-, contributing to differences in lifetimes and semileptonic branching fractions. Thus, a measurement of the ratio of $\overline{B^0}$ and B^- lifetimes provides important feedback in order to understand the puzzle of the semileptonic branching fraction.

As an example of such effects, the lifetimes of the D^+ is 2.5 times that of the D^0. In the D system, the lifetime difference is mainly caused by a reduction of the D^+ hadronic rate from interference between the two amplitudes where the $\bar{d}$ quark from the W^+ decay and the spectator $\bar{d}$ quark are interchanged.

Current predictions are that the $\overline{B^0}$ and B^- mesons have similar lifetimes. Isospin symmetry indicates that $\overline{B^0}$ and B^- mesons should have equal widths for both inclusive and exclusive channels. This assertion is supported by predictions from the QCD corrected spectator model of B decays, as well as the observed equality of semileptonic widths of the D^+ and D^0 mesons Predictions of the asymmetry in total width of B mesons are at the level of 5%[40]

$$\frac{\tau_-}{\tau_0} \simeq 1 + 0.05\left[\frac{f_B^2}{(200\ \mathrm{MeV})^2}\right]. \tag{2.39}$$

Experimentally, this asymmetry is normally expressed as the ratio of semileptonic branching fractions, as a number of systematic errors cancel in taking the ratio. Assuming equality of semileptonic widths, this ratio is equal to the ratio of lifetimes or inverse that of the total widths:

$$\begin{aligned} \frac{\tau(B^-)}{\tau(\overline{B^0})} &= \frac{\Gamma_{\mathrm{tot}}(\overline{B^0})}{\Gamma_{\mathrm{tot}}(B^-)} \\ &= \frac{\Gamma_{\mathrm{tot}}(\overline{B^0})}{\Gamma(\overline{B^0}\to X\ell^-\bar{\nu})} * \frac{\Gamma(B^-\to X\ell^-\bar{\nu})}{\Gamma_{\mathrm{tot}}(B^-)} \\ &= \frac{\mathrm{Br}(B^-\to X\ell^-\bar{\nu})}{\mathrm{Br}(\overline{B^0}\to X\ell^-\bar{\nu})} \\ &= \frac{b_-}{b_0} \end{aligned} \tag{2.40}$$

The ratio b_-/b_0 may thus be compared directly to the ratio of lifetimes, measured through decays in flight.

Chapter 3

The Apparatus

This thesis presents some measurements of $\overline{B^0}$ meson properties. In order to make these measurements, a means of producing the $\overline{B^0}$ mesons is required, as well as a means of observing their decay. A machine called the Cornell Electron Storage Ring (CESR) produces the $\overline{B^0}$ mesons for this thesis, and a device called the CLEO II detector observes the decays.

3.1 CESR

The Cornell Electron Storage Ring is located inside a 244 meter diameter tunnel some 10 meters beneath the athletic fields of the Cornell University campus in Ithaca, New York. Its purpose is to collide electrons with positrons with center of mass energy in the range of 9 to 12 GeV, the region of the Υ resonances.

Before collisions can occur, a multi step acceleration process must take place. This begins with the thermionic emission of electrons from a hot filament cathode at the end of a linear accelerator, or linac (see Figure 3.1). After traversing the 30 meter length of the linac, the electrons reach an energy of about 150 MeV before being injected into the synchrotron. The synchrotron takes the electrons and accelerates them with radiofrequency cavities to 5 GeV within a fraction of a second. Having reached their full energy, the electrons are then passed to CESR through the east transfer line into one of 7 different bunches, evenly spaced about CESR. This entire acceleration cycle is repeated at 60 Hz until the current of electrons in CESR reaches the desired level.

Since positrons are not naturally occurring particles, the procedure for filling CESR with them is somewhat more complicated than for electrons. As before, electrons are accelerated in the linac, but they then strike a thin tungsten target which is placed halfway down the length of the linac. A shower of electrons, x-rays and positrons are produced by the target. The positrons are then collected, accelerated down the remainder of the linac, and injected into synchrotron and CESR, but in the direction opposite the electrons.

Once inside CESR, the electrons and positrons gradually lose energy through emission of synchrotron radiation in the form of x-rays. The loss is of order 1 eV per particle per turn in CESR. This energy must be continuously restored to the beams in order to maintain the requisite center of mass energy at the beam collision point. A set of radiofrequency cavities provides the necessary energy to the beams to offset synchrotron radiation losses. A separate facility called the Cornell High Energy Synchrotron Source (CHESS), also shown in Figure 3.2, uses these x-rays to study the structure of materials.

In practice, the positrons are injected first into CESR, followed by the electrons. The entire injection procedure takes approximately 10 minutes. The accelerator has recently been running on a duty cycle where the stored beams remain in CESR for

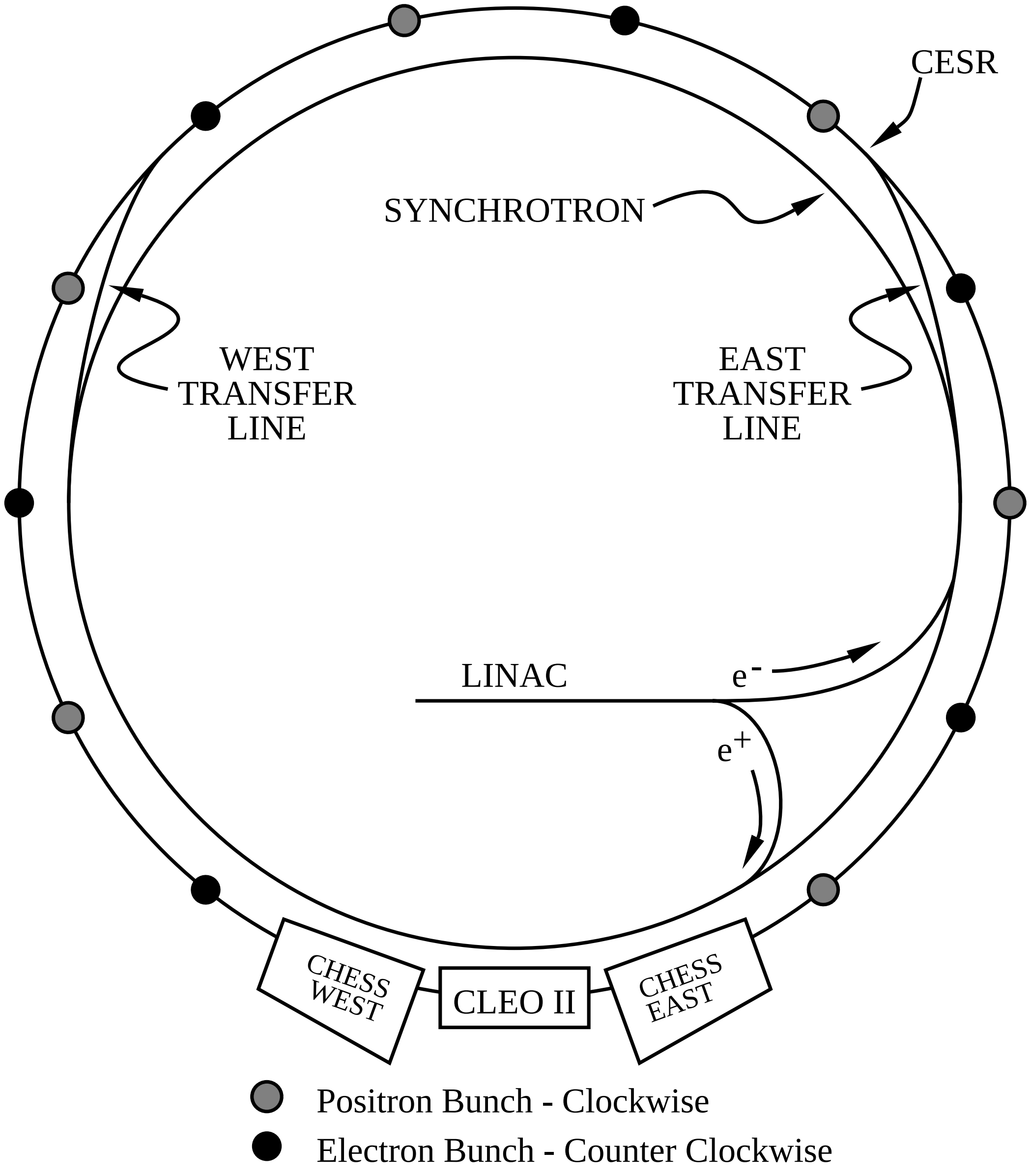

Figure 3.1: Schematic of the Cornell Electron Storage Ring

approximately 1 hour before the machine is filled again. The beams have a finite lifetime due to losses from occasional collisions of the beam particles with residual gas molecules in the vacuum chamber, with the vacuum chamber walls, and with other beam particles.

Once the counter-rotating bunches of electrons and positrons are in CESR, they are kept apart by a series of electrostatic separators such that there are no collisions, except at one point in the ring. There, the two bunches are focussed and cross in an area of size 500 μm wide by 10 μm high at a rate of 2.7 MHz. The rate at which electrons and positrons collide is the product of the instantaneous luminosity of the machine times the cross section. The luminosity of a collider is given by

$$\mathcal{L} = \frac{N_1 N_2 f n}{4A}$$

where N_1 and N_2 are the number of particles per bunch, n is the number of bunches, f is the revolution frequency of one bunch, and A is the cross sectional area of the region where the bunches cross. A typical value for $\mathcal{L}$ at CESR is $2.5 \times 10^{32}\,\mathrm{sec}^{-1}\mathrm{cm}^{-2}$. This is currently the world's highest luminosity achieved at any collider. Given a cross section of 1 nb = 1×10^{-33} cm^2 for the process $e^+e^- \rightarrow \Upsilon(4\mathrm{S}) \rightarrow B\bar{B}$, the rate of B meson pair production at CESR is ~ 0.25 Hz.

3.2 CLEO II

In this section an overview of the CLEOII detector is given, while a more detailed description can be found in reference [41].

3.2.1 History

The present CLEO II detector is the product of a gradual evolution of the original CLEO detector, which started taking data in 1979 when CESR first came online.

The original detector consisted of a 17 layer drift chamber inside a conventional solenoidal magnet of radius 1 meter with a 0.4 Tesla field. A system of octants was outside the coil and included tracking instrumentation, proportional chambers, time of flight counters, electromagnetic calorimeters, magnetic flux return, and muon chambers. The first CLEO detector was not optimized for the study of B mesons because it was designed before the first Υ resonance was discovered in 1977. The first upgrade was in 1981 to replace the magnet with a superconducting coil, providing a 1.0 Tesla field. In 1984, a new 10 layer tracking chamber, the vertex chamber (VD) was added at the innermost region of the detector. A completely new 51 layer main drift chamber (DR) was installed in 1986, and the resulting detector was dubbed CLEO 1.5.

The CLEO II detector was installed in 1988-89. Two views of the detector are shown in Figures 3.2 and 3.3. The detector recycles the same VD and DR tracking chambers from CLEO 1.5, but all other elements are new. These include a smaller radius beam pipe, a straw tube tracking chamber inside the VD, a time of flight system, a CsI crystal electromagnetic calorimeter, a new superconducting solenoid at 1.5 meter radius with a 1.5 Tesla magnetic field, and a muon identification system.

The CLEO II detector is not the end product of this evolutionary process. As this thesis is being written, preparations are being made to replace the beam pipe and innermost tracking chamber with a smaller radius pipe and a three-layer silicon vertex detector. The upgraded CLEO II detector should begin taking data in the Fall of 1995. Additionally, construction is beginning on the CLEO III detector, planned to be ready a few years hence. CLEO III will be based on the CLEO II detector, but with all elements inside the radius of the crystal calorimeter replaced. The new systems will include a completely new set of silicon detectors, a new drift chamber and a ring imaging cerenkov detector for particle identification at high momentum. Thus, the CLEO II detector represents one phase of a very active and ever-improving program to study heavy flavor physics at the $\Upsilon(4S)$.

3.2.2 Beam Pipe

The CLEO II beam pipe is beryllium tube of radius 3.5 cm, length 33 cm and thickness 0.5 mm. The pipe is designed to have walls as thin as possible while still providing mechanical stability against the stresses introduced by one atmosphere of pressure. A thin wall reduces the likelihood of either scattering or energy loss by particles passing through it. The 0.5 mm thickness of beryllium represents 0.44% of a radiation length.[1] Finally, the inner surface of the beam pipe is coated with a 1 μm layer of Ni and a 20 μm layer of Ag to absorb unwanted background from synchrotron radiation.

3.2.3 Precision Tracking Layers

The PTL (Precision Tracking Layers) is the tracking device which is closest to the beam pipe. It extends from a radius of 4.5 cm to 8 cm and has a length of .5 meters. It is composed of 6 layers, each with 64 tubes containing a sense wire, as shown in Figure 3.4. The walls of the tubes are conductive aluminized mylar and serve as the cathode, and the anode wires are 15 μm gold plated tungsten. No measurements are made by the PTL of the z-coordinate of tracks. When CLEO II began taking data in

---

[1] A fast electron passing through one radiation length of material loses 63 % of its energy.

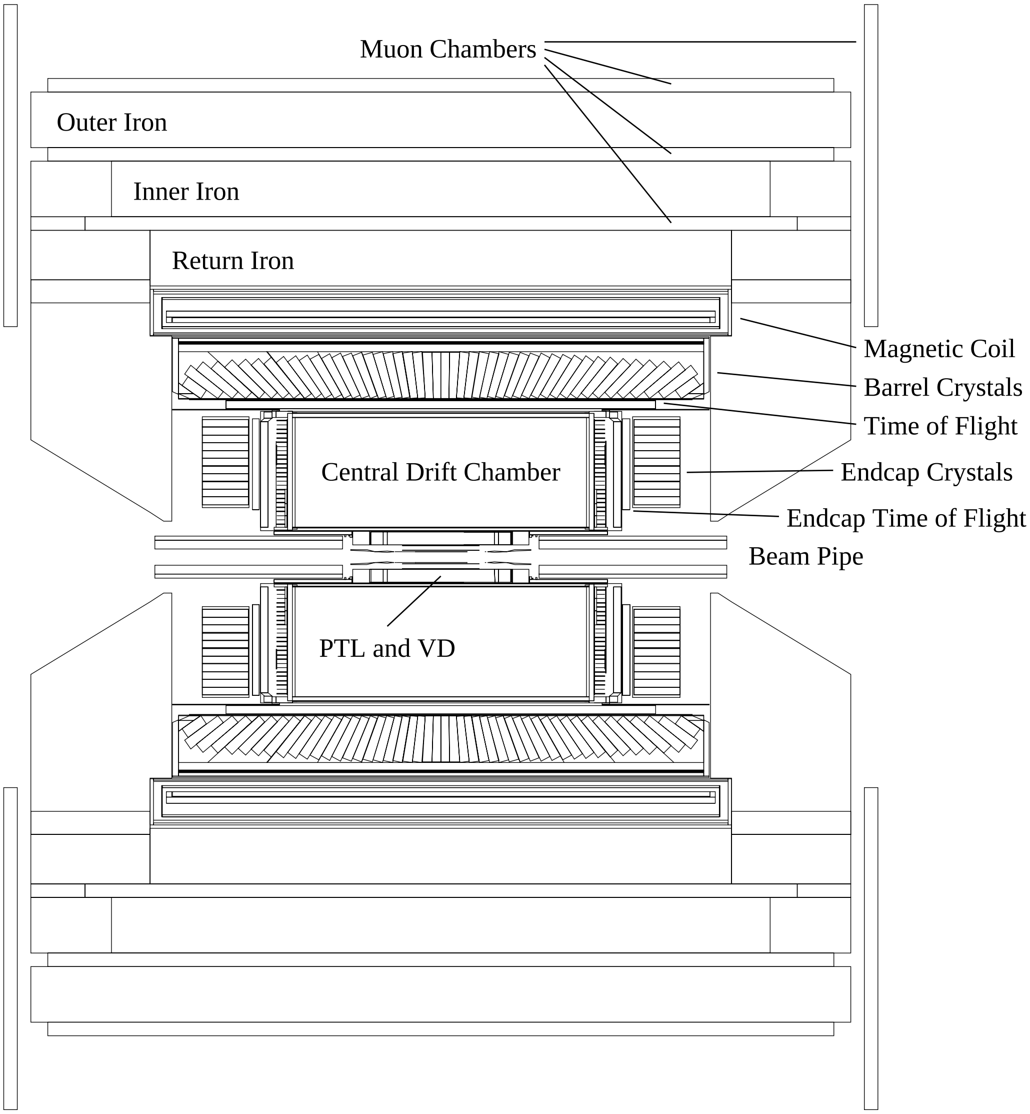

Figure 3.2: Cross section of the CLEO II detector, side view

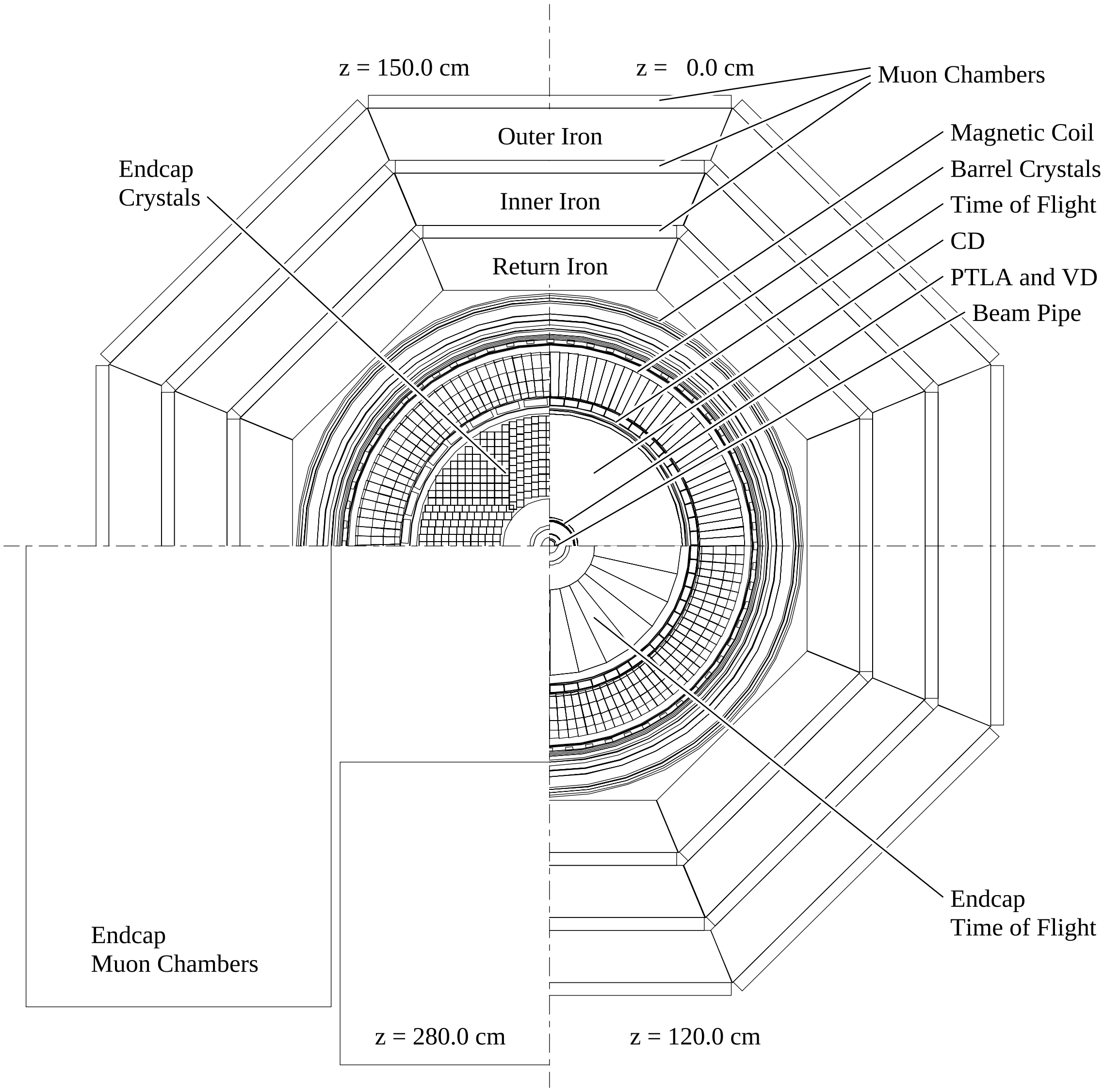

Figure 3.3: Cross section of the CLEO II detector, end view. Each value of z represents a different distance from the center of the detector.

1989, the gas used in the PTL was a 50:50 mixture of argon and ethane. Using this gas, the spatial resolution on the position measurements was 100 μm. The PTL gas was changed in the spring of 1992 to dimethylethane (DME) improving the resolution to 50 μm.

3.2.4 Vertex Detector

The VD extends from a radius 8.1 cm to 16.4 cm and has a length of 0.9 meters. It is a wire chamber with 10 layers of sense wires housed between two carbon filament tubes. There are 64 sense wires per layer in the first five layers, and 96 sense wires per layer in the remainder, each at the center of a hexagonal cell. On the inside of the first and the outside of the tenth layers, cathode strips complete the remaining field shaping. The cross section is shown in Figure 3.4. The chamber is filled with a 50:50 mixture of argon and ethane, 5 psi over atmospheric pressure. The added pressure provides higher gain and shorter drift times. Unlike the PTL, the VD provides information about the z-coordinate of the track by comparing the relative amplitude of signals observed at opposite ends of each sense wire. The wires are composed of a nickel-chromium alloy, with a slightly larger resistance than the tungsten, appropriate for use in this charge division technique. Using this method the z-coordinate where the track passed nearest each sense wire is measured with a resolution of 1.7 cm.

3.2.5 Main Drift Chamber

The Main drift chamber extends from 17.8 cm to 94.7 cm with a length of 1.93 meters. The chamber is strung with 51 layers of 20 μm gold plated tungsten sense wires arranged in square cells, staggered radially. The number of sense wires per layer increases with radius so as to keep the cells nearly uniform in size. In forty layers the

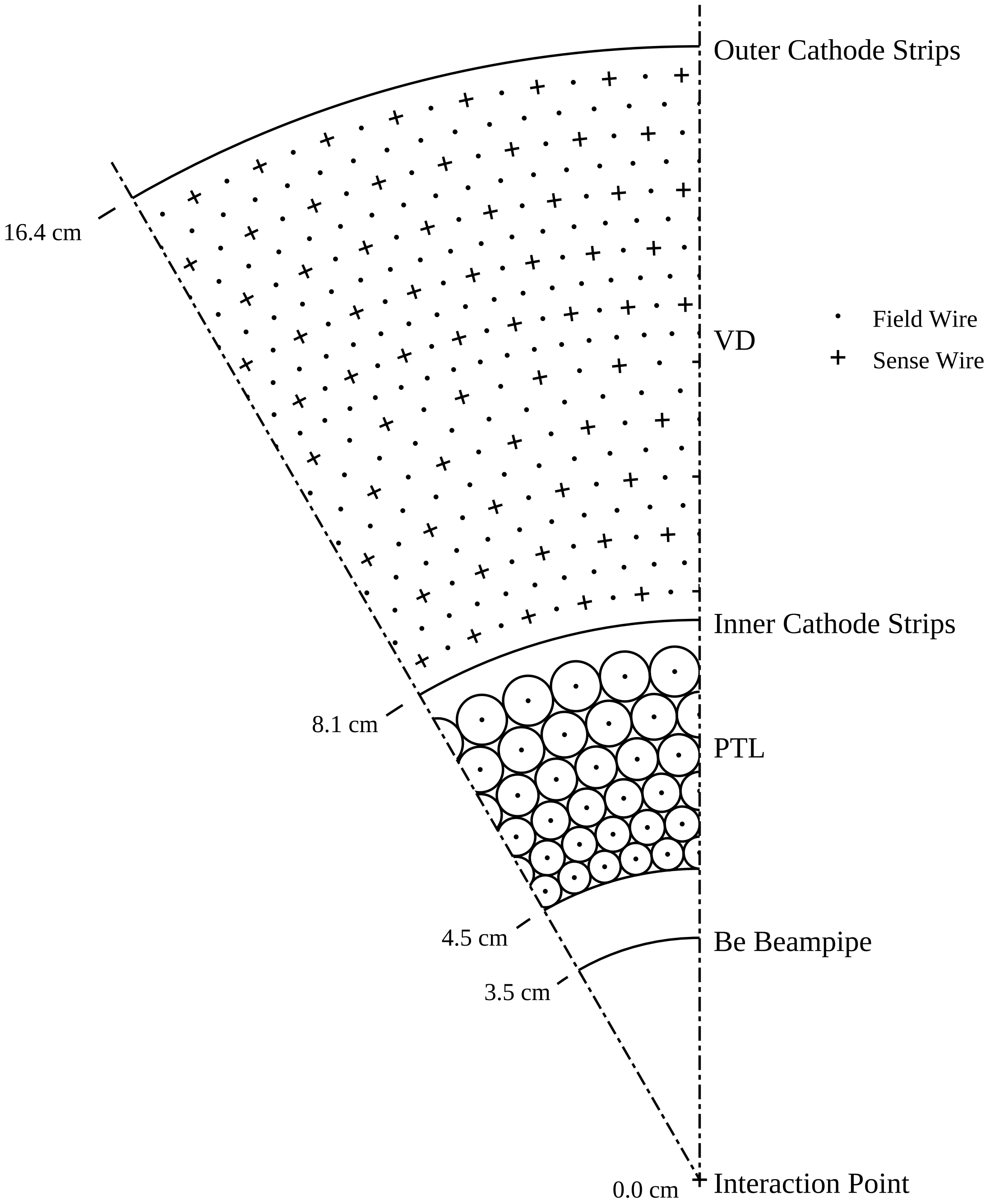

Figure 3.4: Cross section of Precision Tracking Layers and Vertex Detector

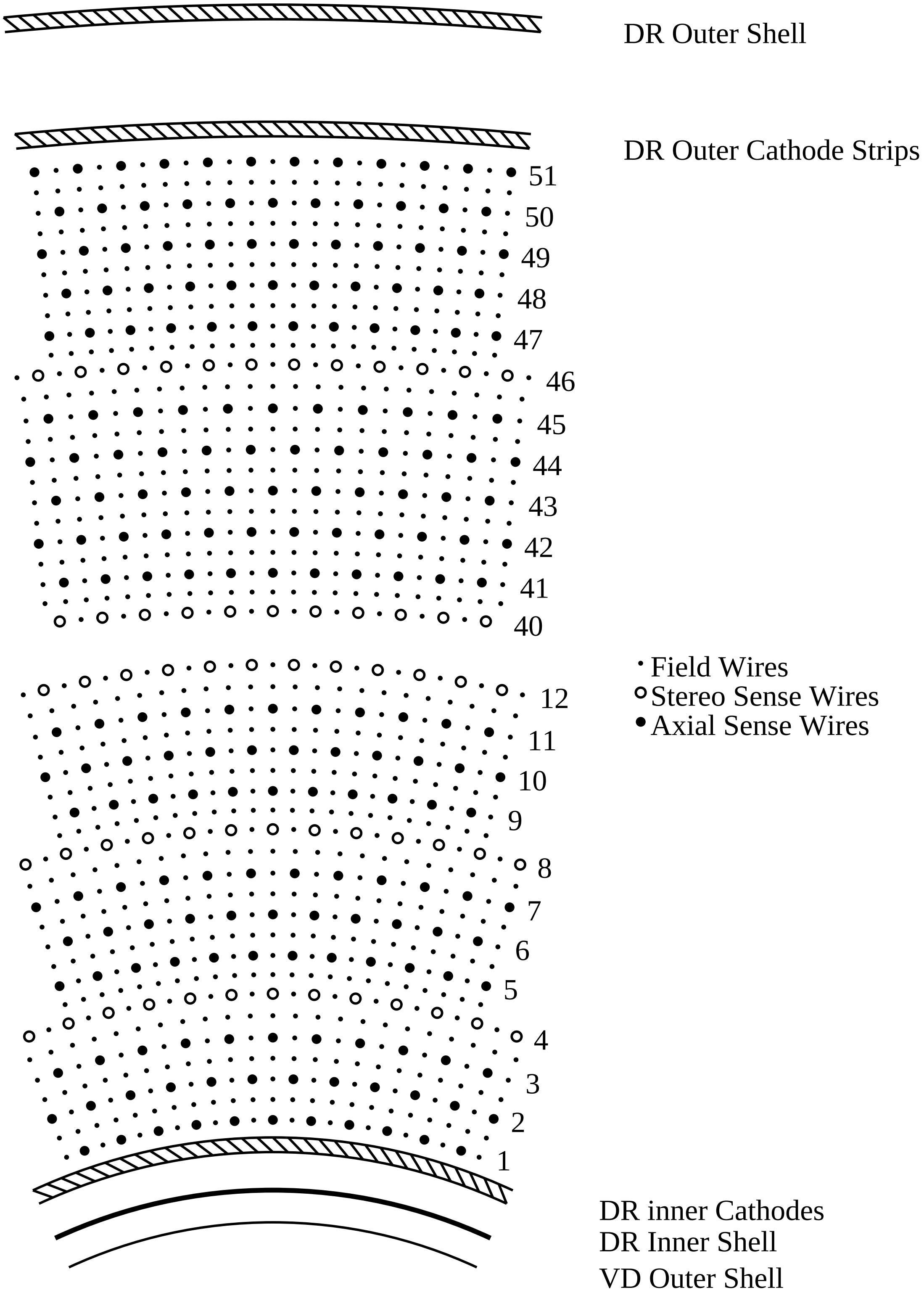

Figure 3.5: Cross section of the Main Drift Chamber

sense wires align parallel to the z axis of the detector, while the wires in the remaining eleven layers are pitched at slight angles. These pitched stereo wires, spaced about every fourth layer, provide information about the z-coordinate of the track. As in the VD, the inner and outer surfaces of the chamber contain segmented cathodes which both provide field shaping and z measurements from the induced signals. Tables 3.1 and 3.2 summarizes the wire geometry in all three chambers.

The resolution of the tracking system is measured to be

$$(\delta p_t/p_t)^2 = (0.0011 p_t)^2 + (0.0067)^2 \tag{3.1}$$

where p_t is the component of the momentum perpendicular to the beam direction in GeV/c. The angular resolution measured in $e^+e^- \rightarrow \mu^+\mu^-$ events is found to be

$$\delta\phi = 1\,\text{mrad}, \qquad \delta\theta = 4\,\text{mrad}. \tag{3.2}$$

Particle species can be determined by examining the specific ionization energy loss (dE/dx) of the track within the drift chamber. The ionization distribution has a large Landau tail. Consequently, events above the median are discarded, and the mean calculated from the remaining sample (a 50% truncated mean) is taken to be the best estimate of dE/dx. The measurement must be corrected for the dip angle within the cell, for the drift distance, and for the entrance angle in the $r-\phi$ plane of the cell. A dE/dx resolution of 6.2% is found for $e^+e^- \rightarrow e^+e^-$ (bhabha) tracks, and 7.1% for minimum ionizing pions. Figure 3.6 shows the dE/dx in units of keV/cm as a function of momentum for tracks in the drift chamber. Clear bands are visible for each particle species. We define `SGxxDI` as the difference between the measured dE/dx and the dE/dx one would expect for particle species `xx`, divided by the resolution, with `xx` being either `EL`, `MU`, `PI`, `KA` or `PR`.

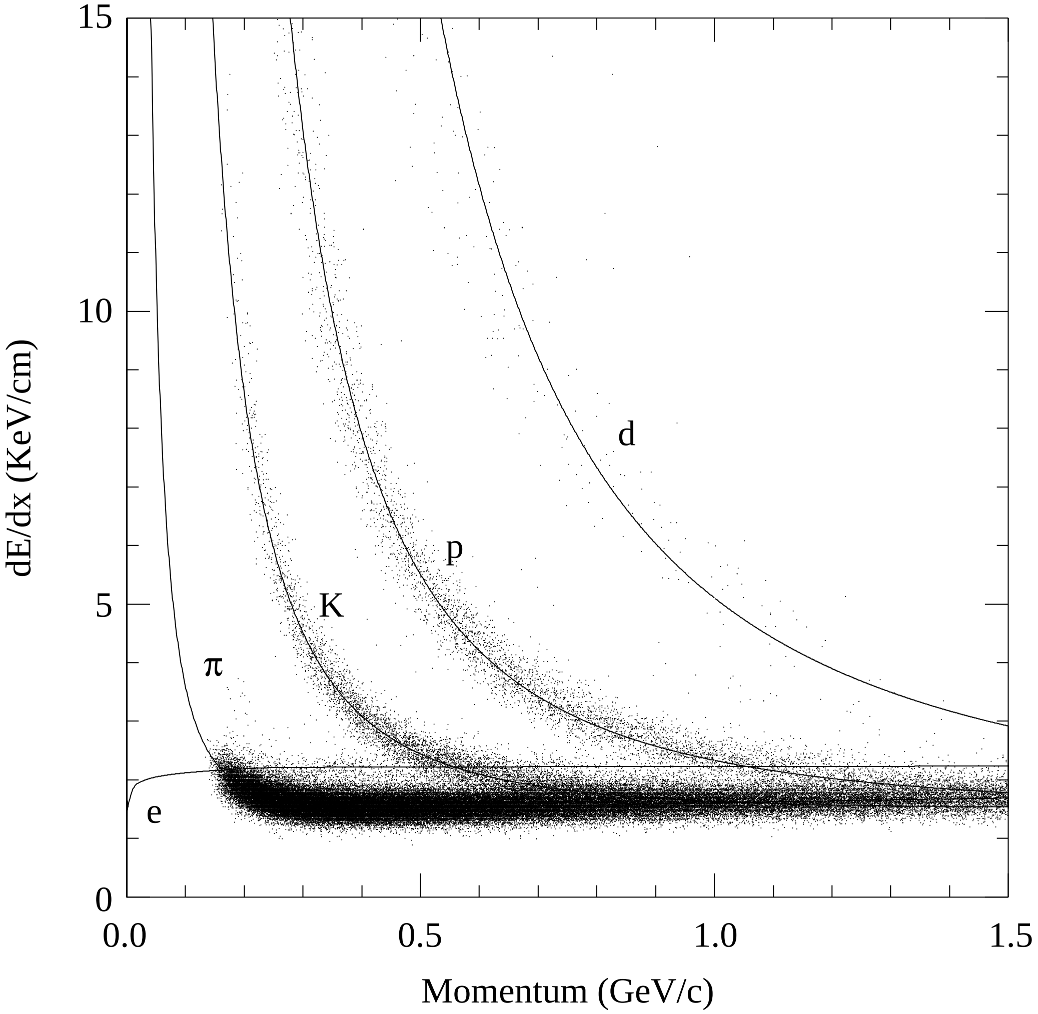

Figure 3.6: dE/dx

Layer	Radius (cm)	Wires	Angle (deg)	Layer	Radius (cm)	Wires	Angle (deg)
PTL 1	4.73	64	0	VD 1	8.47	64	0
2	5.15	64	0	2	9.22	64	0
3	5.60	64	0	3	10.04	64	0
4	6.10	64	0	4	10.93	64	0
5	6.64	64	0	5	11.91	64	0
6	7.23	64	0	6	12.78	96	0
				7	13.52	96	0
				8	14.31	96	0
				9	15.15	96	0
				10	16.03	96	0

Table 3.1: PTL and VD Wire Geometry

3.2.6 Time of Flight

The time of flight (TOF) system determines the species of the particle by measurement of its velocity, once the momentum is known from the curvature of the track within the tracking chambers. The TOF system is comprised of a barrel and an endcap portion.

The barrel TOF detector consists of 64 scintillation counters mounted just outside

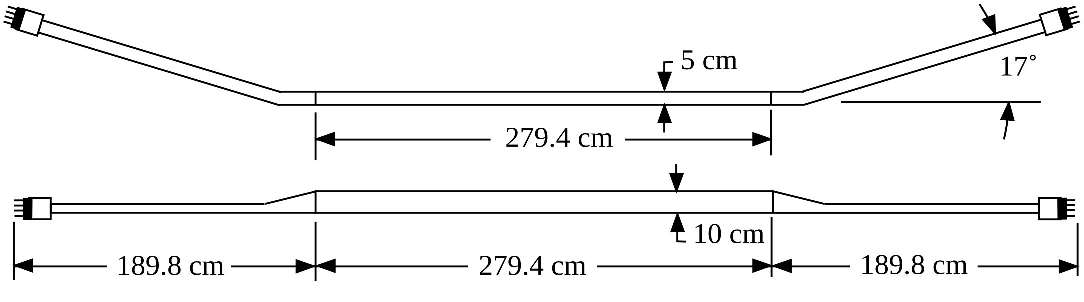

Figure 3.7: Barrel Time of Flight Counter

Layer	Radius (cm)	Wires	Angle (deg)	Layer	Radius (cm)	Wires	Angle (deg)
DR 1	19.90	96	0	DR 27	56.42	240	0
2	21.30	96	0	28	57.93	252	5.57
3	22.71	96	0	29	59.23	264	0
4	24.21	108	3.77	30	60.64	264	0
5	25.52	120	0	31	62.04	264	0
6	26.92	120	0	32	63.55	276	−6.01
7	28.33	120	0	33	64.85	288	0
8	29.83	132	−4.22	34	66.26	288	0
9	31.14	144	0	35	67.66	288	0
10	32.54	144	0	36	69.16	300	6.44
11	33.95	144	0	37	70.47	312	0
12	35.45	156	4.67	38	71.87	312	0
13	36.76	168	0	39	73.28	312	0
14	38.16	168	0	40	74.78	324	−6.45
15	39.57	168	0	41	76.09	336	0
16	41.07	180	−4.69	42	77.49	336	0
17	42.38	192	0	43	78.90	336	0
18	43.78	192	0	44	80.30	336	0
19	45.18	192	0	45	81.71	336	0
20	46.69	204	5.13	46	83.21	360	6.89
21	47.99	216	0	47	84.52	384	0
22	49.40	216	0	48	85.92	384	0
23	50.80	216	0	49	87.33	384	0
24	52.31	228	−5.56	50	88.73	384	0
25	53.61	240	0	51	90.14	384	0
26	55.02	240	0				

Table 3.2: DR Wire Geometry

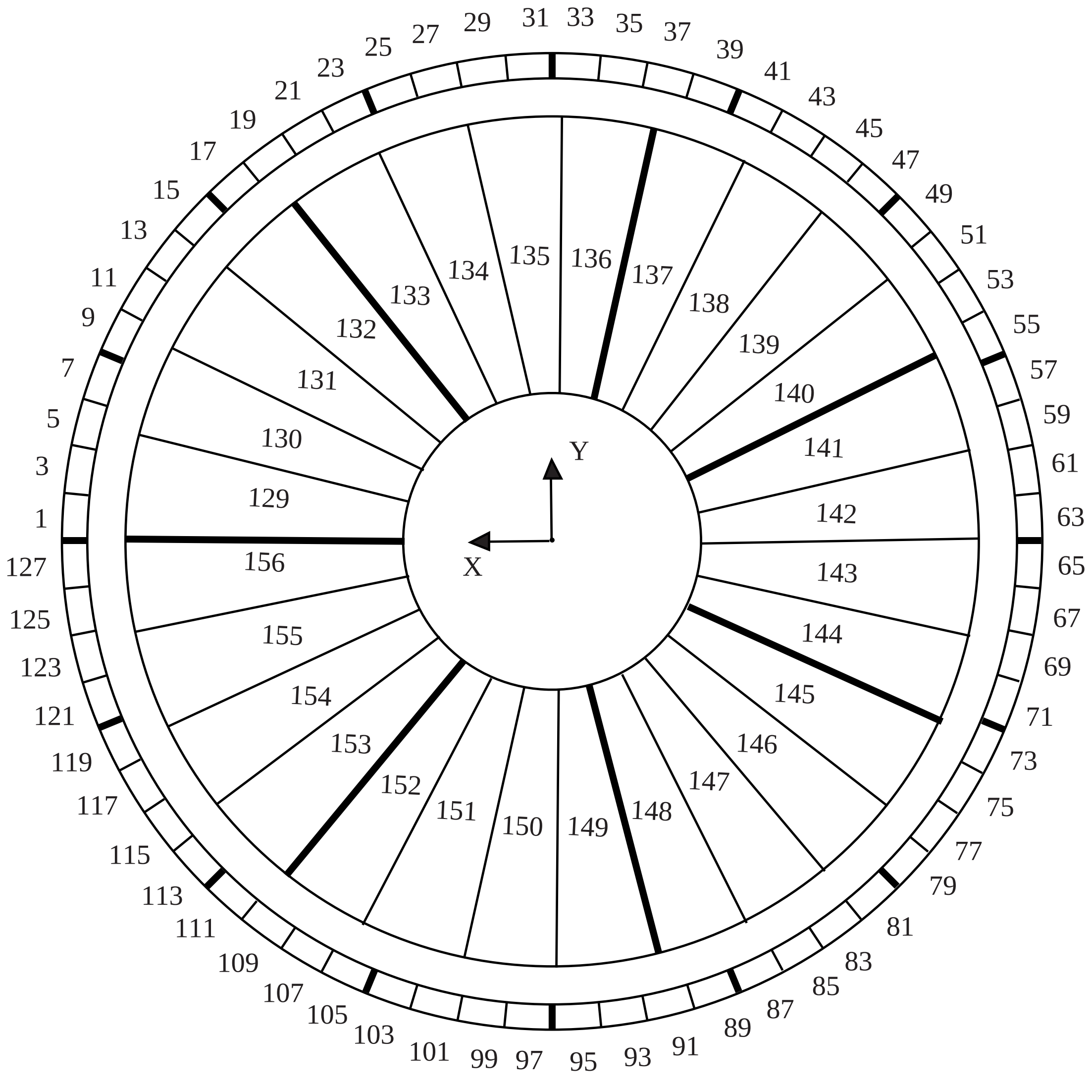

East TOF

Figure 3.8: Endcap Time of Flight Counters

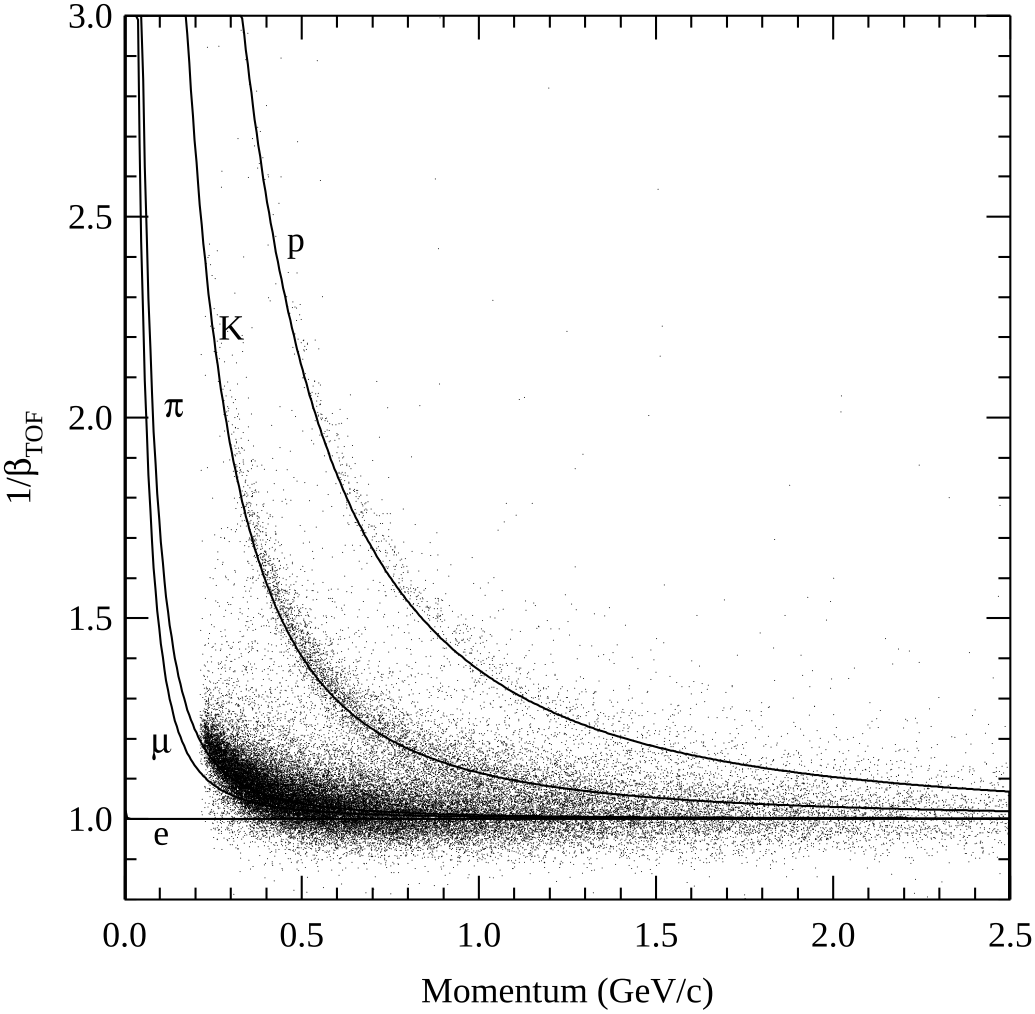

Figure 3.9: TOF

the DR, with a light guide and photomultiplier at each end. The light guides are necessary to keep the photomultiplier tubes operating safely away from the magnetic field of the detector. Figure 3.7 shows the geometry of a single counter. Bicron BC-408 is the material used in the counter, and the light pipes are constructed from lucite. The photomultiplier tubes are a variation of the standard Amperex 2020.

The endcap TOF detector is positioned just behind each end of the DR. At each end are 28 wedge-shaped scintillation counters, shown in Figure 3.8. The counters are read out with a single photomultiplier tube at the small end. These tubes are Hamamatsu proximity mesh type, and are designed to operate inside high magnetic fields. Unlike the barrel, the signals from the endcap photomultiplier tubes are subsequently amplified.

Figure 3.9 shows a plot of $1/\beta$ as a function of momentum where $\beta = v/c$ is velocity of the particle as measured by the TOF system. Bands are clearly visible for each particle species.

3.2.7 Electromagnetic Calorimeter

A hallmark of the CLEO II detector is its excellent capability to detect photons. The electromagnetic calorimeter is composed of 7800 cesium iodide crystals doped with thallium. The system is located just outside of the Time of Flight detector and is divided into barrel and endcap regions. The barrel portion contains 6144 trapezoidal crystals which are positioned such that they point towards the interaction region. Each endcap portion is composed of 828 rectangular crystals all with axes parallel to the z-axis of the detector, and thus lack the projective geometry found in the barrel crystals. The crystals are 30 cm deep, a thickness of 16 radiation lengths, and fully contain the electromagnetic shower. A 6mm thick UVT lucite window separates the back end of the crystal from four photodiodes, which detect the scintillation light from the crystal. The fourfold redundancy insures that isolated failures of photodiodes will not compromise the calorimeter performance. The four preamp signals from a single crystal are then summed and shaped before being sent to an ADC.

The energy resolution of the CLEO II calorimeter is excellent and for the barrel barrel can be summarized as

$$\frac{\sigma_E}{E}(\%) = \frac{0.35}{E^{0.75}} + 0.19 - 0.1E \tag{3.3}$$

where E is the photon energy in GeV. The resolution is about 1.5 % at 5 GeV and 3.8 % at 100 MeV. The endcap region is somewhat worse due to the drift chamber endplate in front of the crystals which causes showering to begin prematurely.

Not only is the energy resolution of the calorimeter exceptional, but the fine granularity permits very good resolution of position as well. This is critically important in order to reconstruct π^0 or η decays to $\gamma\gamma$. This is one of the great advantages of the CLEO II detector. For the barrel portion of the calorimeter, the angular resolution can be parameterized as

$$\sigma_\phi(\mathrm{mr}) = \frac{2.8}{\sqrt{E}} + 1.9, \qquad \sigma_\theta(\mathrm{mr}) = 0.8\sigma_\phi \sin(\theta). \tag{3.4}$$

The rms width of the π^0 invariant mass peak is approximately 5 MeV.

In this thesis, the usefulness of the calorimeter lies not in its ability to reconstruct neutrals, but in its ability to help identify electrons. The ratio E/p of the energy measured in the calorimeter to the momentum measured in the tracking chambers is a very powerful figure of merit for electron identification. An E/p close to 1 is consistent with an electron hypothesis since all of the electron's energy should be deposited in the calorimeter. Hadrons and muons have smaller E/p. This can be combined with other information from the calorimeter, and from the dE/dx measurement in the drift chamber to calculate a sum of log likelihood ratios $\mathcal{L}_e$ for the track to be an electron. We define it to be

$$\mathcal{L}_e = \sum_i \ln(P_{ei}/P_{\not{e}i}) \tag{3.5}$$

where P_{ei} is the probability that a track is an electron according to the i^{th} estimator, and $P_{\not{e}i}$ is the probability that the track is not an electron. A detailed discussion of the electron efficiency and hadron misidentification probability (fake rate) is given in reference [42].

3.2.8 Superconducting Solenoid

A magnetic field is required to measure the momentum of charged particles from their curvature. The CLEO II magnet is a superconducting solenoid providing a 1.5 Tesla axial field which is uniform to within ±0.2% over the volume of the Drift Chamber. The coil consists of two layers of 5 mm × 16 mm aluminum rectangular tubing containing a flat ribbon of Cu-Nb-Ti superconducting cable, wound on the inside surface of a 1.55 meter diameter aluminum cylinder. The inner layer of tubing contains an eleven strand ribbon, while the outer layer contains a ribbon of nine strands, all carrying a current of 3300 A. The entire system is cooled to a temperature of 4 Kelvin using a liquid helium circulation system. The flux return is provided by four layers of iron outside the magnet, each 36 cm thick, and which serve as absorbers for the muon detection system.

3.2.9 Muon Chambers

Between the iron layers for magnetic flux return are three superlayers of detectors for muon identification. Each superlayer consists of three sublayers of plastic Iarocci

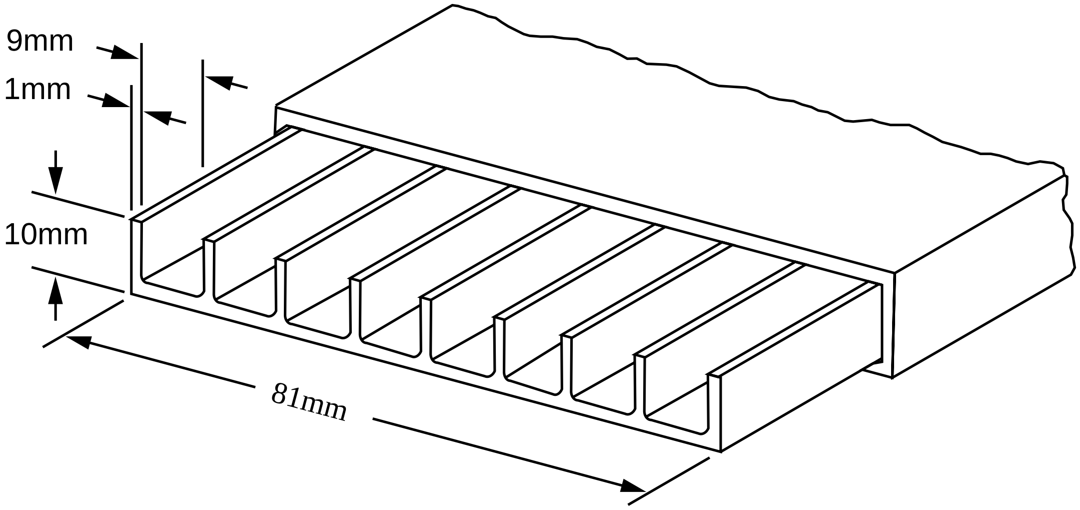

Figure 3.10: Cross section of muon chamber proportional tubes.

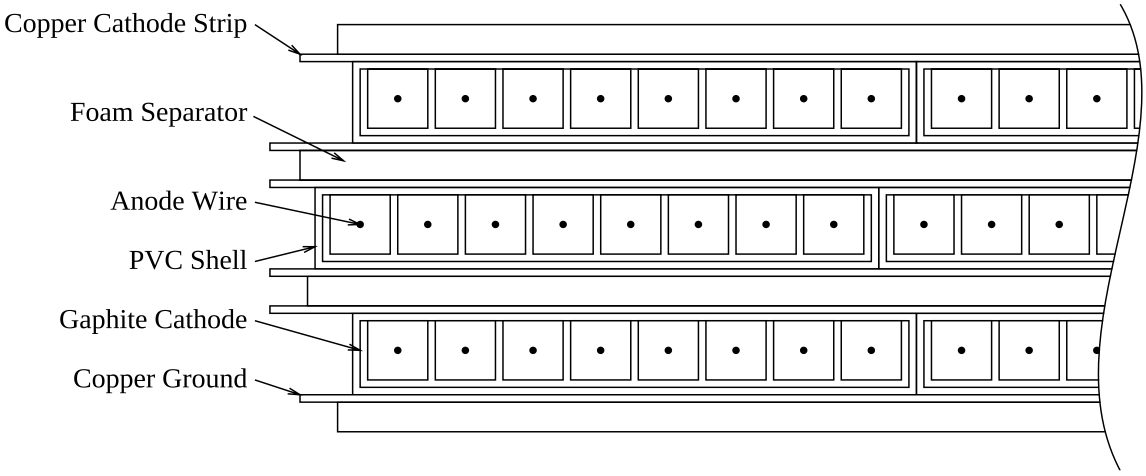

Figure 3.11: Cross section of one muon chamber superlayer.

tubes, shown in cross section in Figure 3.10. A 50 μm gold-plated tungsten anode wire runs down the center of each channel. The three sides of the plastic "comb" are coated with a layer of graphite to act as a conductive cathode. Copper strips run perpendicular to the anode wires on the side which is not coated by graphite. The spacing between copper strips is the same spacing as between the anode wires.

The tubes are filled with the same 50:50 argon-ethane mixture as is used in the main drift chamber and are operated in a proportional mode at 2500 V. The readouts from a number of neighboring counters and neighboring strips are ganged together at both ends through 100 Ω resistors. Charge division is the used to determine the coordinate of the hit, eliminating the need for a large number of readout channels. The spatial resolution obtained with this method is 2.4 cm for the counters. This resolution is adequate since it is smaller than the uncertainty in the projected track position at the muon chamber radius due to effects of multiple scattering.

The muon chambers are arranged in an octagonal geometry about the periphery of the CLEO II detector. The cross section of one superlayer is shown in Figure 3.11. An additional superlayer covers the endcap regions of the detector. The total coverage is 86% of 4π steradians. Depending on the direction of the particle, the total thickness of the iron represents between 7 to 10 nuclear absorption lengths.

A detailed description of the muon identification efficiency and of the muon fake rates are described in detail in reference [42].

3.2.10 Trigger

The crossing rate for bunches of electrons and positrons in CESR is 2.8 MHz, while the rate of interesting events is only about 10 Hz. It is not possible or desirable for the detector to record the results of each beam crossing. A hierarchy of triggers select interesting events to be written to tape. The Level 0 (L0) trigger is fast, receiving inputs from the time of flight counters, from the vertex detector, and from the electromagnetic calorimeter. The rate of events passed by L0 is of order 10 kHz.

After a L0 trigger, all detector gating is disabled, and a search is made for a L1 requirement. L1 takes information from the time of flight scintillators, from the vertex detector, from the drift chamber and from the calorimeter. Approximately 1.5 μs is required for all information to be ready for the L1 decision, and thus a deadtime of 2% is introduced. If the L1 requirement is not satisfied, the system is reset and detector gating resumes. The rate of events passed by L1 is of order 50 Hz.

The L2 trigger takes inputs from the vertex detector and drift chamber and performs detailed pattern recognition to reject events due to interactions of the beam with the beam pipe or with residual gas molecules. L2 decreases the event rate by a factor of between two and four. As with L1, if the requirements of L2 are not met, gating resumes.

The final level if event filtering is L3, and occurs in software after the entire event has been read out by the detector, but not yet written to tape. It uses detailed information from reconstructed events, and reduces the event rate by as much as 50%.

3.2.11 Monte Carlo

An important tool used to make the measurements in this thesis is a simulated dataset produced by a computerized Monte Carlo simulation of $\Upsilon(4S)$ decays and of the CLEO II detector response. For this thesis, the Monte Carlo is used primarily to understand backgrounds. The information that will be obtained from the Monte Carlo is not terribly sensitive to the details of the simulation, so only a brief overview will be presented here.

The production of the simulated data occurs in three steps. The first step occurs within a program called QQ which uses a random number generator to decides the complete decay chain of an $\Upsilon(4S)$ event, determining the 4-momenta of all particles involved. The probability for a particle to decay into a given mode is given by a table of measured branching fractions and, when measurements are not available, predictions. Portions of total decay rates that are unaccounted for are filled in by a fragmentation routine JETSET 7.3 from CERN. All particles are decayed except for those which are expected to pass through the beampipe before themselves decaying.

The decay history output of the QQ program is then passed through a program called CLEOG, based on the package GEANT from CERN. CLEOG simulates the complete detector response to the event. Those particles which are not decayed within QQ are handled here, such as decays in flight of μ and K. All manner of detailed processes are simulated in CLEOG in order to make the simulated data match the true data as accurately as possible. The program simulates the energy loss of the particles while passing through the matter of the detector, the electromagnetic showering within the calorimeter, and the ionization of the drift chamber gas. Random noise hits in the various detectors is modeled by adding hits from randomly triggered events in data.

The simulation of the lepton identification in the Monte Carlo is especially relevant to this thesis. If a track is known to be an electron from tagging routines, a value for the log-likelihood $\mathcal{L}_e$ is randomly selected from the $\mathcal{L}_e$ distribution measured for electrons in data. This distribution is found by embedding radiative bhabha events

$e^+e^- \to e^+e^-\gamma$ in hadronic events, and recording the $\mathcal{L}_e$ value for the track known to be the scattered bhabha electron. If in the Monte Carlo a track is known to be a hadron, a value of $\mathcal{L}_e$ is chosen randomly instead from the distribution found in continuum-subtracted $\Upsilon(1S)$ events. The muon identification simulation uses the wire and strip efficiencies measured in data. Additionally, noise hits are added to the muon chambers from randomly triggered events in data. The simulated Monte Carlo muon efficiency is found to match that of the data to the level of a few percent.

The third and final step of the Monte Carlo production is to process the simulated data with the identical program as is used on the genuine data.

Chapter 4

Mixing

4.1 Introduction

In this chapter, a measurement of the $\overline{B^0} - B^0$ mixing parameter χ_d is presented. First, the dilepton method of measuring mixing at the Υ(4S) is discussed. The limitations of this method will motivate the need for a tagged measurement, and the tagged analysis will be presented.

It is important to reiterate that this measurement is performed at a center of mass energy corresponding to the Υ(4S) resonance. There is an important consequence to consider which affects the mixing measurement at $\overline{B}B$ production threshold. The B meson pairs are created in a coherent $L = 1$ state with $C = -1$, the same quantum numbers as those of the virtual photon. The $L = 1$ relative orbital angular momentum wave function is antisymmetric. The $\overline{B^0}\,B^0$ state cannot evolve to $B^0\,B^0$ or $\overline{B^0}\,\overline{B^0}$ because a symmetric wave function would be required by Bose-Einstein statistics. Therefore, the probability than an event created as $\Upsilon(4S) \to \overline{B^0}\,B^0$ will decay as

$B^0\,B^0$ or $\overline{B^0}\,\overline{B^0}$ is simply χ_d

$$\chi_d = \frac{N(B^0\,B^0) + N(\overline{B^0}\,\overline{B^0})}{N(\overline{B^0}\,B^0) + N(B^0\,B^0) + N(\overline{B^0}\,\overline{B^0})} \qquad \text{at the } \Upsilon(4\text{S}). \tag{4.1}$$

Given a value of χ_d, one must take the measured B lifetime $\tau_B = 1/\Gamma_B$ from higher energy experiments to determine ΔM.

A well-established method for measuring mixing at the Υ(4S) is to examine events where both B's decay semileptonically. The semileptonic decay of a B meson allows the charge of the constituent bottom quark to be cleanly determined from the charge of the observed lepton. Decays of the type $\overline{B} \rightarrow X l^- \bar{\nu}$ with a lepton of negative charge indicate that the B meson contained a b quark, while $B \rightarrow X l^+ \nu$ is the signature of a $\bar{b}$ antiquark.

In this method, events are examine with two leptons (dilepton) both with a momentum above some minimum required value. A pair of opposite-sign leptons is the signature of either a $B^-\,B^+$ or an unmixed $\overline{B^0}\,B^0$ event, while two like-sign leptons indicate that the event is mixed ($B^0\,B^0$ or $\overline{B^0}\,\overline{B^0}$). High momentum leptons are required in order to exclude those from secondary decays of charm, $\overline{B} \rightarrow D \rightarrow X l \nu$, which incorrectly tag the flavor of the parent B and can result in a false mixing signal.

This method of dileptons can not distinguish between events containing charged and neutral B's. As a result, the contribution to the opposite-sign dileptons from $B^-\,B^+$ events must be taken into account when calculating the mixing probability χ_d. At the Υ(4S),

$$\chi_d = \left(\frac{1}{1-\Lambda}\right) \frac{N(\ell^\pm \ell^\pm)}{N(\ell^+ \ell^-) + N(\ell^\pm \ell^\pm)}, \tag{4.2}$$

where $N(\ell^\pm \ell^\pm)$ is the number of like-sign primary lepton pairs, and $N(\ell^+ \ell^-)$ is the number of unlike-sign pairs. The parameter Λ is equal to the fraction of all primary lepton pairs from $B^- \, B^+$ events

$$\Lambda = \frac{f_+ b_+^2}{f_+ b_+^2 + f_0 b_0^2}. \tag{4.3}$$

Here f_+ and f_0 are the production fractions for charged and neutral B pairs at the Υ(4S), and b_+ and b_0 are the semileptonic branching fractions of charged and neutral B's, respectively,

$$f_+ \equiv \mathrm{Br}(\Upsilon(4\mathrm{S}) \to B^- \, B^+) \tag{4.4}$$

$$f_0 \equiv \mathrm{Br}(\Upsilon(4\mathrm{S}) \to \overline{B^0} \, B^0) \tag{4.5}$$

$$b_+ \equiv \mathrm{Br}(B^- \to X \ell^- \bar{\nu}) \tag{4.6}$$

$$b_0 \equiv \mathrm{Br}(\overline{B^0} \to X \ell^- \bar{\nu}). \tag{4.7}$$

Recent experimental data suggest that Λ is near 0.5, consistent with theoretical expectations, but the uncertainty on its value represents the largest contribution to the systematic error on mixing measurements by this method. In 1993 at the time this analysis was performed, estimates of $\Delta\Lambda/\Lambda$ were at the level of 15%. From equation 4.2, it is seen that the relationship between the fractional change in Λ and χ_d can be summarized by the following rule

$$\Delta\chi_d/\chi_d \simeq -\Delta\Lambda/\Lambda \tag{4.8}$$

for dilepton measurements. It is this large uncertainty which is the motivation for seeking an alternative method.

4.2 Motivation for $\overline{B^0}$ Tagging

In principle, all dependence on Λ would be eliminated if the event sample contained only $\overline{B^0}$ events.[1] The ability to select such events requires some form of *tagging*,

---

[1] Charge conjugation is implied throughout this thesis.

or identification of a $\overline{B^0}$. In this approach, a specific decay mode of the $\overline{B^0}$ is reconstructed. Having done this, one has not only established that the event contains a pair of neutral rather than charged B's, but also the flavor of the tagged B is also known.[2] If the remaining B decays semileptonically, then the charge of the lepton identifies the second B's flavor, determining whether the event is unmixed or mixed. Tag backgrounds from B^-B^+ events are inevitable, but if the neutral B purity of the tag is sufficiently high, the residual Λ dependence is no longer the dominant source of systematic uncertainty.

A tag of the decay $\overline{B^0} \to D^{*+}l^-\bar{\nu}$, $D^{*+} \to D^0\pi^+$ has been developed through correlations of l^- and π^+ which is used to obtain a statistically useful sample of events enriched in neutral B. This tag is used to measure $\overline{B^0} - B^0$ mixing.

4.2.1 Reconstruction of $D^{*+}\ell^-\overline{\nu}$

The exceptionally low momentum of B's produced in Υ(4S) decays is exploited in a technique called *partial reconstruction* where the momentum of an undetected neutrino in an exclusive semileptonic decay channel is inferred by conservation of momentum and energy. This method has been used to study the decay mode $\overline{B^0} \to D^{*+}l^-\bar{\nu}$. In this case, all final decay products except for the neutrino are detected. The mass of the neutrino may be calculated given the four-momenta:

$$\begin{aligned} M_\nu^2 &= E_\nu^2 - P_\nu^2 = (E_{\text{beam}} - E_l - E_{D^*})^2 - |\vec{P}_B - \vec{P}_l - \vec{P}_{D^*}|^2 \\ &= (E_{\text{beam}} - E_l - E_{D^*})^2 - |\vec{P}_l + \vec{P}_{D^*}|^2 - P_B^2 + 2\vec{P}_B \cdot (\vec{P}_l + \vec{P}_{D^*}). \end{aligned} \tag{4.9}$$

This quantity is also known as the square of the *missing mass* and should equal zero if the decay has been properly reconstructed. The only unknown quantity in the above expression is the direction of motion of the B. The contribution of the last two terms

---

[2] The $\overline{B^0}$ tag decay mode must not be accessible from B^0 as well, $\overline{B^0} \to J/\psi\, K_s$ for example.

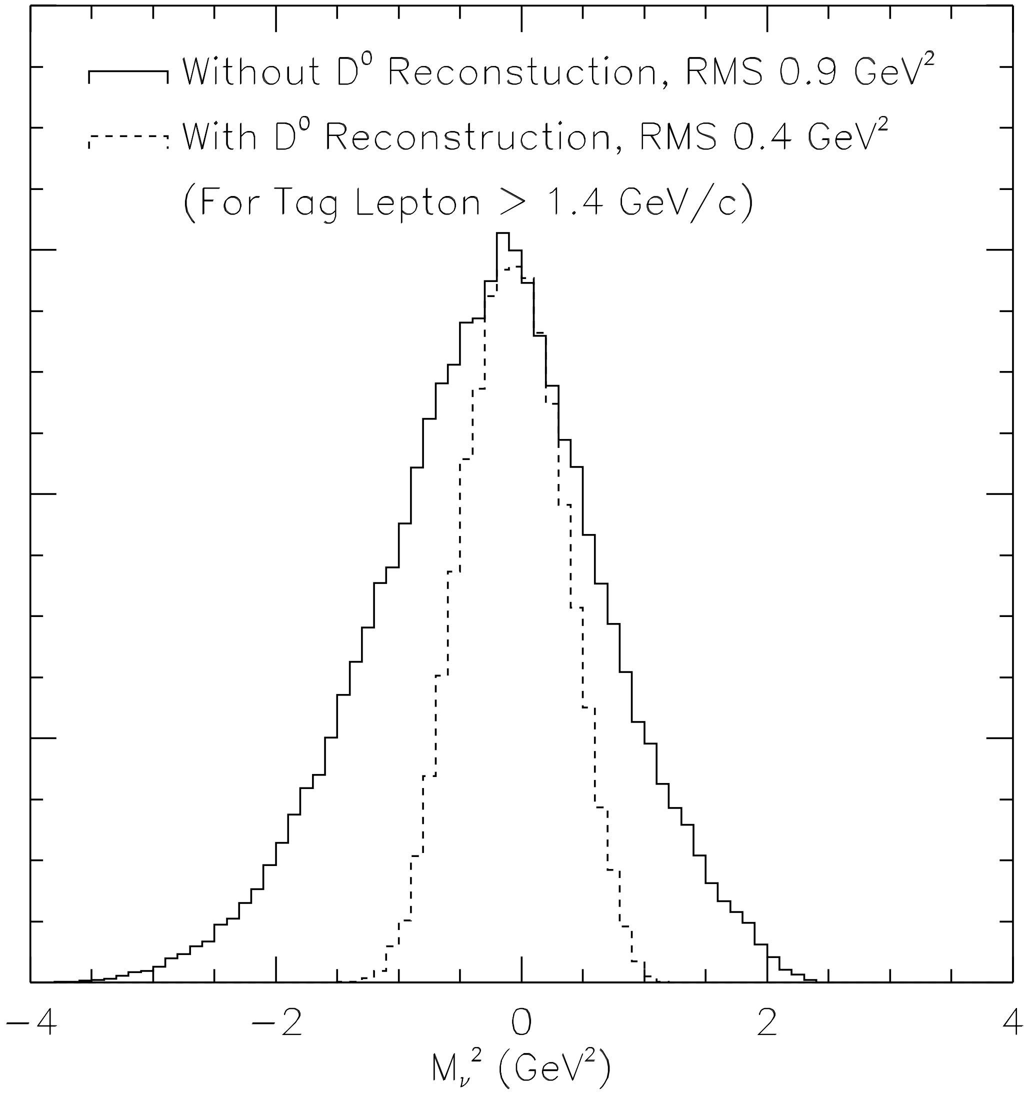

Figure 4.1: $\widetilde{M}_\nu^2$ signal with and without D^0 reconstruction for tag lepton momentum $>$ 1.4 GeV/c

can be estimated, using the known magnitude of $|\vec{P}_B| = 300$ MeV/c. Averaged over many events, this is found to be ~ 0.002 GeV^2. Approximating $|\vec{P}_B| = 0$ does not significantly shift the mean value of M_ν^2 from zero, but it does introduce an rms width of ~ 0.4 GeV^2, as shown in the dashed curve of Figure 4.1.

4.2.2 Without D^0 reconstruction

The method may be carried one step further by tagging the decay $D^{*+} \rightarrow D^0\pi^+$ using *only* the π^+ without reconstructing the D^0 decay. This approach is possible due to the extremely low decay energy of this mode, which leaves the π^+ nearly at rest in the D^{*+} center of mass frame. As a consequence, the π^+ alone carries sufficient information to determine an approximate four-momentum of the D^{*+}, so no D^0 reconstruction is needed. The sample can be increased by a significant factor by not requiring the D^0 reconstruction. For example, the single mode $D^0 \rightarrow K^-\pi^+$ is often used in the reconstruction. The branching fraction for this mode is 4%. Assuming a reconstruction efficiency of 50%, a factor of 50 in sample size would be gained if D^0 reconstruction were not required.

If the π^+ produced in the decay $D^{*+} \rightarrow D^0\pi^+$ were precisely at rest in the D^{*+} center of mass frame, the energy of the D^{*+} could be obtained by scaling the pion energy by the ratio of the D^{*+} and π^+ masses, Additionally, the direction of the π^+ in the lab would coincide with the direction of the parent D^{*+}. Of course this is not actually the case and the actual momentum P_π^{CM} of the soft π^+ in the D^{*+} center of mass is not zero, but 39 MeV/c. Therefore in this technique, the energy scaling rule is modified slightly from that described above, but the laboratory directions are still taken to be the same. These two approximations are examined as follows.

Energy approximation

At CLEO, the laboratory frame is the $\Upsilon(4S)$ rest frame. If the D^{*+} energy in the laboratory is $E_{D^*} = \gamma m_{D^*}$, then the energy of the π^+ in the laboratory is given by a Lorentz transformation

$$E_\pi = \gamma(E_\pi^{CM} + \beta P_\pi^{CM} \cos\theta), \tag{4.10}$$

where $E_\pi^{CM} = 145$ MeV is the energy of the π^+ in the D^{*+} rest frame and θ is the decay angle of the π^+ in the D^{*+} rest frame with respect to the D^{*+} direction in the laboratory. Averaging over all θ, the contribution from the second term drops out and the mean energy in the laboratory is simply γE_π^{CM}. Therefore, the approximation is made that

$$\gamma \simeq \frac{E_\pi}{E_\pi^{CM}} \equiv \tilde{\gamma}. \tag{4.11}$$

The rms spread of true values γ about $\tilde{\gamma}$ depends on the polarization of the D^{*+}. Figure 4.2 shows the ratio $(\tilde{\gamma} - \gamma)/\gamma \equiv \delta\gamma/\gamma$ for unpolarized and polarized D^{*+} with a momentum spectrum as predicted by the the model of Isgur *et al.*. For an unpolarized D^{*+}, then γ, and the D^{*+} energy, is obtained with ≈ 8% uncertainty,

$$E_{D^*} \simeq \frac{E_\pi}{E_\pi^{CM}} M_{D^*} \equiv \widetilde{E}_{D^*}. \tag{4.12}$$

This approximation is better for D^{*+} of helicity $= \pm 1$ than for D^{*+} of helicity $= 0$, as the pions are preferentially emitted towards $\cos\theta = 0$ and consequently experience the same boost as the D^{*+}.

Direction approximation

The second approximation made is that the direction of motion of the D^{*+} is the same as that of the soft π^+. Again, the precision of this approximation depends on the

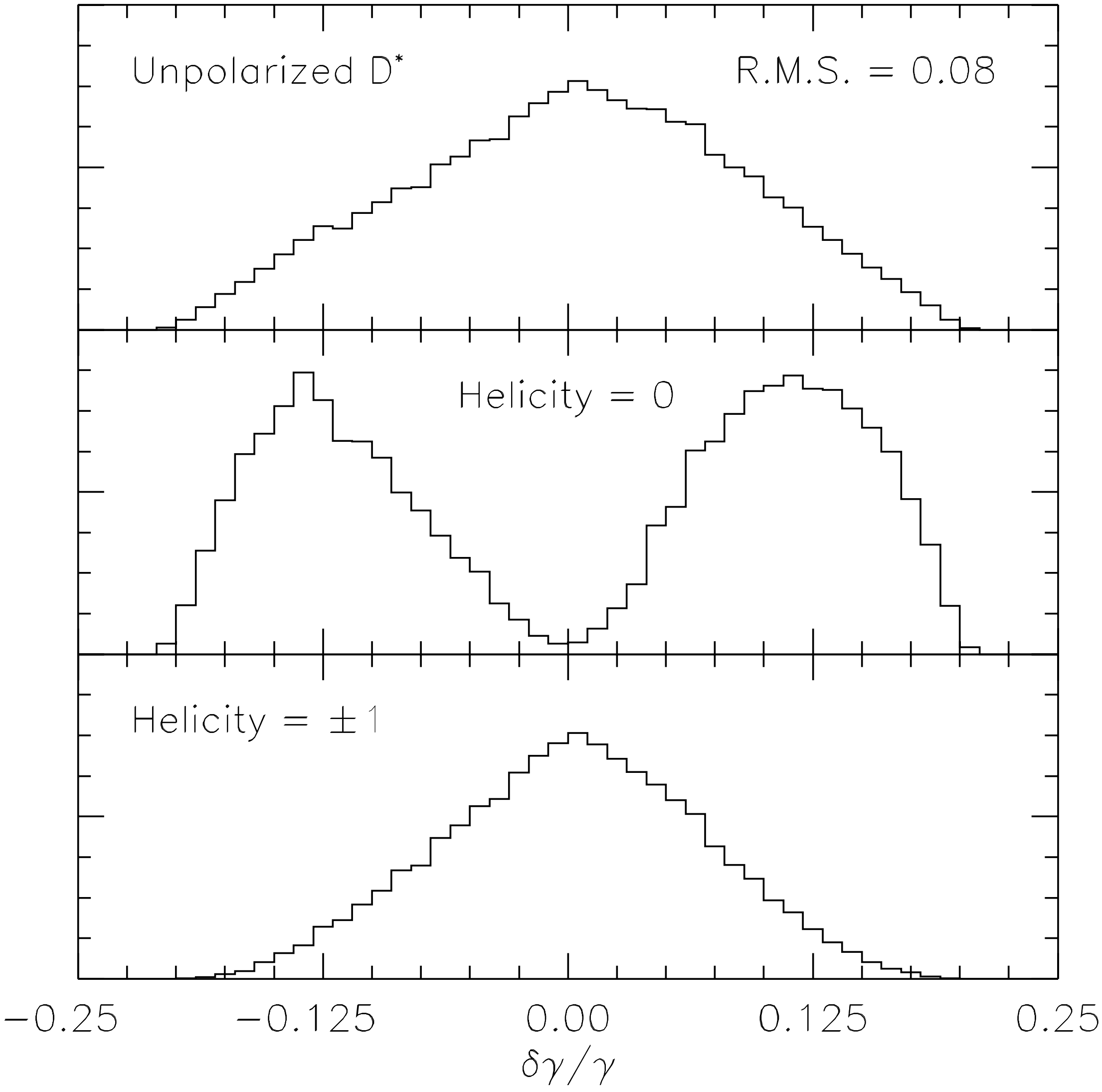

Figure 4.2: Error on gamma approximation

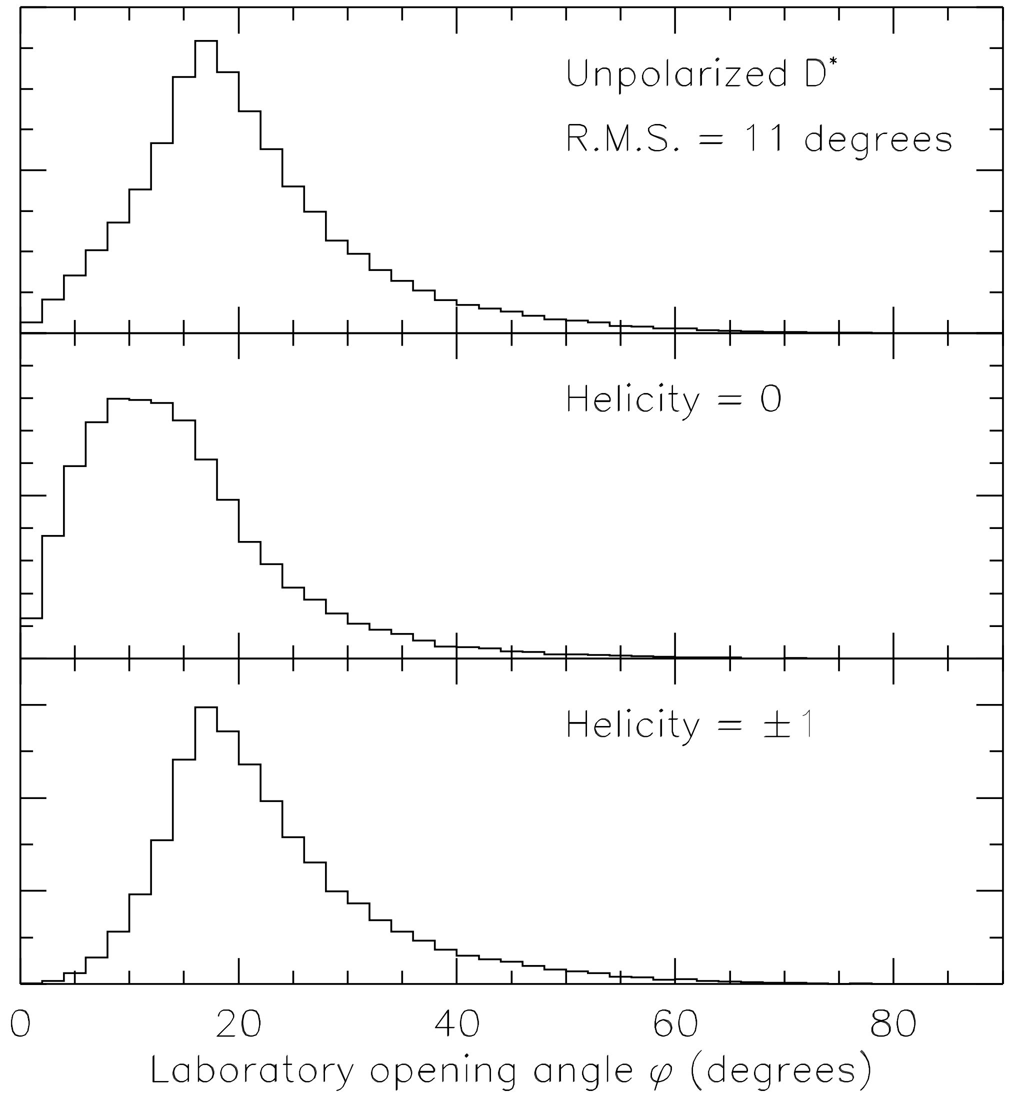

Figure 4.3: Opening angle ϕ between D^{*+} and π^+ directions in the laboratory.

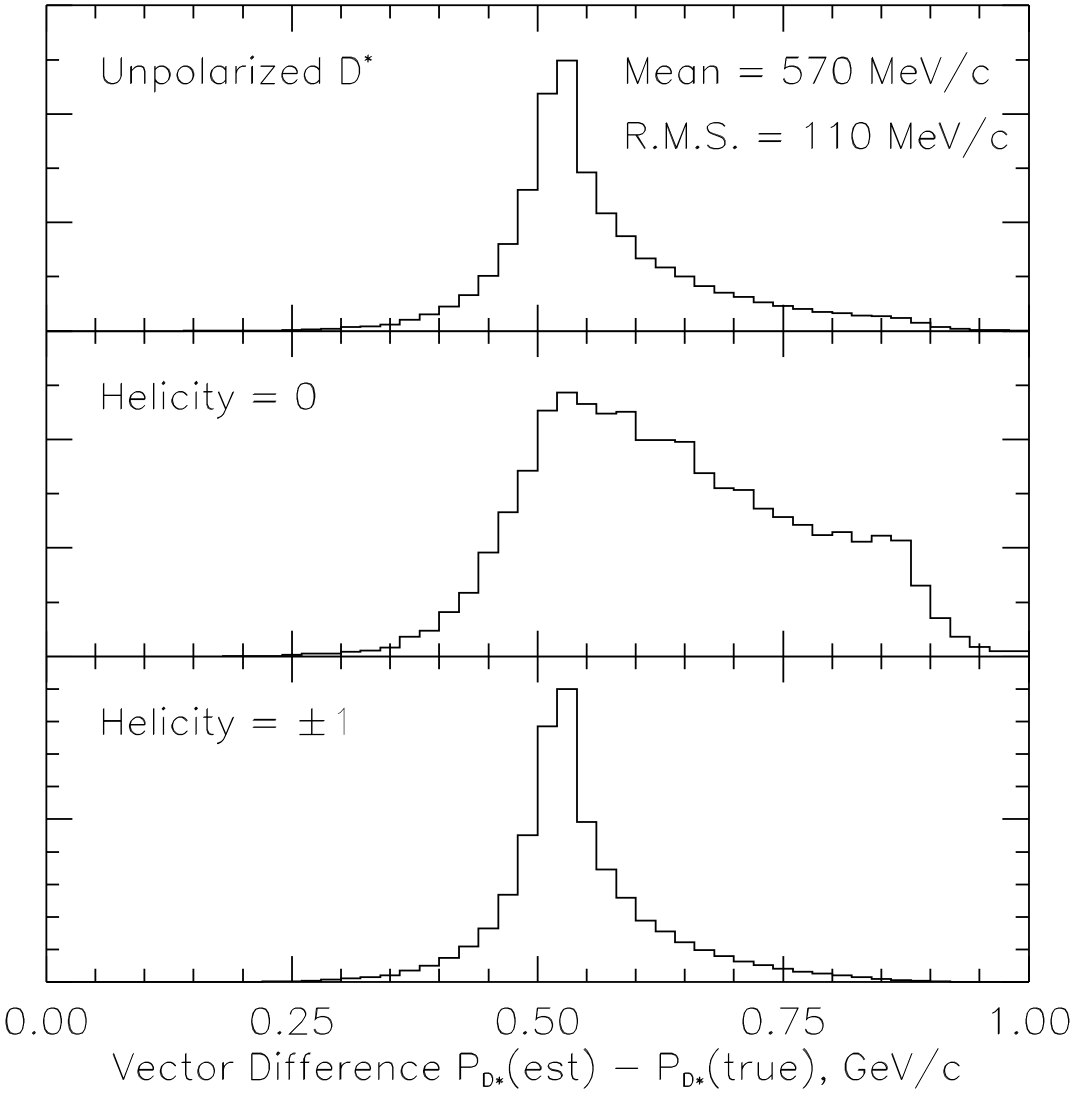

Figure 4.4: Vector difference of estimated minus true D^{*+} momentum.

shape of the momentum spectrum of the D^{*+} and its polarization. The distribution of opening angle ϕ between the laboratory directions of the D^{*+} and π^+ is shown in Figure 4.3, using a Monte Carlo with unpolarized D^{*+}'s ($\Gamma_{\mathrm{L}}/\Gamma_{\mathrm{T}} = 0.5$) which has a momentum spectrum described by the model of Isgur *et al.*. In this case, the rms value for ϕ is found to be 11 degrees. This approximation is better for D^{*+} of helicity $= 0$, where the π^+ is preferentially emitted parallel or antiparallel to the boost axis.

The approximate D^{*+} momentum is then obtained simply via

$$\widetilde{\vec{P}}_{D^*} = \frac{\sqrt{\widetilde{E}^2_{D^*} - M^2_{D^*}}}{|\vec{P}_\pi|}\vec{P}_\pi. \tag{4.13}$$

Figure 4.4 shows the magnitude of the vector difference of the estimated and actual D^{*+} momenta. The error in the D^{*+} momentum derived by making these two approximations is ~ 600 MeV/c.

The squared missing mass distribution,

$$\widetilde{M}^2_\nu \equiv (E_{\mathrm{beam}} - \widetilde{E}_{D^*} - E_\ell)^2 - (\widetilde{\vec{P}}_{D^*} + \vec{P}_\ell)^2, \tag{4.14}$$

is then an approximation of the neutrino mass. In comparison the momentum of the B is ~ 300 MeV/c. One would therefore expect that the $\widetilde{M}^2_\nu$ distribution obtained with this method should not be much wider than twice the 0.4 GeV^2 found for the full reconstruction. Indeed, in Monte Carlo simulations it is found to be ~ 0.9 GeV^2, shown as the solid curve in Figure 4.1.

4.3 Analysis Overview

The mixing analysis can be summarized as follows. Oppositely charged leptons and pions are paired and $\widetilde{M}^2_\nu$ is calculated. If $\widetilde{M}^2_\nu \simeq 0$, then the spectrum of any remaining leptons is examined, separately for leptons which are the (1) opposite and

(2) same charge as the lepton in the tag. Both spectra are fitted in order to determine the number of primary leptons in each. Lastly, the ratio of primary lepton yields is related to χ_d. The remainder of this section is devoted to presenting the major issues encountered during each of these steps.

The $\widetilde{M}_\nu^2$ distribution has a striking peak at $\widetilde{M}_\nu^2 = 0$ (GeV/c^2)^2 from properly partially reconstructed decays. There is also a background in the same region of roughly the same size as the signal due to random combinations of ℓ^- and π^+. Because both properly reconstructed tags and random combinations are used in this measurement, it is necessary to understand their origins. To determine the number of tags in the peak and in the random background, the $\widetilde{M}_\nu^2$ distribution is fitted using two models of the background shape each of which is extrapolated into the region of signal, $\widetilde{M}_\nu^2 > -2$ (GeV/c^2)^2.

The peak has contributions not only from the decay $\overline{B^0} \to D^{*+} l^- \bar{\nu}$, but also from $\overline{B^0} \to D^{*+} \pi^0 l^- \bar{\nu}$ and $B^- \to D^{*+} \pi^- l^- \bar{\nu}$. In the latter two decays, the pion produced with the D^* is not reconstructed, but the value of $\widetilde{M}_\nu^2$ is still close to zero. The sum of the second and third decays is set to be the fixed fraction f^{**} of the total peak, with the two contributing in proportion to the isospin phase space, production rate and semileptonic branching fractions, respectively.

The random background has components with leptons from $\overline{B^0}$ and B^- primary and, to a smaller degree, secondary decays. $\overline{B^0}$ and B^- events contribute to the random background at different rates. The number of contributions per event is determined by monte carlo, and differ for charged and neutral B events due to differences in the mean multiplicity of low-momentum pions of the correct relative charge. Background tags from unmixed and mixed $\overline{B^0}$ events also differ and are treated separately. These components are fixed to contribute to the measured random background size in proportion to their tagging efficiencies, and respective production and semileptonic decay fractions.

If the tag candidate has a value of $\widetilde{M}_\nu^2 > -2$ GeV^2, then a search is made for any additional leptons in the event. The yield of additional leptons for random background tags is lower than that for peak tags. This phenomenon is discussed in some detail in Section 4.5.2. Consequently, there is a factor called the effective efficiency for the random background which describes this reduction in yield of additional leptons. The effective efficiencies are determined from monte carlo separately for random background tags from charged B events, unmixed and mixed neutral B events. It is important to account for this effect in order to correctly determine the size of the charged B contamination in the tag sample.

The yield of additional leptons is plotted as a function of momentum. These are separated into two cases, where the additional lepton has the opposite charge as the tag lepton (*unlike*-sign spectrum), and where the additional lepton has the same charge as the tag lepton (*like*-sign spectrum). Each spectrum is then fitted to a sum of spectra for primary $\overline{B} \to clX$ and secondary $\overline{B} \to cX, c \to slY$ decays to obtain a value for the primary components N_{-+} and N_{--}. The quantity of interest is the *ratio* M of primary areas in the like and unlike-sign spectra, and it is related to the mixing parameter χ_d.

The total unlike-sign and like-sign signals are linear in the parameter χ_d, and each is proportional to the sum of contributions from their respective sources. Each source is the product of three quantities (1) a fraction of tags (2) a tagging efficiency and (3) an effective efficiency. Their ratio $M = N_{++}/N_{-+}$ depends only on known parameters and on χ_d. One finds a linear relationship of the general form

$$\chi_d = \frac{aM - b}{cM + d} \tag{4.15}$$

where a, b, c and d are functions of known parameters.

It is tempting to consider somehow subtracting the contribution from the random background. One flawed scheme would be to repeat the mixing analysis selecting on the $\widetilde{M}_\nu^2$ distribution obtained using same sign $\ell^+\pi^+$ pairs (called the wrong-sign $\widetilde{M}_\nu^2$ distribution) to define the tag, record the spectra of additional leptons, and then finally to subtract these spectra from those found using the correct sign tags. Naïvely this would be the spectra of additional leptons for signal tags only, simplifying matters substantially. The reason that this scheme fails is that the right-sign random background of the signal region may have contributions from charged and neutral B events in different proportions than would occur in the wrong-sign distribution in the same region of $\widetilde{M}_\nu^2$. In this case, it would not be appropriate to use the wrong-sign sample to estimate the charged/neutral composition of the background under the right-sign peak. If one proceeded to do the subtraction, one would over-subtract neutral B background and under-subtract charged B background, or vice versa. This is verified in Monte Carlo simulations. In fact, it is found that contributions depend on whether a neutral B event is mixed or unmixed. Therefore, no attempt is made to directly subtract the effects of the random background using some other region of the $\widetilde{M}_\nu^2$ distributions. Instead, Monte Carlo events are used to estimate the relative sizes of the charged versus neutral B contributions to the random background of the right-sign $\widetilde{M}_\nu^2$ distribution as described earlier. Much of the intricacy of this analysis involves the detailed understanding of these contributions.

There is another approach to the mixing measurement which can be considered where the complications of tagging efficiency and effective efficiency for the random tag background are avoided. The method is similar to the one used in Chapter 5 for the measurement of the $\overline{B^0}$ semileptonic branching fraction. In this approach, one forms a $\widetilde{M}_\nu^2$ distribution in the usual way, but rather than requiring a minimum value of $\widetilde{M}_\nu^2$ and plotting the spectrum of additional leptons, one instead requires a minimum momentum of an additional lepton and then plots the $\widetilde{M}_\nu^2$ distribution for cases where the two leptons are same and opposite sign and fits for the size of the peak in both plots. This method was used by the ARGUS collaboration to measure mixing[43]. Although this is a simpler approach, it was not chosen because the statistical error would have been unacceptably large compared to the results of a separate analysis on the same data, the standard dilepton measurement. The method used here was chosen instead to have an overall uncertainty which was competitive with the other result.

4.4 Data and Selection Criteria

This measurement is based on an integrated luminosity of 951 pb^{-1} on the $\Upsilon(4S)$ and 455 pb^{-1} at an energy on the continuum below the $\Upsilon(4S)$, the `4S1` through `4S3` datasets. Events are required to have a ratio of Fox-Wolfram moments[44] `R2GL`[3] $\equiv H_2/H_0$ less than 0.4 and to pass our standard hadronic event criteria (`KLASGL` = 10)[45].

The selection requirements on the tag lepton, the tag pion and the additional lepton are summarized in Table 4.1. The 1.4 GeV/c momentum requirement on the tag lepton rejects secondary leptons from charm decays. The 0.19 GeV/c requirement on the pion is slightly below the upper kinematic limit for pions from $\overline{B} \to D^{*+}X \to D^0\pi^+$. Electrons in the tag are are allowed to fall in any fiducial region. The fiducial requirement on the muons eliminates the outermost endcap re-

---

[3] Throughout this thesis, terminology which is used internally by the CLEO collaboration will be set in `typewriter` font. These terms are defined in Appendix C.

gion where the monte carlo and offline analysis had not been modeling the muon detection efficiency correctly at the time of this analysis. The tag lepton identification requirements are somewhat less stringent than those typically used for inclusive lepton analyses, but the requirement of the soft pion correlation reduces the rate at which fake tag leptons enter the sample. The loosened tag lepton requirements increase the sample size by some 20%.

The second lepton in the event must satisfy the same tracking requirements as the tag lepton. Unlike the lepton in the tag, tighter identification cuts are used for these additional leptons, where the efficiency is better known. To eliminate false mixing signals from double tracking, leptons which make an angle θ with the tag lepton such that $\cos\theta > 0.95$ are discarded.

Figures 4.5 and 4.6 shows a candidate mixed event in data. The two tracks which form the tag are the 2.0 GeV/c electron candidate at top, and the 0.15 GeV/c pion candidate which is emitted nearly opposite to the electron. The second lepton in the event is the 1.7 GeV/c muon, which is the same sign as the tag lepton. Since the lower lepton momentum of 1.7 GeV/c is sufficiently high to virtually exclude contamination from charm decay, this is almost certainly a mixed $\overline{B^0}\,\overline{B^0}$ event.

4.5 Composition of Tags

Tag candidates are formed by pairing identified leptons with pions of opposite charge. These candidates will be referred to as *right-sign*. Lepton/pion pairs of the same charge will be referred to as *wrong-sign*. Figure 4.7 shows the $\widetilde{M}_\nu^2$ distributions observed in data after subtracting continuum contributions. A clear enhancement is seen in the right-sign $\widetilde{M}_\nu^2$ distribution near zero. The corresponding plot with

Tag Lepton	$1.4 < p_\ell < 2.5$ GeV/c
	$\texttt{KINCD} = 0$
	$\texttt{NHITPT} > 0$
	$\texttt{NHITVD} > 0$
	$\texttt{RHITDR} > 0.4$
	At least two of the following three
	$\lvert\texttt{DBCD}\rvert < 5$ mm
	$\lvert\texttt{Z0ZD}\rvert < 5$ cm
	$\texttt{RESICD} < 0.6$ mm
(electrons)	$\texttt{R2ELEC} > 3$
(muons)	$\lvert\texttt{CZCD}\rvert < 0.79$
	$\texttt{MUQUAL} = 0$
	$\texttt{DPTHMU} > 3$ if $p_\ell < 1.5$ GeV/c
	$\texttt{DPTHMU} > 5$ otherwise
Tag Pion	$p_\pi < 0.19$ GeV/c
	$\texttt{KINCD} = 0$
	$\lvert\texttt{SGPIDI}\rvert < 2$
	$\texttt{IQALDI} = 1$ or -2
Second lepton	$\texttt{KINCD} = 0$
	$\texttt{NHITPT} > 0$
	$\texttt{NHITVD} > 0$
	$\texttt{RHITDR} > 0.4$
	At least two of the following three
	$\lvert\texttt{DBCD}\rvert < 5$ mm
	$\lvert\texttt{Z0ZD}\rvert < 5$ cm
	$\texttt{RESICD} < 0.6$ mm
	$\cos\theta_{\ell\ell} < 0.95$
(electrons)	$\texttt{R2ELEC} > 3$
	$\lvert\texttt{CZCD}\rvert < 0.707$
(muons)	$\texttt{MUQUAL} = 0$
	$\texttt{DPTHMU} > 5$
	$\lvert\texttt{CZCD}\rvert < 0.79$

Table 4.1: Selection criteria for tags

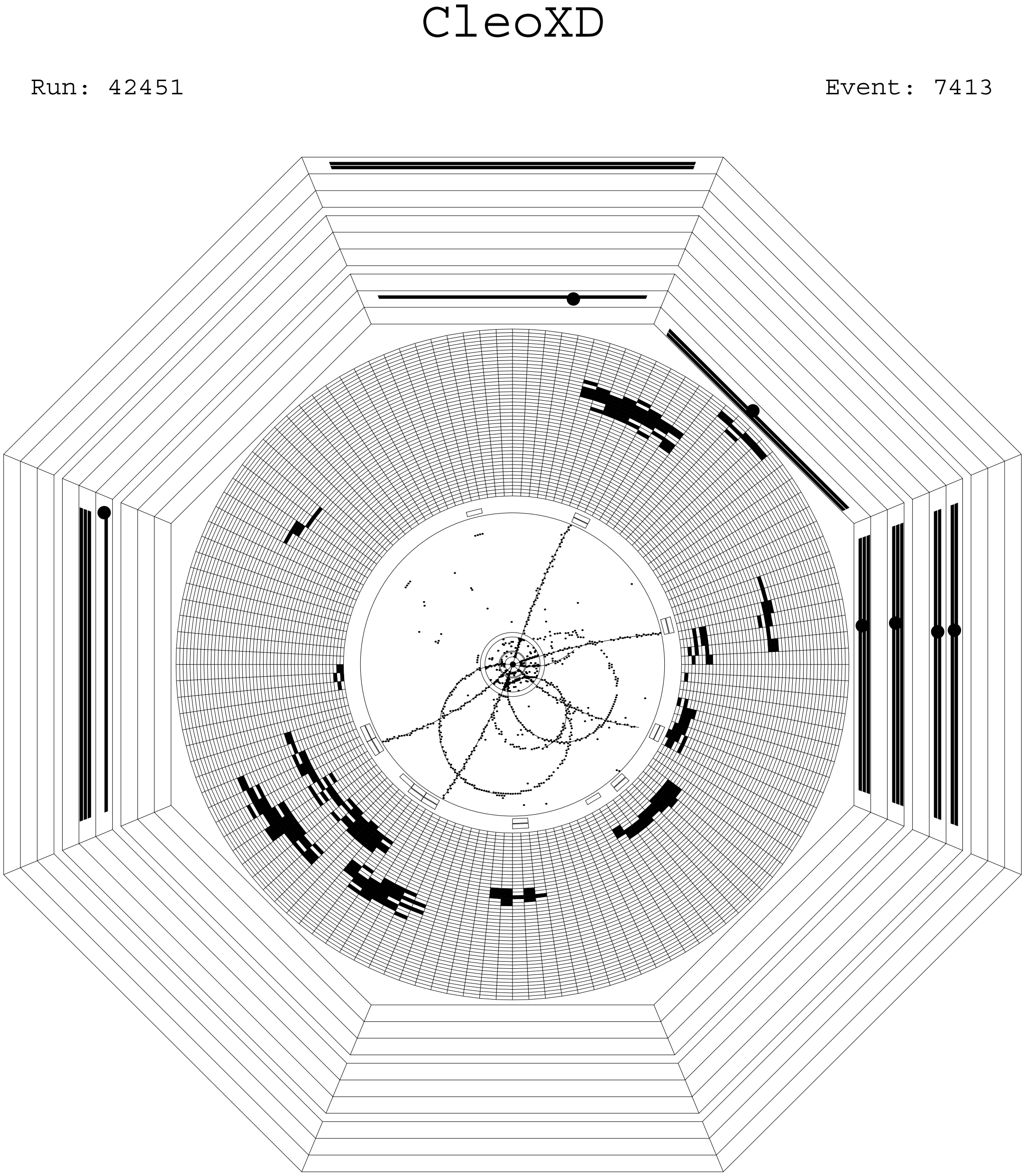

Figure 4.5: A candidate mixed event in data, cross section view of the CLEO detector.

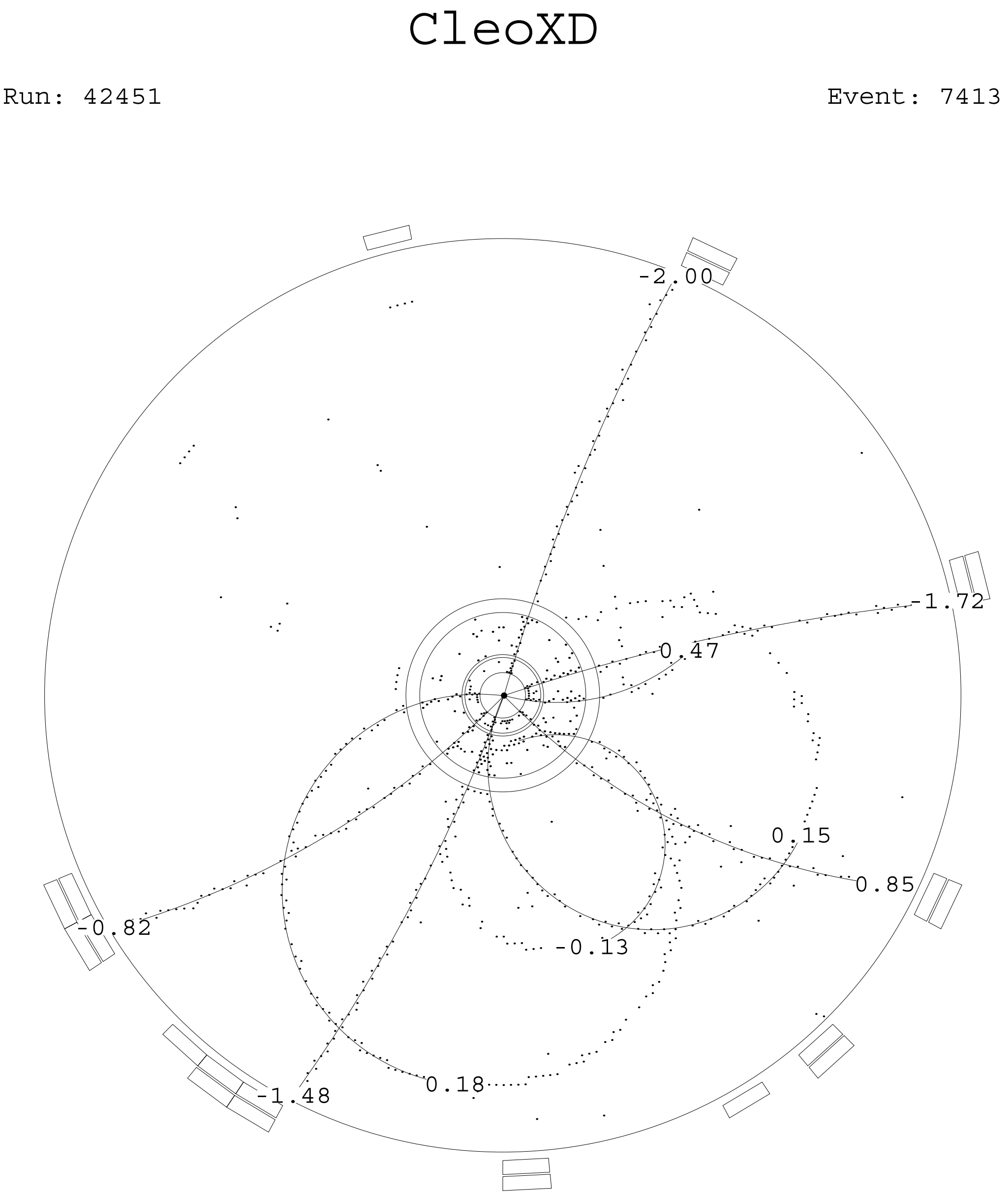

Figure 4.6: A candidate mixed event in data, detailed view. The numbers indicate the signed momentum of each track. The tag is the 2.00 GeV/c electron at top recoiling against the 0.15 GeV/c pion at bottom. The additional lepton is the 1.72 GeV/c muon at right.

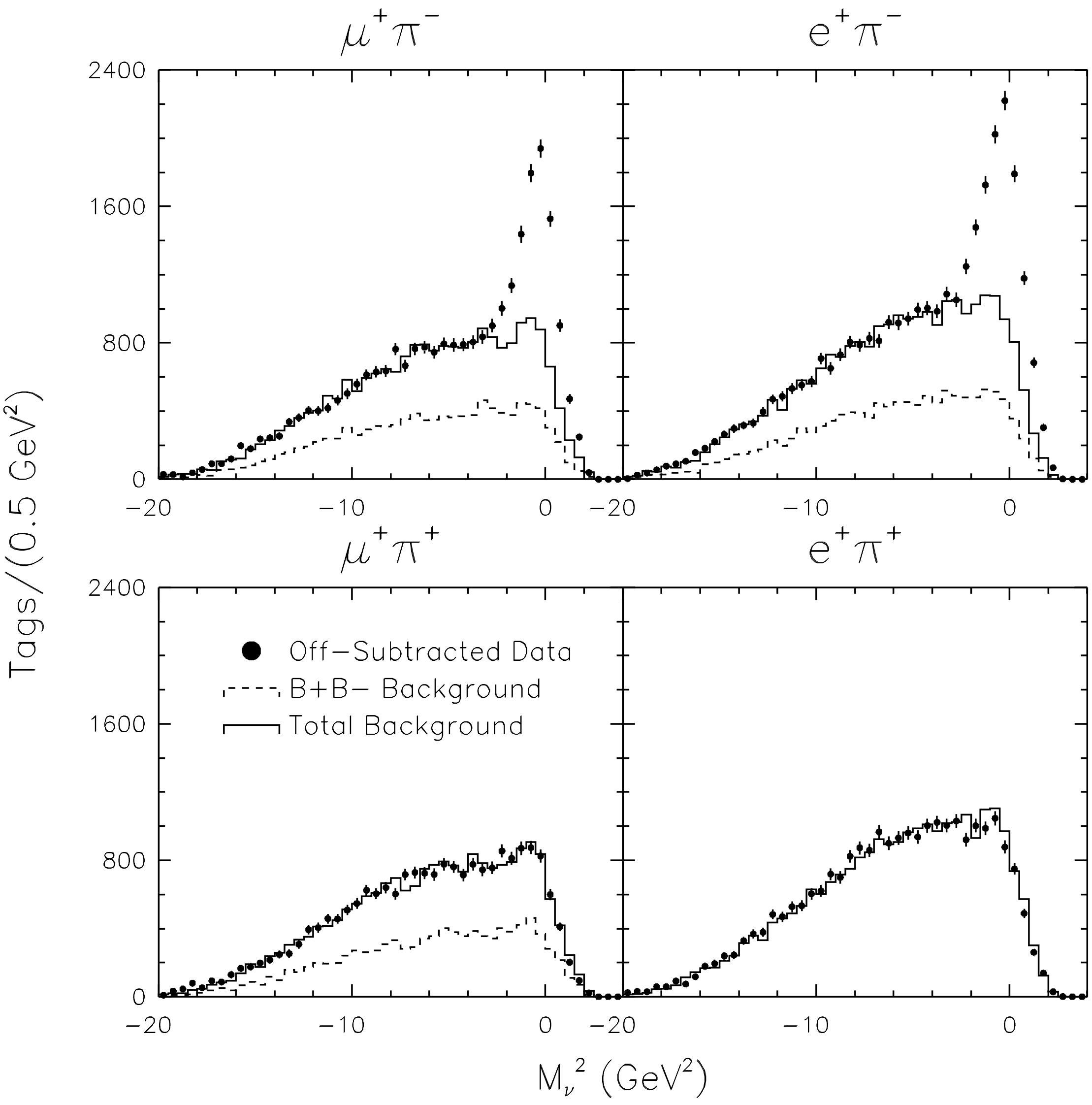

Figure 4.7: $\widetilde{M}_\nu^2$ distributions in data. The points are the off-resonance subtracted data, the solid curve is the estimated monte carlo background fitted in the sideband region, the dashed curve is the portion of the background from B^+B^- events.

the wrong-sign candidates shows no such enhancement. For the purpose of studying background the region $-2\ \mathrm{GeV}^2 < \widetilde{M}_\nu^2$ is designated as the *signal* region and $-20\ \mathrm{GeV}^2 < \widetilde{M}_\nu^2 < -4\ \mathrm{GeV}^2$ as the *sideband* region. After passing the various selection requirements made in data the candidates remaining in the right sign signal region comprise the tag sample.

Background distributions obtained from Monte Carlo are overlaid, with the dashed histogram representing the $B^- B^+$ contribution, and the solid representing the total background, including the neutral B, assuming that $f_+ = f_0 = 0.5$ and that $\chi_d = 0.161$. Agreement between data and Monte Carlo of the background shape, both in sideband and wrong-sign distributions, is good. The absolute rate per $\overline{B}B$ event is in reasonable agreement; the ratio of the data to Monte Carlo for right-sign sidebands is 1.03 ± 0.02 for muons and 1.07 ± 0.02 for electrons, and for wrong-sign distributions is 0.97 ± 0.01 and 1.03 ± 0.01 for muons and electrons, respectively. The fact that these normalizations are close to unity indicates that the Monte Carlo is doing a reasonable job of reproducing the same soft pion multiplicities as in data.

To understand the composition of the tags, it is necessary to evaluate the size of the background. The shape of the random background may be estimated by looking either at (1) the wrong-sign distribution in data, or (2) the right-sign background simulated in Monte Carlo. A study of events generated via Monte Carlo simulation indicates that the wrong-sign distribution is a rough representation of the background shape in the right-sign distribution,[4] and justifies method (1). In both methods, the distribution which models the background is overlaid on the right-sign distribution in data, taking the number of candidates in the signal region of each, and adjusting

---

[4] As will be seen in Chapter 5, the shapes of the right-sign and wrong-sign distributions differ slightly in the region $\widetilde{M}_\nu^2 = 0$, but this was not fully appreciated at the time of the mixing measurement.

by a scaling factor determined by fitting the sideband. The systematic error on the number of random tags is taken to be the variance of the two numbers from the mean. After the size of the background is estimated using either of these two methods, the number of tags in excess of the random background is designated the *peak* and the remainder *random*.

The raw and net numbers of tags are given in Table 4.2. The fraction of random background in the tag sample is found to be

$$F^R = 0.512 \pm 0.007 \pm 0.019. \tag{4.16}$$

4.5.1 Peak candidates

Of the tags in the signal region, those in the peak arise from true D^*-lepton correlations in B decay. Contributions from decays other than the tag $\overline{B} \to D^{*+}\pi\ell^-\overline{\nu}$ should occur in the partial reconstruction tag at the same level as in the tag where the D^0 is reconstructed. The process which must be considered is the decay $\overline{B} \to D^{*+}\pi l^-\bar{\nu}$ where the additional pion is not detected and the $D^{*+}\pi$ may or may not form a D^{**} state.[5] In this case, the B can be either charged or neutral, so it may result in contamination of the peak by charged B's. Isospin symmetry assigns 2/3 of such events to B^- and 1/3 to $\bar{B}^0$. This can be understood by considering the four resonant modes

$$\overline{B^0} \to D^{**+}\ell^-\overline{\nu}, \qquad D^{**+} \to D^{*+}\pi^0$$

$$\overline{B^0} \to D^{**+}\ell^-\overline{\nu}, \qquad D^{**+} \to D^{*0}\pi^+$$

$$B^- \to D^{**0}\ell^-\overline{\nu}, \qquad D^{**0} \to D^{*+}\pi^-$$

---

[5] Here, the term D^{**} loosely refers to all excited D states with $L \geq 1$.

$$B^- \to D^{**0}\ell^-\overline{\nu}, \qquad D^{**0} \to D^{*0}\pi^0.$$

Assuming that $f_0 = f_+$ and $b_0 = b_+$, then from isospin symmetry the number of decays in each mode are in the proportions 1:2:2:1, respectively. Since only the first and third modes contain a D^{*+} which could feed into our signal, the feeddown from B^- is twice the size as the feeddown from $\overline{B^0}$. A similar argument holds for the corresponding nonresonant modes such as $\overline{B^0} \to D^{*+}\pi^0\ell^-\overline{\nu}$. The overall contribution from the process $\overline{B} \to D^{*+}\pi l^-\bar{\nu}$, resonant as well as nonresonant, was found in reference [46] to comprise 0.17 ± 0.10 times the contribution from $\overline{B^0} \to D^{*+}l^-\bar{\nu}$, or

$$f^{**} = 0.14 \pm 0.08 \tag{4.17}$$

times the total peak size. The charged B content is then $2\alpha f^{**}/(1+2\alpha) = 9.6 \pm 5.6\%$ of the total peak, for $\alpha \equiv f_+b_+/f_0b_0 = 1.0$. These three contributions to the peak are given in Table 4.4.

4.5.2 Sources of random candidates

The random background consists of three classes of events, those where the lepton is from primary $b \to c\ell\nu$ decay, those where the lepton is from secondary $c \to X\ell\nu$ decay, and those containing a fake lepton. The contributions to the tags from the various random sources are listed in Table 4.5.

Primary leptons

To determine the relative abundance of charged and neutral events in the random background of the signal region, the probability $\epsilon^{\rm tag}$ per event to populate the random background in the signal region is determined separately for $\overline{B^0}\,B^0(\epsilon_u^{\rm tag})$, $\overline{B^0}\,\overline{B^0}(\epsilon_m^{\rm tag})$ and $B^-\,B^+(\epsilon_+^{\rm tag})$ events. We call these quantities *tagging efficiencies*. Note that unmixed and mixed neutral B events are treated separately. Since the overall size of the random background is measured, the absolute values of the three tagging efficiencies are unimportant. We are only interested in their relative magnitudes, described as two separate ratios of tagging efficiencies

The tagging efficiencies are a measure of the multiplicity of low momentum right-sign charged pions in the event. If a large number of such pions are available, it is easier to form a background tag, resulting in a higher tagging efficiency. Using a sample of 800,000 Monte Carlo events, we find that

$$\frac{\epsilon_{+}^{\mathrm{tag}}}{\epsilon_{u}^{\mathrm{tag}}} = 0.97 \pm 0.03 \tag{4.18}$$

$$\frac{\epsilon_{m}^{\mathrm{tag}}}{\epsilon_{u}^{\mathrm{tag}}} = 1.18 \pm 0.07 \tag{4.19}$$

where the errors are due to monte carlo statistics only. Because we are only interested in the *ratios* of tagging efficiencies, the monte carlo need only determine the *relative* abundances of pions correctly to determine these parameters. Nonetheless, the Monte Carlo does predict the absolute rates correctly, as shown at the start of Section 4.5.

The somewhat higher probability per event for obtaining random background tags in mixed events is due to an extra source not present in unmixed events. These are pions from the second B if it decays via $\overline{B^0} \to D^{*+}X$, $D^{*+} \to D^0\pi^+$. Not only do these pions have the desired sign, but there is a high probability that they have a sufficiently low momentum to pass our requirements. This contribution to the random background does not normally exist in unmixed events, since such a pion would be of the wrong sign.[6]

To illustrate the application of tagging efficiency ratios, consider the case where $f_+ = f_0$ and $\chi_d = 1/7 \simeq 0.143$. In this scenario, the relative abundance of

---

[6] Unless the D^{*+} comes from the W hadronization in the second B decay. This would be a Cabibbo suppressed process if no additional quarks are popped.

charged:unmixed:mixed decays produced would be 7:6:1. The tagging probabilities state that the relative sizes of the charged:unmixed:mixed contributions to the random background in the signal region would be $7\frac{\epsilon_{+}^{\rm tag}}{\epsilon_{u}^{\rm tag}}:6:\frac{\epsilon_{m}^{\rm tag}}{\epsilon_{u}^{\rm tag}}$.

Secondary leptons

Random background tags containing a lepton from secondary rather than primary B decay are studied separately, as they can give an incorrect flavor tag and possibly a false mixing signal. The two principal sources of such leptons are from $\overline{B} \rightarrow cX, c \rightarrow slY$, and $\overline{B} \rightarrow \bar{c}X, \bar{c} \rightarrow \bar{s}lY$ Leptons from $\overline{B} \rightarrow \bar{c}X, \bar{c} \rightarrow \bar{s}lY$ (anticharm quark from the W hadronization) have a momentum spectrum similar to those from $\overline{B} \rightarrow cX, c \rightarrow slY$, but do not result in an incorrect flavor tag of the B. We take the fraction of leptons in $\overline{B}B$ events above 1.4 GeV/c from both c and $\bar{c}$ sources to be $f_{c+\bar{c}} = 2.8 \pm 0.8\%$, of which

$$f_c = (0.92) f_{c+\bar{c}} = 2.6 \pm 0.8\% \tag{4.20}$$

are from $\overline{B} \rightarrow cX, c \rightarrow slY$.[42]

There is one small asymmetry which is not significant given the statistics of the present data set. Charged and neutral B's each decay to both charged and neutral D's. However, $\overline{B^0}$ decay more readily to D^+ than do B^-. Since D^+ has a larger semileptonic branching fraction than D^0, a larger proportion of leptons from secondary decays is expected to originate from $\overline{B^0}$ than from B^-. The effect of this asymmetry on the final result is very small, and it is assumed that charged and neutral B's contribute equally to the total number of secondary leptons.

Fake leptons

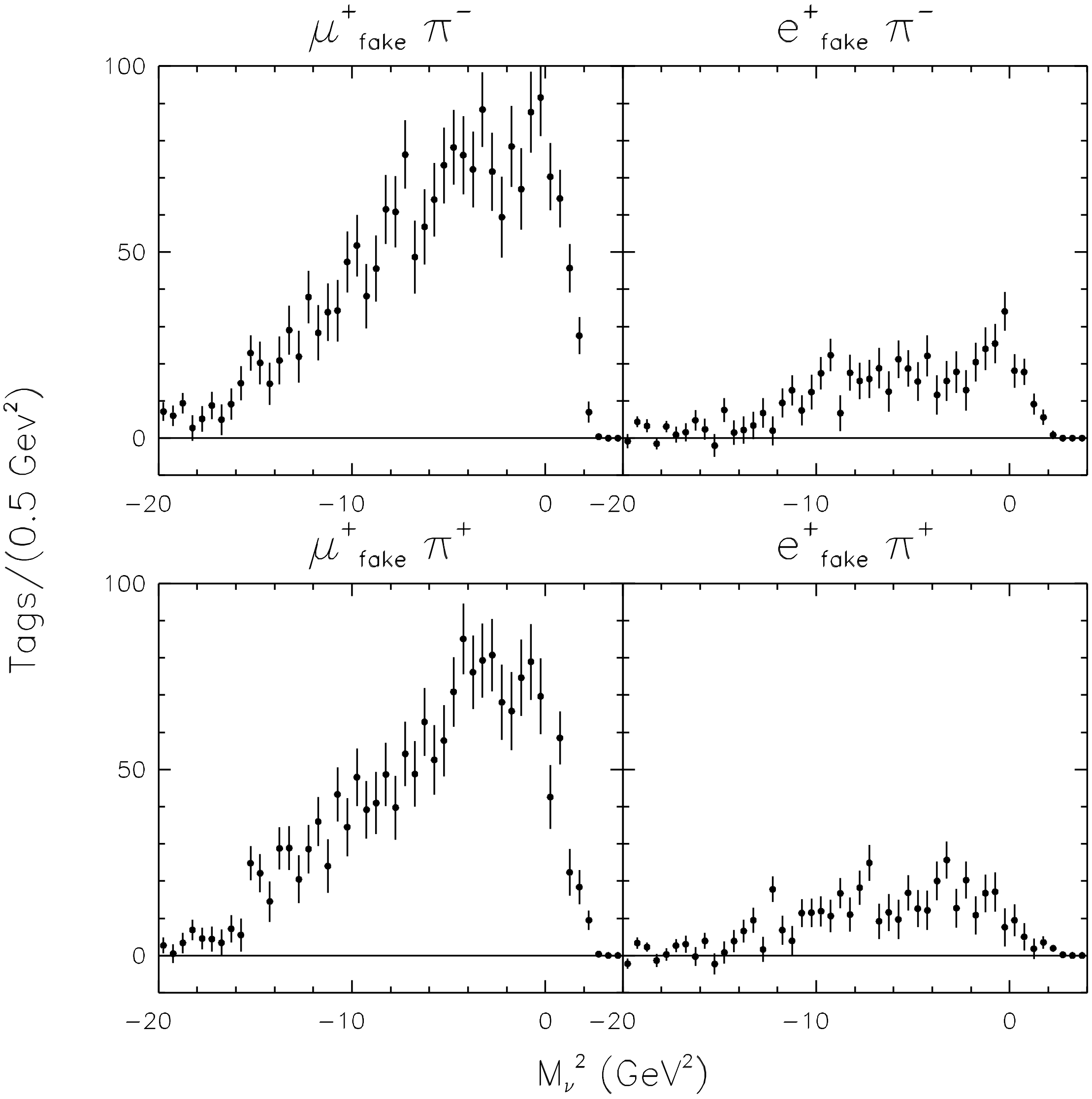

Figure 4.8: $\widetilde{M}_\nu^2$ distributions for tags with fake leptons, off-resonance subtracted. Note the change in vertical scale from Figure 4.7.

Finally, a random background tag containing a lepton candidate which is in fact a misidentified hadron may or may not be correlated with the flavor of its parent B.[7] The rate at which such hadrons enter the tag sample may be studied directly using data in which the lepton candidate enters the fiducial region for lepton identification but does not pass lepton identification requirements. The number of such tags found is scaled by the misidentification probability as a function of momentum. The estimated $\widetilde{M}_\nu^2$ distribution of tags in which the lepton candidate is a fake is shown in Figure 4.8. The areas of these distributions in the right-sign signal region give the number of tags where the lepton candidate is a fake. There are 460 ± 138 tags with fake muons and 140 ± 42 with fake electrons. The errors are due to a systematic uncertainty of $\pm 30\%$ on the fake probabilities[42]. These numbers indicate that a fraction

$$f^f = 5.6 \pm 1.3\% \tag{4.21}$$

of all random tags contain either a fake electron or a fake muon.

4.6 Spectra of Additional Leptons

The probability of finding an additional lepton in a random tag is effectively lower than that for a peak tag. This is because random tags are preferentially selected among events where the second B decays hadronically. The hadronization of the W from the second B is an additional source of pions with which to form background tags – a source not present when the second B decays semileptonically. This bias occurs only for background tags where the lepton and pion candidates originate from different B's. The bias does not occur for the portion of background tags where the

---

[7] One exception would be the process $\bar{B}^0 \rightarrow D^{*+}\pi^-, D^{*+} \rightarrow D^0\pi^+$ where the π^- fakes a μ^-. This contribution would tend to peak at $\widetilde{M}_\nu^2 = 0$.

uncorrelated pion is from the *same* B as the lepton candidate, nor does it occur for peak tags (which certainly have the pion coming from the same B as the tag lepton). The *effective efficiency* $\epsilon^{\rm eff}$ for finding an additional lepton in a random tag, relative to that for a peak tag, is evaluated via Monte Carlo for $\overline{B^0}\, B^0(\epsilon_u^{\rm eff})$, $\overline{B^0}\,\overline{B^0}(\epsilon_m^{\rm eff})$ and $B^-\, B^+(\epsilon_+^{\rm eff})$ events. The values for the three effective efficiencies are found to be

$$\epsilon_u^{\rm eff} = 0.625 \pm 0.035 \tag{4.22}$$

$$\epsilon_m^{\rm eff} = 0.908 \pm 0.090 \tag{4.23}$$

$$\epsilon_+^{\rm eff} = 0.649 \pm 0.033 \tag{4.24}$$

where the effective efficiency for peak tags is understood to be 1.0. These numbers are for background tags where the tag lepton is a primary lepton. The effective efficiency for secondary tag leptons is also evaluated, and found to be 1.0 ± 0.3 for charged and neutral events.

The electron spectrum is measured between 0.6 GeV/c and 2.5 GeV/c, and the muon spectrum between 1.5 GeV/c and 2.5 GeV/c. Figure 4.9 shows the raw spectrum for ON $\Upsilon(4S)$ data.

Four contributions must be subtracted from these raw spectra. Firstly, the OFF $\Upsilon(4S)$ data must be subtracted. Next, the spectrum of second lepton candidates which are actually misidentified hadrons must be removed. Thirdly, the contribution when the tag lepton is a misidentified hadron must be subtracted. Finally, a correction must be made for leptons (either tag lepton or second lepton) which is from a J/ψ or ψ'. Figure 4.10 shows the size of each of these contributions. Note the change in vertical scale from Figure 4.9.

The contribution to the second lepton spectra from fake second leptons is determined by first forming the spectrum of all tracks not identified as leptons in tagged

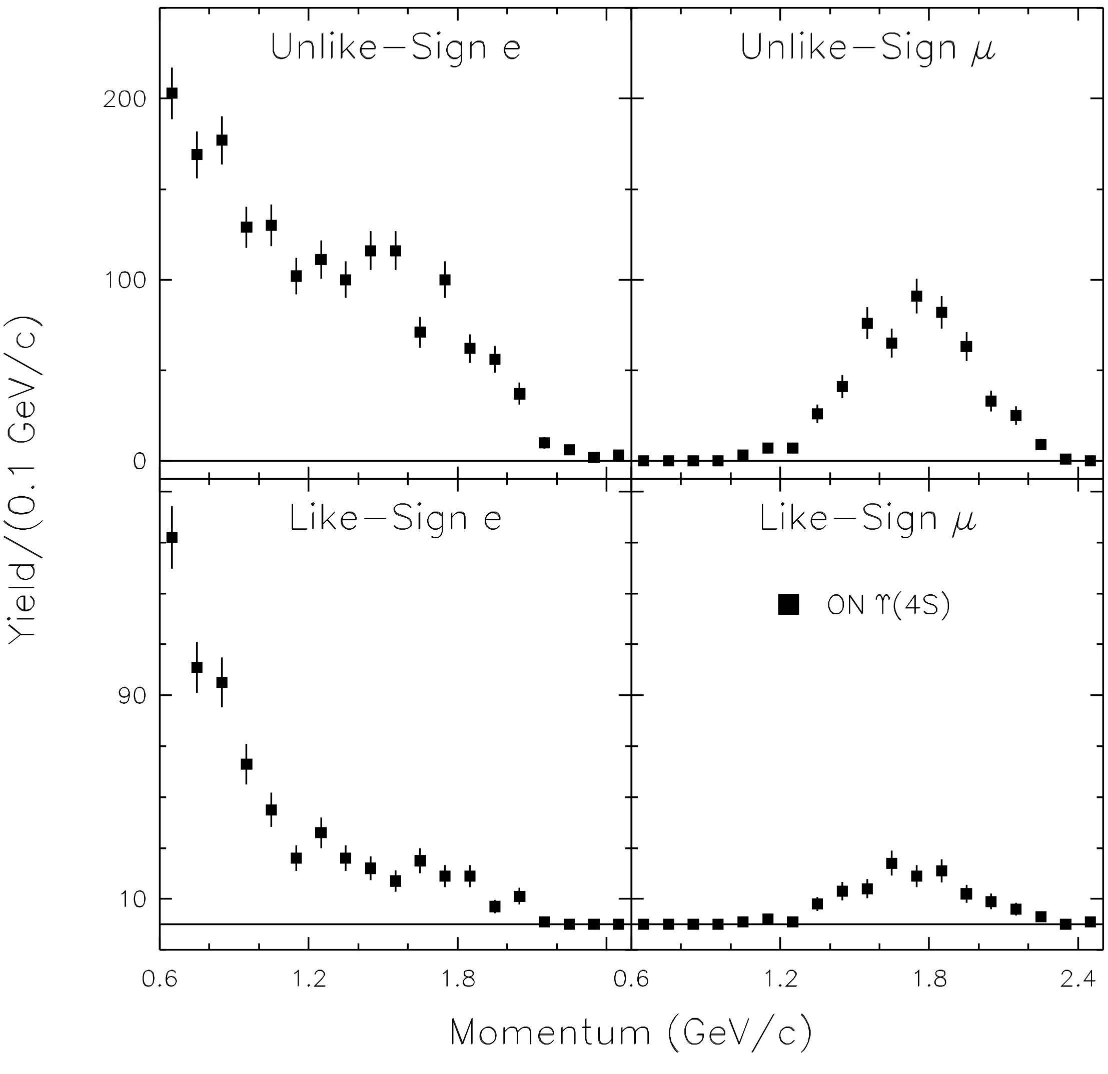

Figure 4.9: Raw spectra of additional leptons in tagged events in data. The spectra are sorted by type of additional lepton, and by charge relative to the tag lepton. The points represent the on-resonance data and have not been corrected for the continuum contributions.

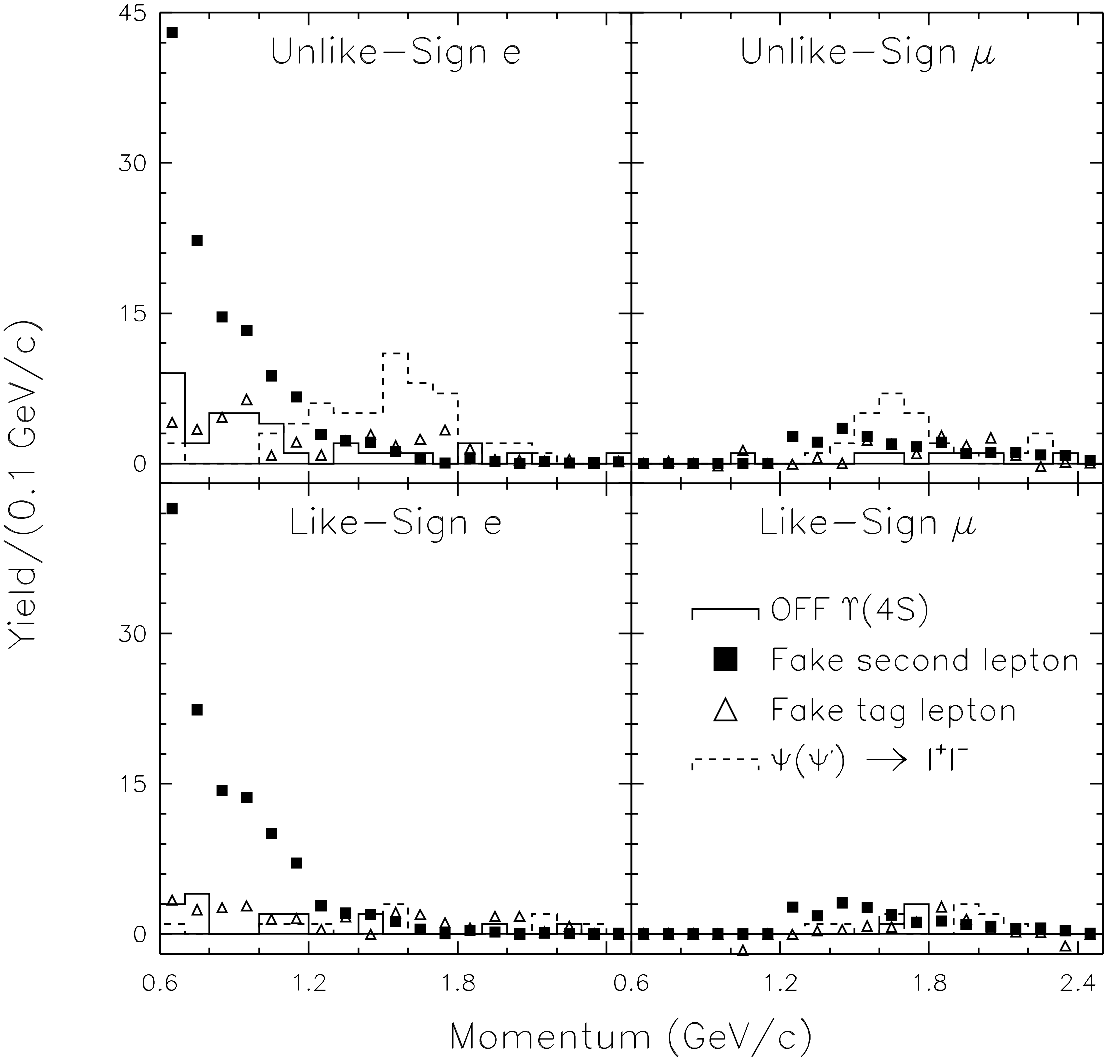

Figure 4.10: Four different contributions to subtract from the raw spectra. The solid curve is the off-resonance contribution, the solid squares represent the contribution from fake additional leptons, the open triangles represent the contribution to real additional leptons from fake tag leptons, and the dashed curve represents the Monte Carlo estimate for contributions from J/ψ decay.

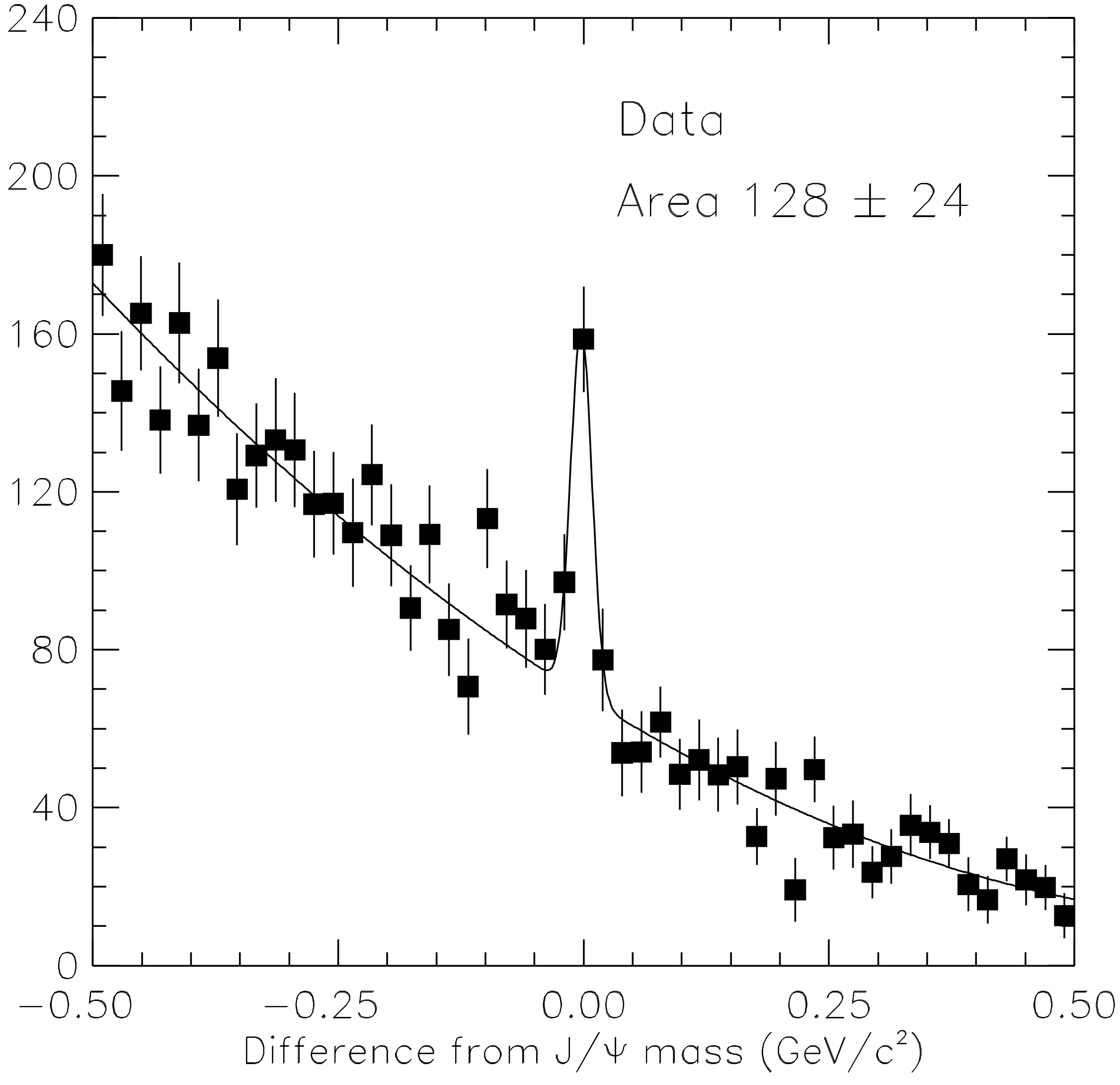

Figure 4.11: $J/\psi \rightarrow \mu^+\mu^-$ mass peak in tag signal region (Data).

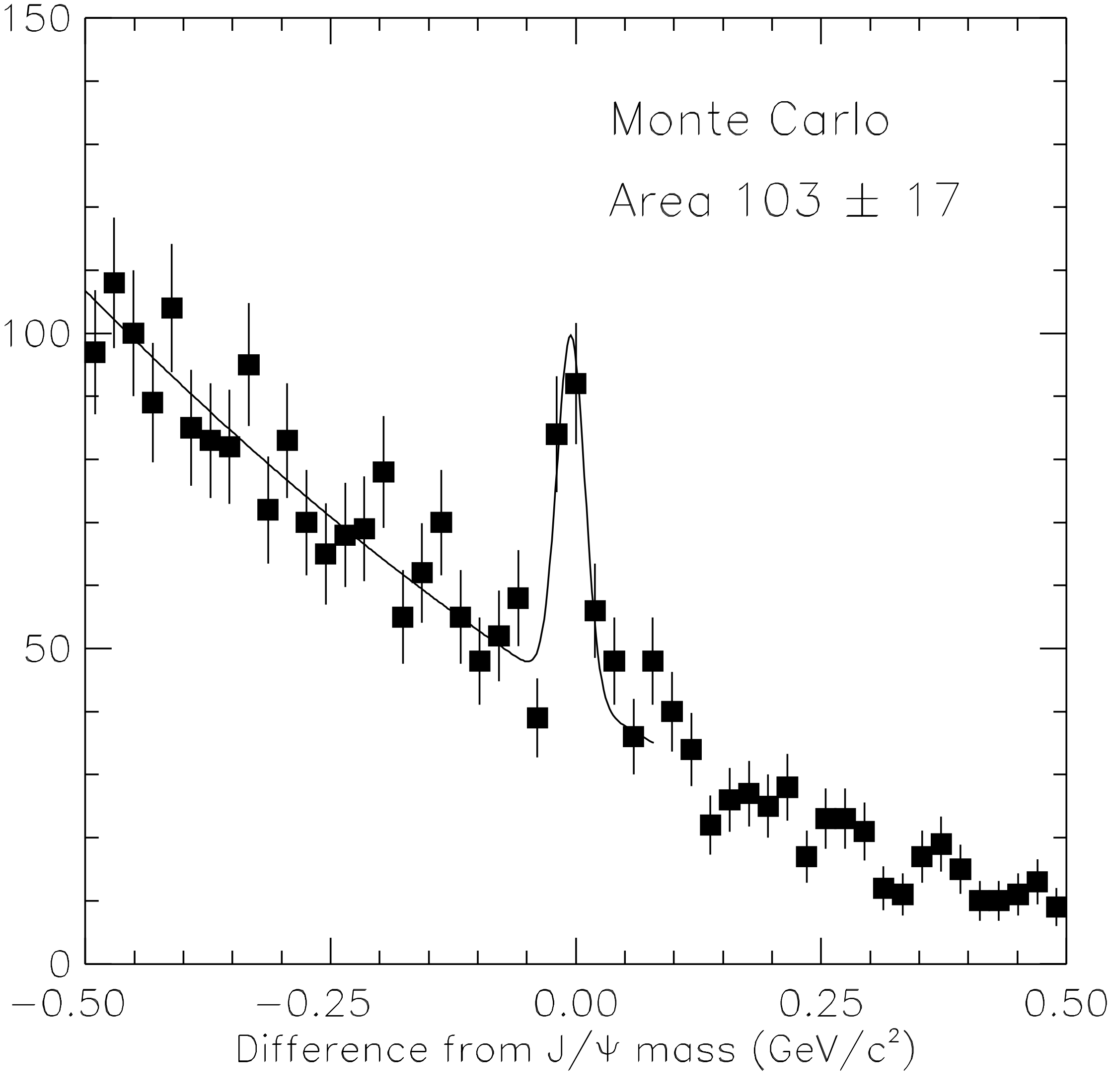

Figure 4.12: $J/\psi \rightarrow \mu^+\mu^-$ mass peak in tag signal region (Monte Carlo)

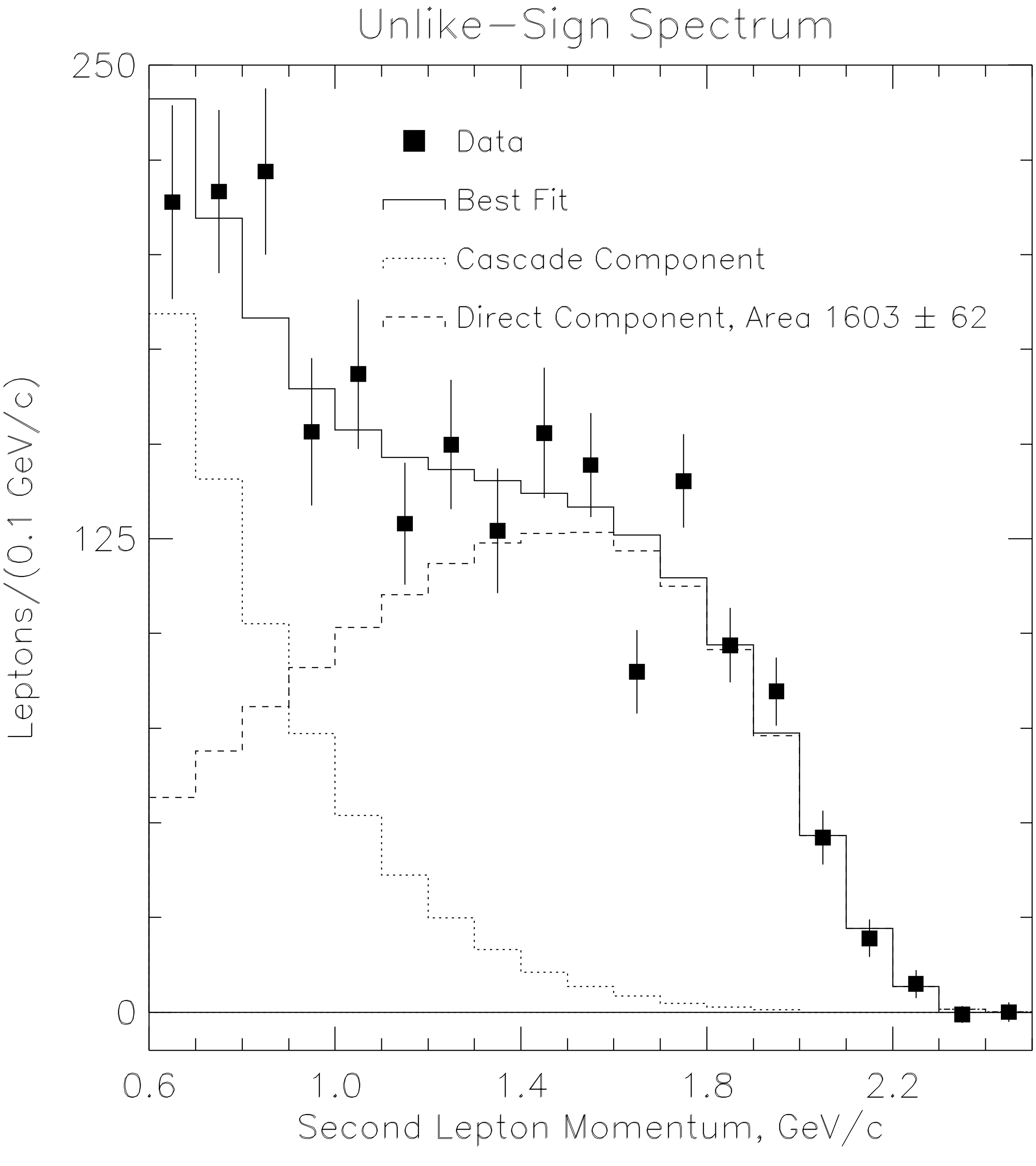

Figure 4.13: Fit to the unlike-sign additional lepton spectrum. The points are the data after all corrections, the dashed curve is a primary spectrum shape from the model of ISGW, the dotted curve is a secondary spectrum shape, and the solid curve is the best fit to the data. The error bars on the points are statistical only.

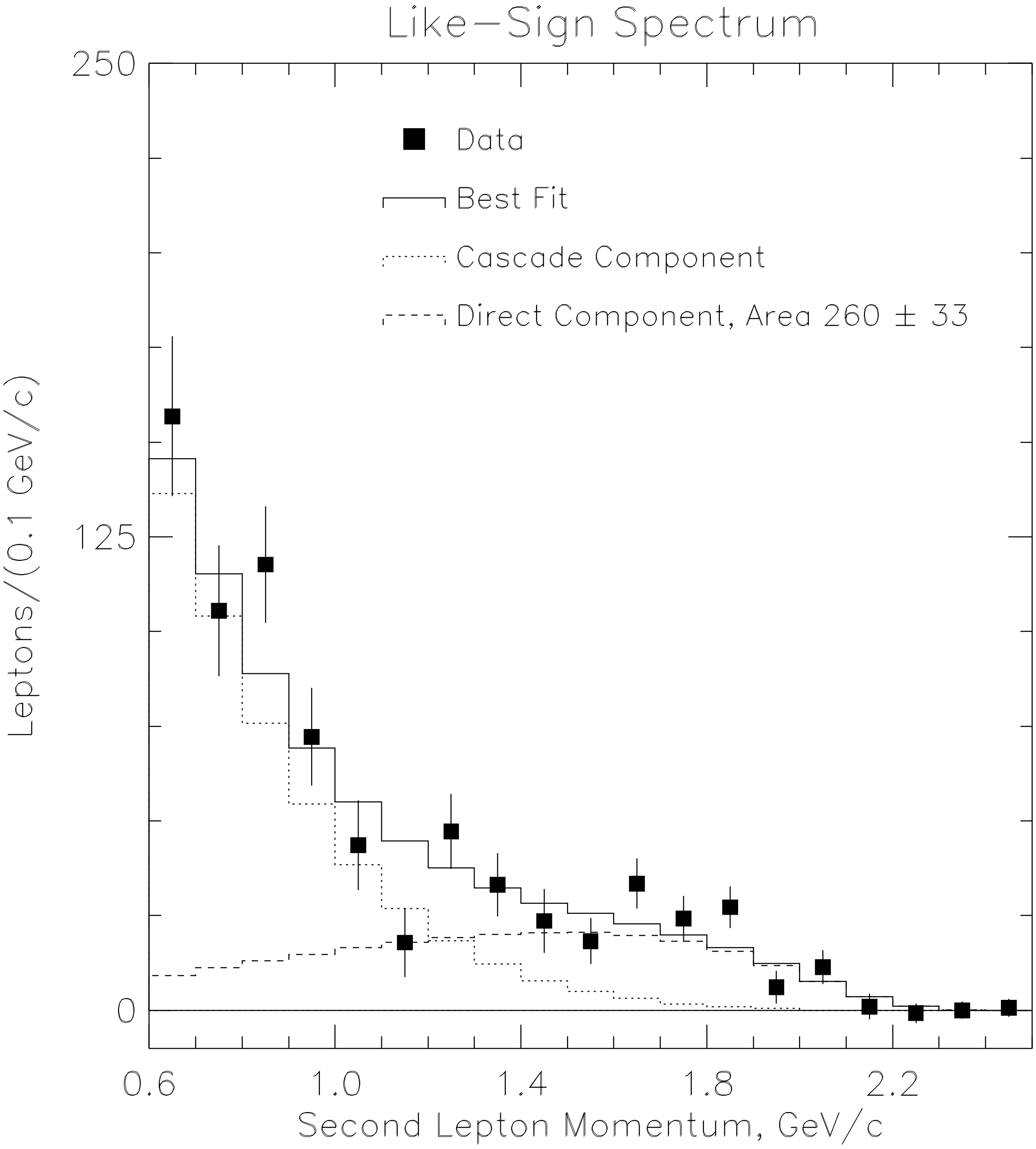

Figure 4.14: Fit to the like-sign additional lepton spectrum. The points are the data after all corrections, the dashed curve is a primary spectrum shape from the model of ISGW, the dotted curve is a secondary spectrum shape, and the solid curve is the best fit to the data. The error bars on the points are statistical only.

events, but which fall inside the allowed fiducial region for second leptons. These are assumed to be hadrons. A separate spectrum is recorded for hadrons of each relative sign to the tag lepton, like and unlike sign. Next, each momentum bin of the spectra is weighted by the electron fake rate for that momentum bin to determine the number of second electron candidates which are fakes. The spectra are also weighted by the muon fake rates to obtain the spectra of muon fakes.

The contribution to the second lepton spectra from tags containing a fake lepton is determined by repeating the entire analysis, replacing the tag lepton with tracks which fail the lepton identification requirements, and scaling the rates by the misidentification probability.

Contributions from the decay $J/\psi \rightarrow l^+l^-$ must be subtracted, where both or only one of the tag and additional lepton are from the J/ψ decay. An excess of unlike-sign events occurs when both the tag and the additional lepton are from a single J/ψ. When only one of the J/ψ leptons is used in the analysis, along with a lepton from some other source, either a like or unlike-sign lepton pair can result. To evaluate these contributions to the spectra, the analysis is performed on simulated events, and the like and unlike-sign spectra are recorded if *either* tag or additional lepton is from a J/ψ. The four uncorrected spectra are shown in Figure 4.10 for like-/unlike-sign, and for additional electrons/muons. The simulated event results must be scaled by a factor equal to the number of J/ψ's in data divided by the number in the simulated event sample. To determine this scale factor, a fit is made to the $J/\psi \rightarrow \mu^+\mu^-$ invariant mass peak in data and monte carlo for tags in the right-sign signal region. One of the muons is required to pass loose identification criteria, and no requirements were made on the other track. The muon rather than the electron mode is used because the size of the radiative tail of the invariant mass peak is smaller, and

	$\mu^{\pm}\pi^{\mp}$	$e^{\pm}\pi^{\mp}$
Tags, $\Upsilon(4S)$	11197	13029
Tags, continuum	804	736
Net, $B\overline{B}$	9499±122	11475±128
Random	4992±87±115	5749±92±277
Net peak	4507±150±115	5726±158±277

Table 4.2: Tags in data, with muons and electrons shown separately. Calculation of the random contribution is described in the text.

presumably less sensitive to the modeling of the tail in the simulated data. Muon identification is required on only one candidate, which minimizes the systematic error due to possible differences in muon identification efficiencies between the data and monte carlo The invariant mass peaks observed in data and monte carlo right-sign tags are shown in Figures 4.11 and 4.12.

After J/ψ, continuum and fake subtractions and corrections for detection efficiency have been completed, the weighted average of electron and muon spectra is calculated.

To determine the number of primary leptons the ISGW** model is used to fit the primary $b \to cl\nu$ spectrum and a semiempirical model for the secondary $c \to sl\nu$ spectrum. The fitted spectra are shown in Figures 4.13 and 4.14. The numbers of primary leptons are found to be $N_{-+} = 1603 \pm 62$ and $N_{++} = 260 \pm 33$, giving a ratio

$$M = N_{++}/N_{-+} = 0.162 \pm 0.022. \tag{4.25}$$

4.7 Evaluation of Mixing

Each row of Tables 4.4 and 4.5 represents one term in a sum either for N_{-+} or N_{++}. Collecting all of the terms explicitly, one finds the expressions for N_{-+} and

Parameter	Value
F^R	0.512 ± 0.019
f^{**}	0.14 ± 0.08
f^f	0.056 ± 0.013
f_c	0.026 ± 0.008
$\epsilon_+^{\rm tag}/\epsilon_u^{\rm tag}$	0.97 ± 0.03
$\epsilon_m^{\rm tag}/\epsilon_u^{\rm tag}$	1.18 ± 0.07
$\epsilon_u^{\rm eff}$	0.625 ± 0.035
$\epsilon_m^{\rm eff}$	0.908 ± 0.090
$\epsilon_+^{\rm eff}$	0.649 ± 0.033
N	$[1 + \alpha\frac{\epsilon_+^{\rm tag}}{\epsilon_u^{\rm tag}} + \chi_d(\frac{\epsilon_m^{\rm tag}}{\epsilon_u^{\rm tag}} - 1)]^{-1}$

Table 4.3: Summary of parameters used to extract χ_d from M

Tag Process	l_2 from	Tag Fraction (f_i)	Sign
$\overline{B^0} \to D^{*+}l^-\bar{\nu}$	B^0	$(1-F^R)(1-f^{**})(1-\chi_d)$	$-+$
	$\bar{B}^0$	$(1-F^R)(1-f^{**})\chi_d$	$--$
$\bar{B}^0 \to D^{*+}\pi^0 l^-\bar{\nu}$	B^0	$(1-F^R)\frac{f^{**}}{1+2\alpha}(1-\chi_d)$	$-+$
	$\bar{B}^0$	$(1-F^R)\frac{f^{**}}{1+2\alpha}\chi_d$	$--$
$B^- \to D^{*0}\pi^+ l^-\bar{\nu}$	B^+	$(1-F^R)\frac{2\alpha f^{**}}{1+2\alpha}$	$-+$

Table 4.4: Origins of tag-lepton pairs among tags in the peak. l_2 refers to the additional lepton from a primary B decay. f_i is the fraction of tags from the listed process including its dependence on the mixing parameter χ_d. α is defined $\alpha \equiv f_+ b_+ / f_0 b_0$.

Tag Process	l_2 from	Tag Fraction (f_i)	$\epsilon_i^{\rm eff}$	Sign
$\bar{B}^0 \to clX$	B^0	$NF^R(1-f^f)(1-f_c)\ (1-\chi_d)$	.625±.035	$-+$
	$\bar{B}^0$	$NF^R(1-f^f)(1-f_c)\frac{\epsilon_m^{\rm tag}}{\epsilon_u^{\rm tag}}\chi_d$	.908±.090	$--$
$B^- \to clX$	B^+	$NF^R(1-f^f)(1-f_c)\alpha\frac{\epsilon_+^{\rm tag}}{\epsilon_u^{\rm tag}}$	.649±.033	$-+$
$\bar{B}^0, B^- \to cX$	B^0, B^+	$F^R(1-f^f)f_c(1-\frac{\chi_d}{2})$	1.0±0.3	$++$
$c \to slY$	$\bar{B}^0$	$F^R(1-f^f)f_c\frac{\chi_d}{2}$	1.0±0.3	$+-$
	$\bar{B}^0, B^-$	$F^R(1-f^f)f_c$	1.0±0.3	$+-$
$B\bar{B} \to l_{\rm fake}X$		F^Rf^f		

Table 4.5: Origins of tag-lepton pairs among tags in the random background. l_2 refers to the additional lepton from a primary B decay. f_i is the fraction of tags from the listed process including its dependence on the mixing parameter χ_d and on the tagging efficiencies. $\epsilon_i^{\rm eff}$ is the effective efficiency for an additional primary lepton to have been produced (see text). α is defined $\alpha \equiv f_+b_+/f_0b_0$. N is a normalization factor equal to $[1+\alpha\frac{\epsilon_+^{\rm tag}}{\epsilon_u^{\rm tag}}+\chi_d(\frac{\epsilon_m^{\rm tag}}{\epsilon_u^{\rm tag}}-1)]^{-1}$.

N_{++} are given by

$$
\begin{aligned}
N_{-+} \propto &\quad (1-F^R)(1-f^{**})(1-\chi_d) \\
&+\ (1-F^R)\tfrac{f^{**}}{1+2\alpha}(1-\chi_d) \\
&+\ (1-F^R)\tfrac{2\alpha f^{**}}{1+2\alpha} \\
&+\ NF^R(1-f^f)(1-f_c)(1-\chi_d)\epsilon_u^{\rm eff} \\
&+\ NF^R(1-f^f)(1-f_c)\alpha\tfrac{\epsilon_+^{\rm tag}}{\epsilon_u^{\rm tag}}\epsilon_+^{\rm eff} \\
&+\ F^R(1-f^f)f_c\tfrac{\chi_d}{2} \\
&+\ F^R(1-f^f)f_c
\end{aligned}
\tag{4.26}
$$

$$
\begin{aligned}
N_{++} \propto &\quad (1-F^R)(1-f^{**})\chi_d \\
&+\ (1-F^R)\tfrac{f^{**}}{1+2\alpha}\chi_d \\
&+\ NF^R(1-f^f)(1-f_c)\tfrac{\epsilon_m^{\rm tag}}{\epsilon_u^{\rm tag}}\chi_d\epsilon_m^{\rm eff} \\
&+\ F^R(1-f^f)f_c(1-\tfrac{\chi_d}{2}).
\end{aligned}
\tag{4.27}
$$

The ratio $M = N_{++}/N_{-+}$ is a complicated function of χ_d and known parameters. One can solve for χ_d and find a linear relationship of the general form

$$\chi_d = \frac{aM-b}{cM+d} \tag{4.28}$$

where

$$a = (1 - F^R) + NF^R(1 - f^f)(1 - f_c)(\epsilon_u^{\text{eff}} + \frac{\epsilon_+^{\text{tag}}}{\epsilon_u^{\text{tag}}}\epsilon_+^{\text{eff}}) + F^R(1 - f^f)f_c \tag{4.29}$$

$$b = F^R(1 - f^f)f_c \tag{4.30}$$

$$c = (1 - F^R)(1 - 2f^{**}/3) + NF^R(1 - f^f)(1 - f_c)\epsilon_u^{\text{eff}} - F^R(1 - f^f)f_c/2 \tag{4.31}$$

$$d = (1 - F^R)(1 - 2f^{**}/3) + NF^R(1 - f^f)(1 - f_c)\frac{\epsilon_m^{\text{tag}}}{\epsilon_u^{\text{tag}}}\epsilon_m^{\text{eff}} - F^R(1 - f^f)f_c/2. \tag{4.32}$$

Using the values for the known parameters from Table 4.3 one finds

$$\chi_d = \frac{(0.796)M - 0.013}{(0.584)M + 0.690}. \tag{4.33}$$

For simplicity, $f_+/f_0 = b_+/b_0 = 1$ have been assumed, and these dependences have not been included in Equations 4.29 − 4.32. See appendix A for the full forms of the above equations.

A single event can contribute more than once to this measurement. Double lepton-pion tags are found in approximately 17% of the events containing a tag and an additional lepton. This occurs mainly because a pion candidate can curl around in the drift chamber and reconstruct as two separate tracks of the same charge and similar momenta. In this case, two tags may be found in the right-sign signal region. If no corrections are made, this will result in a slightly underestimated statistical error but no change of central value. To account for this redundancy the statistical error is increased by 10%:

$$M = 0.162 \pm 0.025 \tag{4.34}$$

and the value for χ_d is found to be

$$\chi_d = 0.149 \pm 0.023. \tag{4.35}$$

Model	N_{-+}	χ^2, 15 DOF	N_{++}	χ^2, 15 DOF	M
ISGW **	1603 ± 62	25.5	260 ± 33	27.3	0.162
ACM	1511 ± 57	26.3	252 ± 31	25.7	0.167
ISGW	1453 ± 55	31.0	247 ± 29	25.5	0.170
WSB	1389 ± 52	34.5	237 ± 28	25.6	0.171
Avg$\pm\sigma_{sys}$	1489 ± 91		249 ± 10		0.167 ± 0.004

Table 4.6: Results of fits to lepton spectra for four different theoretical models, described in text. The systematic error on M due to model dependence is taken to be the standard deviation of the four values.

4.8 Systematic Uncertainties

Spectrum shape

To estimate the systematic uncertainty due to uncertainty in the spectrum shape, the values of N_{-+} and N_{++} are fitted to lepton spectra given by four models of b and c semileptonic decay, by Isgur et al. (ISGW), Altarelli et al. (ACCMM), Wirbel et al. (WSB)[47], and the model of Isgur et al. in which the D^{**} fraction is increased from 11% to 32% (ISGW**). The results of these fits are shown in Table 4.6. All of these models include secondary charm spectra which give values of $f_{c+\bar{c}}$ around 2%, somewhat lower than the current estimate. Therefore these fits are used only to indicate the systematic uncertainty due to model dependence, which is estimated from the rms spread among the various models. The fractional deviation of M from the mean is seen to be much smaller than that of either N_{-+} or N_{++} alone. This is due to the fact that the same curve is used in the fits of the two spectra, so that adjustments of the fit to the shape are correlated.

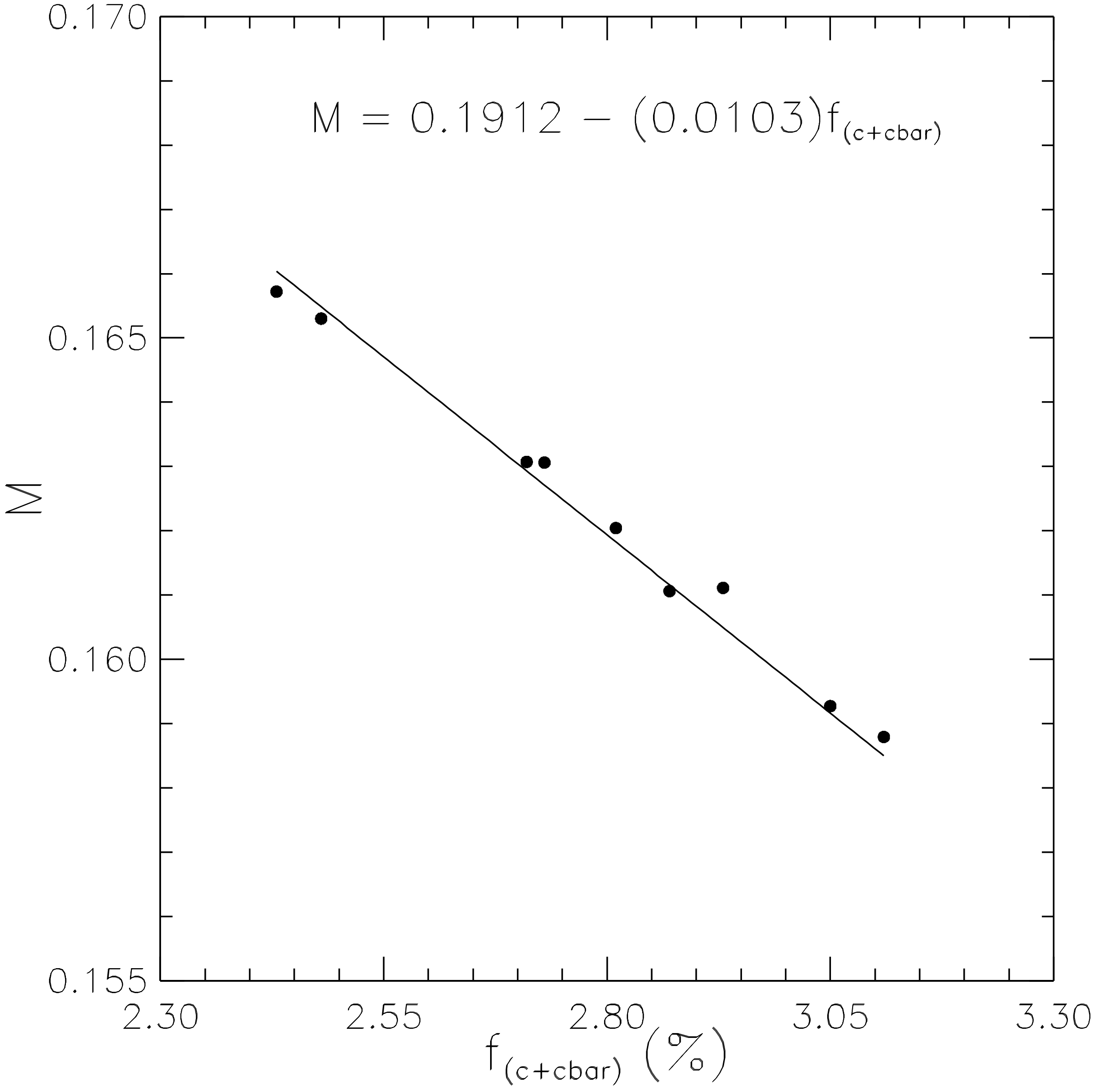

Figure 4.15: M versus $f_{c+\bar{c}}$

	$f_{c+\bar{c}}$	N_{-+}	χ^2, 15 dof	N_{++}	χ^2, 15 dof	M
Nominal	0.028	1603 ± 62	23.7	260 ± 33	22.3	0.162
Param #1 high	0.025	1613 ± 62	23.7	267 ± 33	20.9	0.165
Param #1 low	0.031	1593 ± 62	22.8	254 ± 33	22.8	0.159
Param #2 high	0.029	1598 ± 62	23.1	257 ± 33	22.5	0.161
Param #2 low	0.027	1606 ± 62	23.4	262 ± 33	21.6	0.163
Param #3 high	0.031	1591 ± 62	23.2	253 ± 33	23.3	0.159
Param #3 low	0.024	1615 ± 62	23.9	268 ± 33	21.2	0.166
Param #4 high	0.027	1606 ± 62	23.4	262 ± 33	21.7	0.163
Param #4 low	0.029	1599 ± 62	23.4	258 ± 33	22.4	0.161

Table 4.7: Variation of fits with secondary lepton spectrum shape. Each of four parameters defining the secondary curve is varies by $\pm 1\sigma$. The value of $f_{c+\bar{c}}$ is listed for each curve, along with the fit ratio M. To be conservative, this study was done using an electron fake rate of 0.7 times the nominal value, since the dependence of M on $f_{c+\bar{c}}$ was found to be strongest at low values for the electron fake rate.

$f_{c+\bar{c}}$

Uncertainty on the value of $f_{c+\bar{c}}$ affects the analysis in two ways. Firstly, adjustments must be made to the shape of the secondary lepton spectrum used to fit the unlike and like-sign second lepton spectra, affecting the value of M. Secondly, adjustments must be made for the fraction of the random background tags with secondary leptons from charm. These two effects must be treated in the appropriate correlated manner. In the discussion which follows, we examine the first issue, the dependence of M upon $f_{c+\bar{c}}$.

Four parameters used to define the secondary spectrum can each in turn be varied by the values of their uncertainty. This provides a set of nine secondary spectra, all with slightly different values of $f_{c+\bar{c}}$. These nine fits can be used to determine the dependence of the fit ratio M on the value of $f_{c+\bar{c}}$. Table 4.7 gives the fitting results for each of the nine different secondary spectrum shapes. A plot of $M(f_{c+\bar{c}})$ from Table 4.7 is shown in Figure 4.15. The dependence of M on $f_{c+\bar{c}}$ is found to be linear. This linear parameterization can be used to quantify the systematic uncertainty on M due to uncertainty on $f_{c+\bar{c}}$.

It is important to determine the slope of $M(f_{c+\bar{c}})$ correctly, or at least to not underestimate it, because this dependence results in the largest contribution to the systematic error in the final result. Therefore, it is important to elaborate upon a certain point. *The slope of the linear fit in Figure 4.15 depends on the value of the electron fake rate.* For the study shown in Table 4.7, a value 0.7 times the nominal electron fake rate was used, not the nominal value. To be conservative, this lower value was used, because the slope of M versus $f_{c+\bar{c}}$ was found to be larger at low values for the electron fake rate. This happens because the spectrum of fake electrons resembles that of the secondary leptons. If a small electron fake rate is used, then the fakes will be underestimated and the size of the secondary component of the spectrum will appear larger. As the absolute size of the secondary component gets larger, the details of its shape become more important. Therefore, the fit ratio M is more strongly dependent on the model used to fit the secondary component. Because this study was performed using a "worst-case" electron fake rate, the slope of the line and therefore the largest contribution to the systematic error is probably overestimated.

Other Uncertainties

The error in the number of random tags is taken to be the spread in the values obtained from two background fitting methods. The uncertainties in the relative tagging efficiencies and second lepton effective efficiencies of $\overline{B^0}B^0$, $\overline{B^0}\,\overline{B^0}$ and B^-B^+ events are taken to be twice the statistical error on the Monte Carlo. The uncertainty in the fraction of $D^*\pi l\bar{\nu}$ decays in the sample is taken from Equation 4.17 to be $0.08/0.14 = 57\%$. The uncertainty on both $f_{c+\bar{c}}$ and on the lepton fake rates are taken to be 30%.

Correlations

The determination of χ_d involves many correlated inputs which must be accounted for in computing the uncertainties. Given these correlations, it would be a formidable task to solve for the errors analytically. Instead, the errors are obtained numerically. The central value of χ_d can be calculated given all the central values of the input parameters. The effects of the correlations are automatically taken into account by allowing the program to recalculate a new central value for χ_d as any or all of the input parameters are varied with a normal distribution within their limits. The error is taken to be the standard deviation of the resulting ensemble of χ_d values. The result is checked against analytically calculated errors in several limiting cases.

Variations in $f_{c+\bar{c}}$ and fake probabilities affect the tags and the spectra in a correlated way which is taken into account. The resulting dependence of χ_d on $f_{c+\bar{c}}$ is shown in Figure 4.16. The model of semileptonic B decay, the $D^*\pi l\bar{\nu}$ fraction and $f_{c+\bar{c}}$ are weakly correlated, and this is allowed for in the overall systematic error.

These sources, their uncertainties and the resulting errors on the measurement of χ_d are given in Table 4.8. Their net contribution to the systematic error is ± 0.019, excluding the uncertainty due to Λ, which will be treated separately.

Λ dependence

The result has a weak dependence on the assumed value of Λ. It also has a separate dependence on b_+/b_0 because of the pure $\overline{B^0}$ sample in the peak. The error is calculated by assuming that $f_+/f_0 = 1.0 \pm 0.05$ and $b_+/b_0 = 1.0 \pm 0.14$, which corresponds to a 14% uncertainty in Λ. The resulting uncertainty in χ_d is ± 0.010 and is reported separately. The dependence on Λ is also calculated assuming that its uncertainty is dominated by that of either b_+/b_0 or f_+/f_0 alone (Figure 4.17). A reasonable parameterization of the Λ dependence is found to be

$$\chi_d \simeq 0.149/(2(1-\Lambda))^{0.4}. \tag{4.36}$$

Discussion

The major systematic uncertainties affecting previous measurements of mixing using dileptons have a significantly reduced influence in this method. There are a number of reasons for this. First, the tag sample consists of two parts, peak and random background. The peak, which comprises approximately half of the tags, has a high purity of $\overline{B^0}$'s and therefore nearly no dependence on the differences between f_+ and f_0, or b_+ and b_0. The peak also contains no leptons from secondary decays of charm or fake leptons, which reduces the natural occurrence of false mixing events due to an incorrect flavor tag. Second, although the background tags are dependent on these effects, they contribute less to the additional lepton tag due to their lower effective efficiency. The result of this is that the purity of the lepton sample in $\overline{B^0}$ is ~80%. The variability of this purity under the uncertainties of production and semileptonic decay of charged and neutral B's is small. Therefore, the final result has a relatively small dependence on Λ, which was the original goal.

Source	σ_{sys}/value	$\delta\chi_d$
$f_{c+\bar{c}}$	0.30	0.011
$D^*\pi l\bar{\nu}$ fraction	0.57	0.007
M, Models	0.02	0.003
$\epsilon_m^{\mathrm{tag}}/\epsilon_u^{\mathrm{tag}}$	0.06	0.003
$\epsilon_+^{\mathrm{tag}}/\epsilon_u^{\mathrm{tag}}$	0.03	0.001
$\epsilon_u^{\mathrm{eff}}$, primary leptons, $\overline{B^0}\,B^0$	0.12	0.002
$\epsilon_m^{\mathrm{eff}}$, primary leptons, $\overline{B^0}\,\overline{B^0}$	0.20	0.010
$\epsilon_+^{\mathrm{eff}}$, primary leptons, $B^-\,B^+$	0.10	0.004
ϵ^{eff}, secondary leptons	0.30	0.003
Fakes	0.30	0.005
Fraction of randoms in tag	0.04	<0.001
Overall		0.019
f_+/f_0	0.05	0.002
b_+/b_0	0.14	0.010

Table 4.8: Sources of systematic errors and the uncertainty introduced by each into the measurement of χ_d.

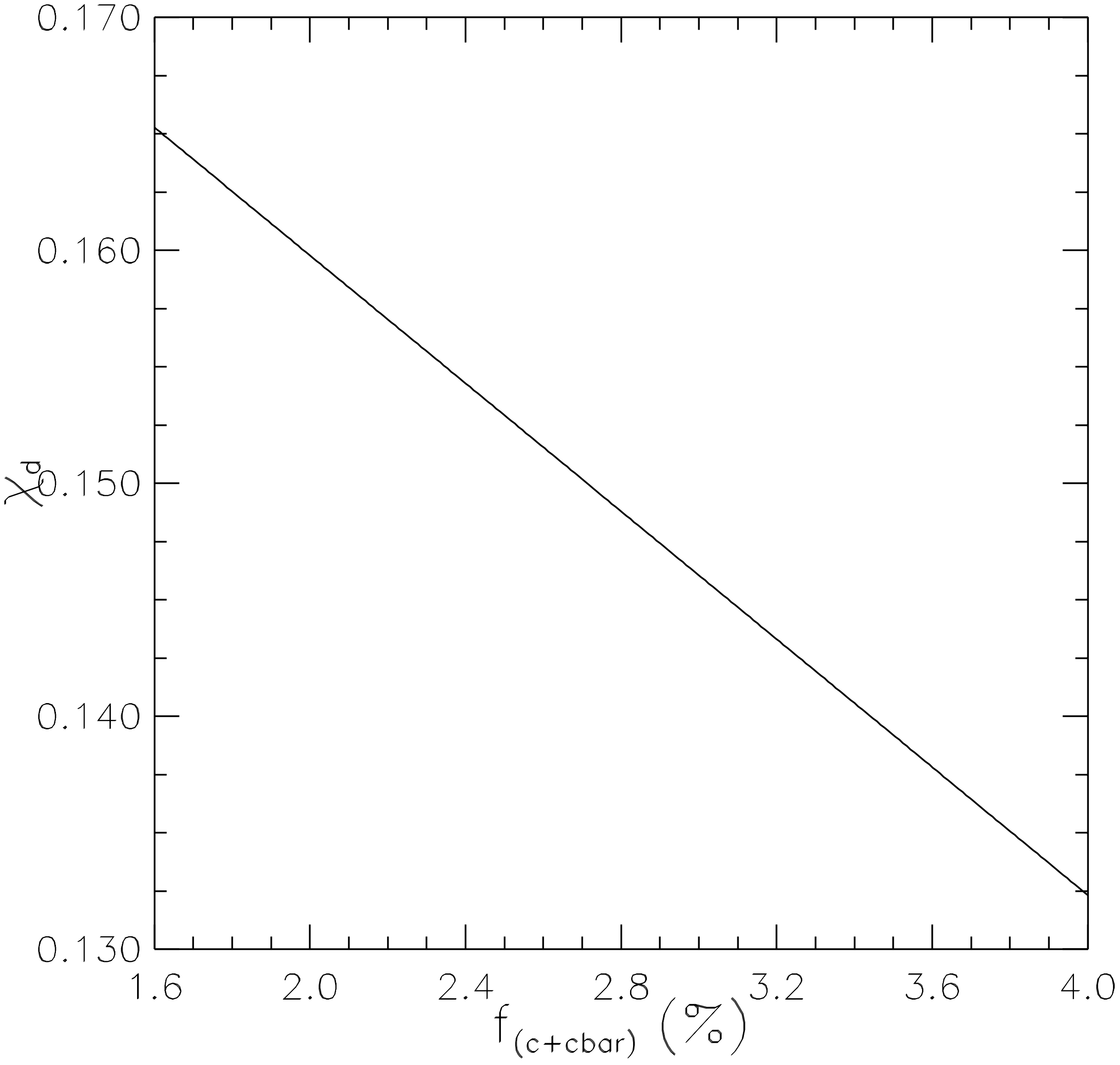

Figure 4.16: Central value of χ_d as a function of $f_{c+\bar{c}}$

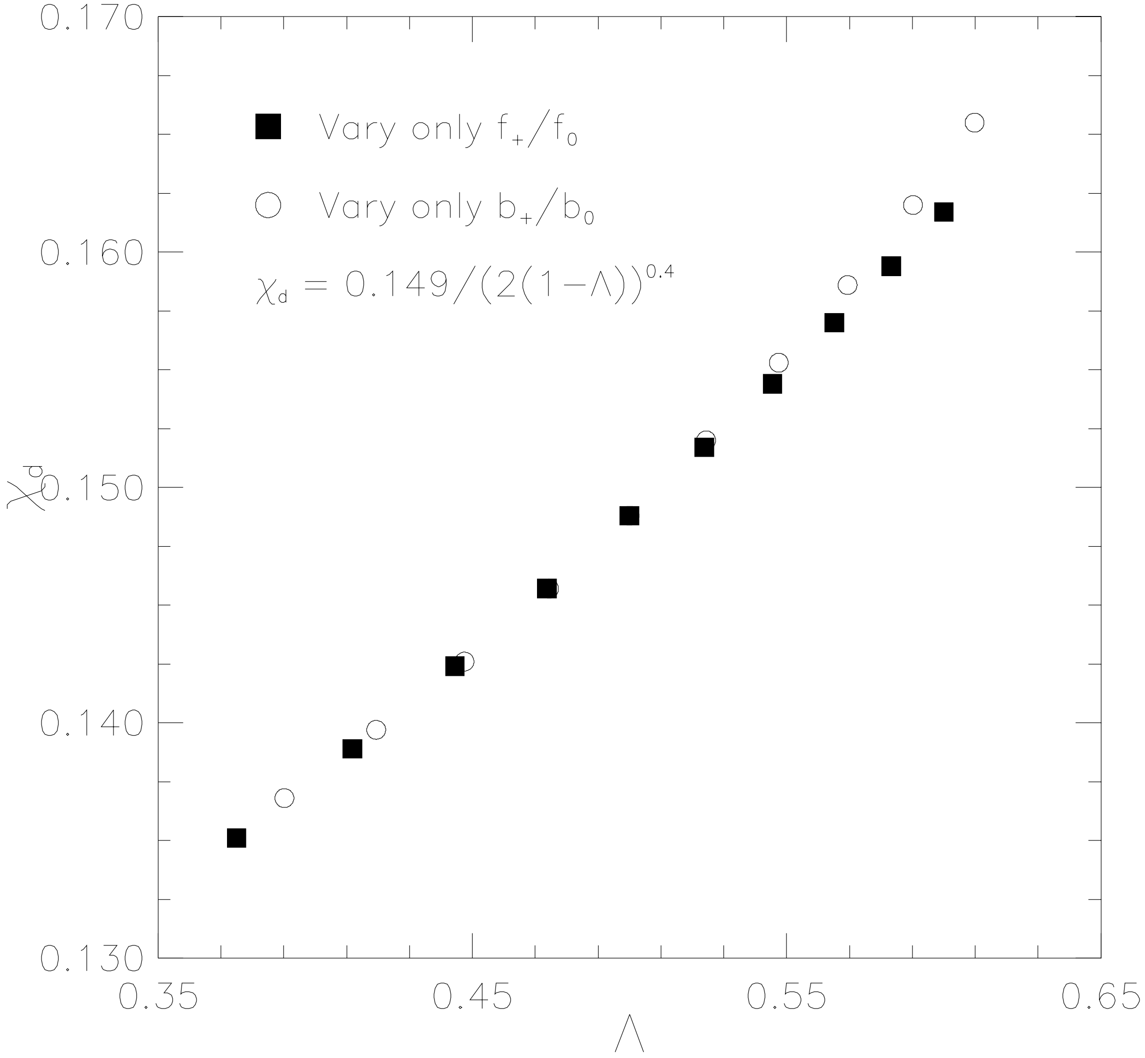

Figure 4.17: Central value of χ_d as a function of Λ

4.9 Result

The result is then

$$\chi_d = 0.149 \pm 0.023 \pm 0.019 \pm 0.010, \qquad \text{This thesis} \tag{4.37}$$

where the error associated with Λ is shown last. This can be compared with with mixing result obtained by other collaborators using the dilepton method with the same dataset

$$\chi_d = 0.157 \pm 0.016 \pm 0.018^{+0.028}_{-0.021} \qquad \text{Dileptons} \tag{4.38}$$

Note the substantially smaller systematic error due to Λ uncertainty on the tagged measurement. The two measurements were published together in September 1993 in reference [48]. At that time, the tagged measurement had the smaller combined uncertainty and was the world's most precise measurement of χ_d.

The ratio x_d is found to be

$$x_d \equiv \frac{\Delta M}{\Gamma} = 0.65 \pm 0.10. \tag{4.39}$$

where the error on x_d is determined from the quadratic sum of all three errors on χ_d.

The neutral B lifetime has been measured by experiments at higher energy experiments to be $\tau_0 = 1.621 \pm 0.067$ ps[24]. This yields a mass difference

$$\Delta M = (0.40 \pm 0.06) \times 10^{12}\ \hbar \mathrm{s}^{-1} \tag{4.40}$$

which is consistent with values obtained by experiments at LEP which observe the time-dependent oscillation frequency directly[49].

The top quark has recently been discovered by the CDF and D0 collaborations at Fermilab. We use the CDF result $m_t = 176 \pm 8 \pm 10$ GeV[50]. One can then use the measured value of x_d and these other measurements to arrive at a value of $|V_{td}|$ as a function of f_B, shown in Figure 4.18. As the figure shows a precise determination of $|V_{td}|$ is limited by knowledge of the decay constant f_B. However for a wide range of f_B values, the CKM matrix element appears to satisfy the following bounds

$$0.005 < |V_{td}| < 0.015. \tag{4.41}$$

This measurement provides a constraint on the location of the unitarity triangle's vertex within the $\rho - \eta$ plane. A measurement of $|V_{td}|$ results in an allowed region of annular shape centered at the point (1,0). Measurement of the CKM-suppressed rate $b \rightarrow u\ell\nu$ relative to the dominant mode $b \rightarrow c\ell\nu$ provides an additional constraint, a semicircular allowed region about the point (0,0). We take the result[51]

$$\frac{|V_{ub}|}{|V_{cb}|} = 0.08 \pm 0.02. \tag{4.42}$$

Additional information can be obtained from the measurement of the CP asymmetry parameter ϵ in neutral kaon decays, defined via

$$|K_L^0 >= [(1+\epsilon)|K^0 > -(1-\epsilon)|\overline{K^0} >]/[2(1+|\epsilon|^2)]^{1/2} \tag{4.43}$$

$$|K_S^0 >= [(1+\epsilon)|K^0 > +(1-\epsilon)|\overline{K^0} >]/[2(1+|\epsilon|^2)]^{1/2}. \tag{4.44}$$

and measured to be $|\epsilon| = (2.26 \pm 0.02) \times 10^{-3}$ [3]. In terms of standard model parameters, the expression for $|\epsilon|$ is

$$|\epsilon| = 4.3A^2B_K\eta[\eta_3S(x_c,x_t) - \eta 1F(x_c) + \eta^2A^2\lambda^4(1-\rho)F(x_t)] \tag{4.45}$$

where A, λ, ρ and η are the four CKM parameters, η_1, η_2 and η_3 are QCD correction factors, $x_i \equiv m_i^2/M_W^2$, $F(x)$ is the function of Equation 2.16, and

$$S(x,y) = xy\left(\left[\frac{1}{4} + \frac{3}{2(1-y)} - \frac{3}{4(1-y)^2}\right]\frac{\ln y}{y-x} + (y \leftrightarrow x) - \frac{3}{4(1-x)(1-y)}\right). \tag{4.46}$$

The allowed region from this measurement is a curving band across the $\rho - \eta$ plane.

Figure 4.19 shows the $\pm 1\sigma$ contours for each of the three measurements. For the mixing measurement, we have assumed a top quark mass of 176 GeV/c, $\eta_{\mathrm{QCD}} = 0.55$, and $\sqrt{B} f_B = 130$ MeV (top plot), 180 MeV (middle plot), and 230 MeV (bottom plot).

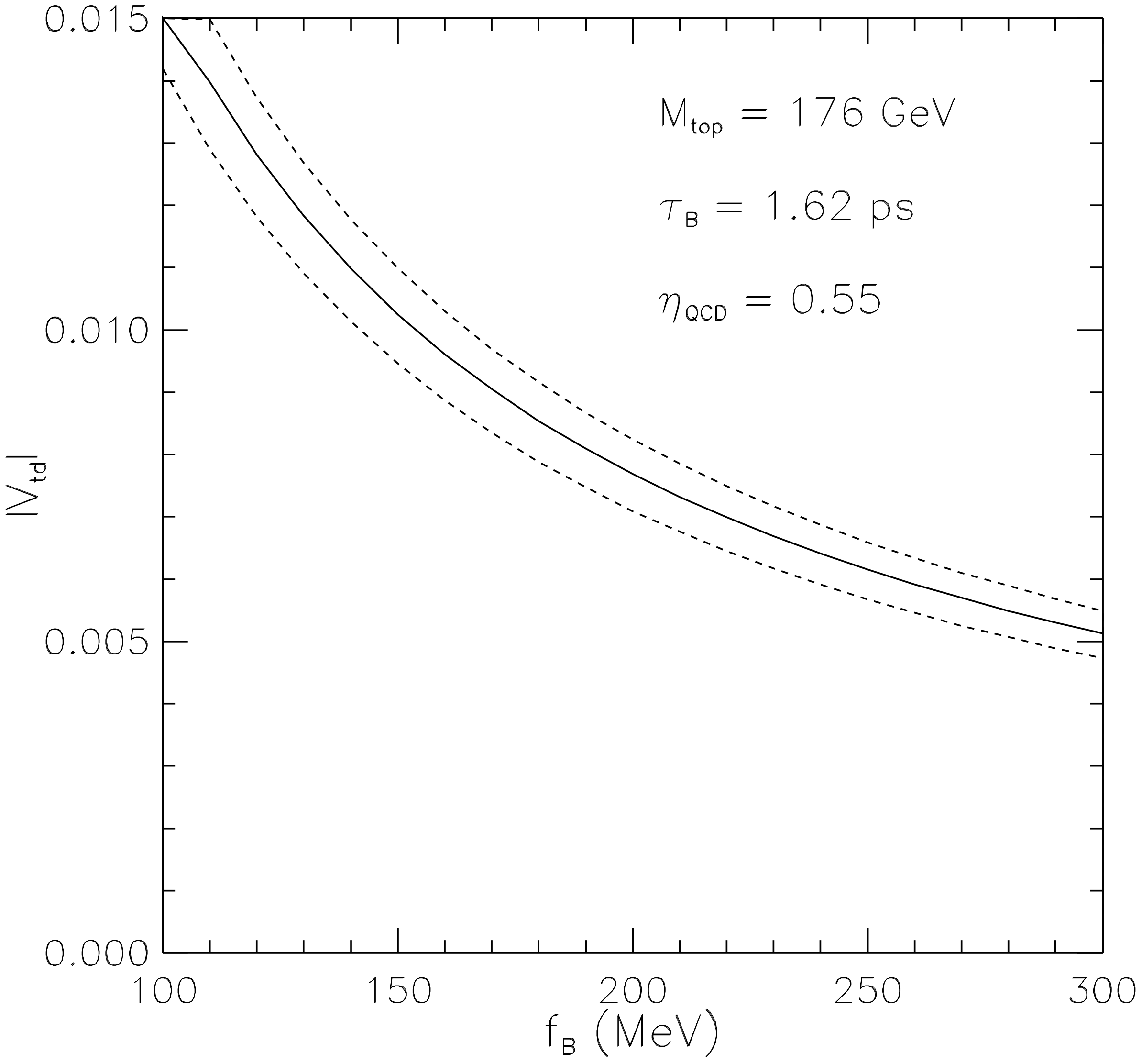

Figure 4.18: $|V_{td}|$ as a function of f_B. The $\pm 1\sigma$ error bands are due to uncertainty on χ_d only.

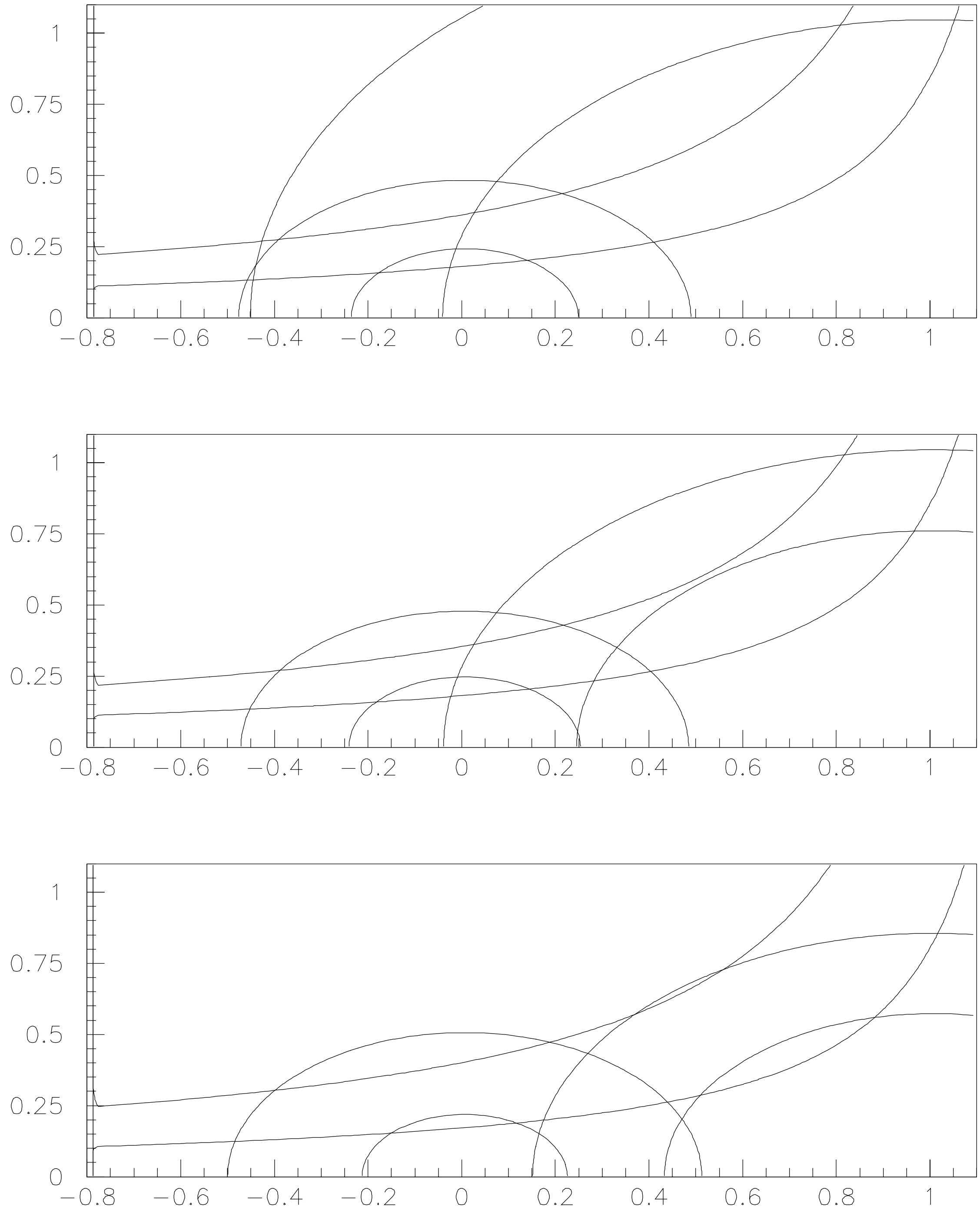

Figure 4.19: $\rho - \eta$ constraints, for $f_B = 130$ MeV (top), 180 MeV (middle), and 230 MeV (bottom). Also shown are the contours obtained from charmless semileptonic B decay and from $|\epsilon|$ in CP-violating kaon decays.

Chapter 5

Semileptonic Branching Fraction

5.1 Introduction

Despite more than ten years of experimental and theoretical work, experimental measurements of the semileptonic branching fraction of B mesons have been consistently and significantly lower than theoretical predictions[52]. The measurements have been made in several ways, most precisely as an average over B^- and $\overline{B^0}$ mesons [53, 54, 42] from the $\Upsilon(4S)$ resonance and with very limited statistics for neutral B's[53].

CLEO has measured the B semileptonic branching fraction, averaging over charged and neutral B's using two methods. The first measurement examines the energy spectrum of leptons at the Υ(4S). Figure 5.1 shows the spectrum for both muons and electrons. The spectrum is composed of two parts. The higher energy leptons are from the desired primary decays of the type $\overline{B} \to DX\ell\nu$. The lower energy leptons are from the secondary semileptonic decays of charm mesons, $D \to \overline{K}X\ell\nu$ for example. One must therefore fit the spectrum to a sum of these two components to arrive at a normalization for the primary area and thus a value for the semileptonic branching fraction. Using the model of ISGW for the primary spectrum, an average B branching fraction of $(10.96 \pm 0.07 \pm 0.22)\%$ is obtained. For this fit, the D^{**} fraction of the primary spectrum is allowed to be a free parameter, the best fit obtained with $(23 \pm 1)\%$. Fitting with the ACCMM model (not shown) a branching fraction of $(10.56 \pm 0.04 \pm 0.22)\%$ is found for $p_f = 265 \pm 25$ MeV/c and $m_c = 1670 \mp 25$ MeV/c^2. The difference between these two central values clearly indicates that model dependence is the limiting uncertainty on the precision of this measurement.

The second measurement determines the average B semileptonic branching fraction with little dependence on model. One demands that the event contain a high momentum lepton $p > 1.4$ GeV/c which tags the flavor of the first B in the event. Next charge and angular correlations are exploited to examine the spectrum of any primary electrons from the remaining B in the event. Figure 5.2 shows the spectrum of primary and secondary electrons from the B opposite the tag. The overlaid curve shows the agreement with the shape expected from the ISGW** model. The average B branching fraction[1] obtained using lepton tags is $(10.46 \pm 0.17 \pm 0.43)\%$.

5.2 Motivation for $\overline{B^0}$ Tagging

It is clear that the measured average B semileptonic branching fraction is less than the theoretical predictions. The natural next step is to examine the separate B^- and $\overline{B^0}$ semileptonic branching fractions. This motivates a tagged measurement

---

[1] The quantity measured is actually a more complicated weighted average $(f_+ b_+^2 + f_0 b_0^2)/(f_+ b_+ + f_0 b_0)$.

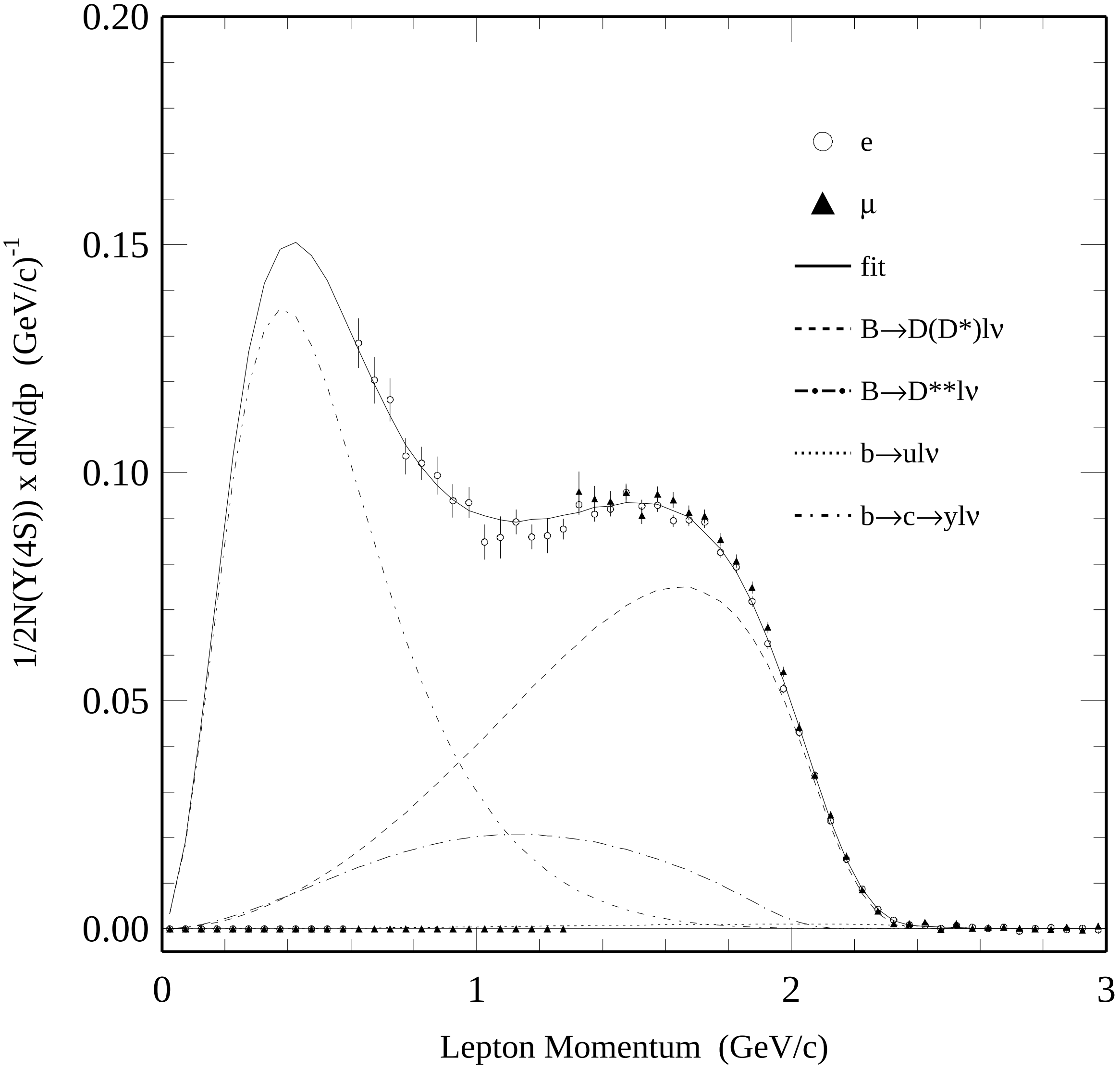

Figure 5.1: Fit to the $\Upsilon(4S)$ single lepton spectrum, using the model of ISGW with a floating D^{**} component. Open circles are the electron spectrum, close triangles are the muon spectrum. The data and theoretical functions have been corrected to account for effects of radiation and bremsstrahlung.

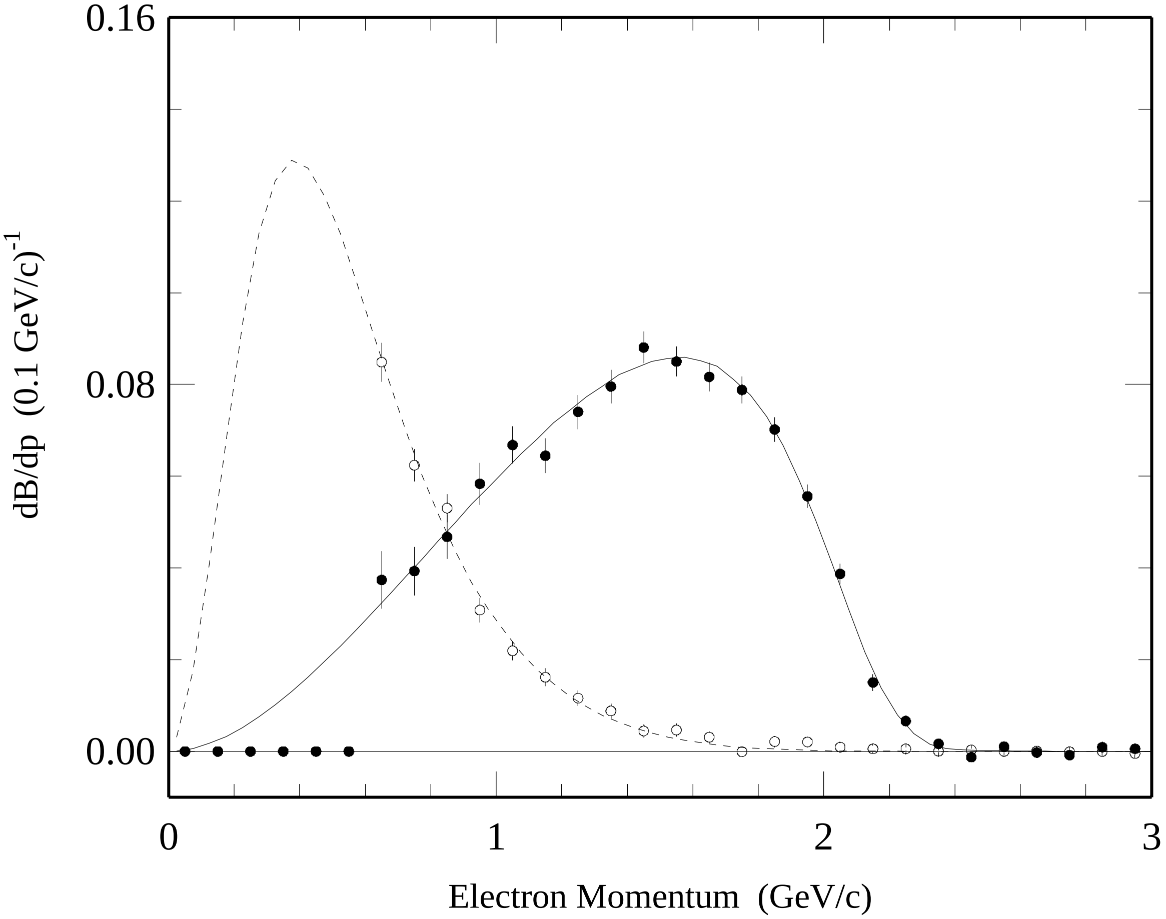

Figure 5.2: The $\Upsilon(4S)$ primary and secondary electron spectra using lepton tags. Overlaid are the curves showing the expected shape for the ISGW** model. The data and theoretical functions have been corrected to account for effects of radiation and bremsstrahlung.

where one first counts the number of B's reconstructed in some tag mode, then counts the fraction for which the remaining B decays semileptonically. This method has the additional advantage that by counting the number of B mesons in the event sample directly, one relies neither on assumptions about non-$B\overline{B}$ decays, nor on the ratio f_+/f_0.

The focus of this chapter is a measurement of the $\overline{B^0}$ semileptonic branching fraction, b_0, using partially reconstructed $\overline{B^0} \to D^{*+}\ell^-\overline{\nu}$ tags. For completeness, also reported here are other results of similar tagged measurements of b_+ and of b_0 using the same data. Combining these different measurements, value of the ratio b_+/b_0 is extracted. Assuming equality of semileptonic partial widths, this is an indirect measurement of the ratio of lifetimes.

5.3 Analysis Overview

The procedure of this analysis is somewhat simpler than that of the mixing measurement. The $\widetilde{M}_\nu^2$ distribution formed from right-sign lepton and pion pairs is fitted to determine the number of tags in the signal N_B. This is the number of events of the type

$$\overline{B^0} \to D^{*+}\ell^-\overline{\nu}, D^{*+} \to D^0\pi^+ \qquad\qquad B^0(\overline{B^0}) \to \text{Anything}.$$

Next, two other $\widetilde{M}_\nu^2$ distribution are plotted. These are the subsets of the initial events for which there is an additional fast electron (muon) present. The presence of such an additional fast lepton is a signature of the semileptonic decay of the remaining neutral B meson. Leptons of either sign are accepted to account for the possibility of $\overline{B^0} - B^0$ mixing. The $\widetilde{M}_\nu^2$ signal size is again determined. The events being counted are those of the type

$$\overline{B^0} \to D^{*+}\ell^-\overline{\nu}, D^{*+} \to D^0\pi^+ \qquad\qquad \overline{B^0}(\overline{B^0}) \to X\ell\nu.$$

Several corrections must be applied to the number of tags observed to contain leptons. Since leptons of both signs are accepted, secondary leptons from charmed meson decay, which have an approximate kinematic limit of 1.4 GeV/c, can contaminate the primary lepton sample. Another source of background is fake leptons, hadrons which pass lepton identification criteria. After background subtractions and efficiency corrections, the spectrum is extrapolated to the unobserved lower momentum region to obtain N_ℓ. A weighted average of the electron and muon results for N_ℓ is taken. The neutral B semileptonic branching fraction is given by

$$\mathrm{Br}(\overline{B^0} \to X\ell^-\overline{\nu}) = \frac{N_\ell}{N_B.} \tag{5.1}$$

In this analysis, if multiple tag combinations are possible in a single event, all are accepted. No attempt is made to select a single candidate. The reason for doing this is to avoid introducing a bias for which a correction would have to be later applied. This subtle phenomenon will now be discussed here firstly because it justifies the method, and secondly because it affects other similar measurements which rely on candidate selection criteria, as will be discussed in Section 5.9.

If one tag is chosen per event, then there is some chance of discarding a correct combination of a lepton and a pion in favor of a background combination. This is effectively an inefficiency for reconstructing tags, much like any other criterion imposed for defining a good tag. The problem arises when this tagging inefficiency may be different for numerator and denominator, resulting in a bias. This is expected to happen. The probability to form an additional background combination is a function of the environment in which a correct tag combination is embedded. For example, given that the first B in the event decays to the tag signal mode, when the opposite

B decays generically, there are generally more tracks in the event than when the opposite B decays semileptonically. With more tracks, it is more likely that a random combination will be formed, increasing the chances of discarding the correct combination from the first B. The correct simulation of this effect depends on accurate knowledge about backgrounds. This bias would result in an anomalously large value for the branching fraction. It is for this reason that we explicitly do not select one tag combination per event, eliminating the possibility for this kind of bias, and the need to correct for it.

5.4 Data and Selection Criteria

The data used in this analysis consist of integrated luminosities of 1.35 fb^{-1} on the $\Upsilon(4S)$ resonance and 0.64 fb^{-1} taken on the continuum, the `4S1` through `4S5` datasets. This is a larger data sample than was used for the mixing measurement.

All events are required to have `KLASGL` $= 10$, but no `R2GL` requirements are made. The pion and tag lepton momenta P_π and P_ℓ are required to satisfy $P_\pi < 0.19$ GeV/c and $1.8 < P_\ell < 2.4$ GeV/c. Pion candidates are additionally required to have specific ionization within two standard deviations of the pion hypothesis.

The relatively high momentum cut of 1.8 GeV/c on the lepton is chosen to reduce contributions from the B^- decay to $D^{**0}\ell\nu$ ($D^{**0} \to D^{*+}\pi^-$), which is believed to be small but is otherwise difficult to separate kinematically from the signal mode in the $\widetilde{M}_\nu^2$ distribution. Due to high reconstruction efficiency, the tag sample is large despite the stringency of the requirement on lepton momentum. Figure 5.3 shows the lepton momentum spectrum from $\overline{B} \to D^*\ell^-\bar{\nu}$ and $\overline{B} \to D^{**}\ell^-\bar{\nu}$ decays, with relative normalizations of .545/.210 respectively. Table 5.2 shows the fraction of the

Tag Lepton	$1.8 < p_\ell < 2.5$ GeV/c
	$\lvert\mathtt{DBCD}\rvert < 5$ mm
(electrons)	$\mathtt{R2ELEC} > 3$
(muons)	$\mathtt{MUQUAL} = 0$
	$\mathtt{DPTHMU} > 5$
Tag Pion	$p_\pi < 0.19$ GeV/c
	$\mathtt{KINCD} = 0$
	$\lvert\mathtt{SGPIDI}\rvert < 2$
	$\mathtt{IQALDI} = 1$ or -2
Second lepton	$1.4 < p_\ell < 2.5$ GeV/c
	$\lvert\mathtt{DBCD}\rvert < 5$ mm
	$\cos\theta_{\ell\ell} < 0.99$
(electrons)	$\mathtt{R2ELEC} > 3$
	$\lvert\mathtt{CZCD}\rvert < 0.707$
(muons)	$\mathtt{MUQUAL} = 0$
	$\mathtt{DPTHMU} > 5$
	$\lvert\mathtt{CZCD}\rvert < 0.707$

Table 5.1: Selection criteria for tags

p_ℓ min. (GeV/c)	D^* Frac. (%)	D^{**} Frac. (%)	Weight D^* by 0.545	Weight D^{**} by 0.210	Max. B^- (%)
1.4	61.1	27.1	33.3	5.7	10
1.6	43.4	13.8	23.7	2.9	7
1.8	24.3	4.46	13.2	0.9	4
2.0	8.16	0.44	4.5	0.1	1

Table 5.2: Contamination of the $\widetilde{M}_\nu^2$ signal from D^{**} feeddown. The second and third columns show the percentage of each lepton spectrum above the lepton momentum shown in the first column. The fourth and fifth columns show the percentages of all primary leptons in the mode above the cut, assuming 24.5/54.5/21.0 production ratios of $D/D^*/D^{**}$. The last column shows the expected percentage B^- contamination of $\widetilde{M}_\nu^2$ signal, assuming resonant D^{**} production and that D^{**} decays to $D^*\pi$ but not to $D\pi$.

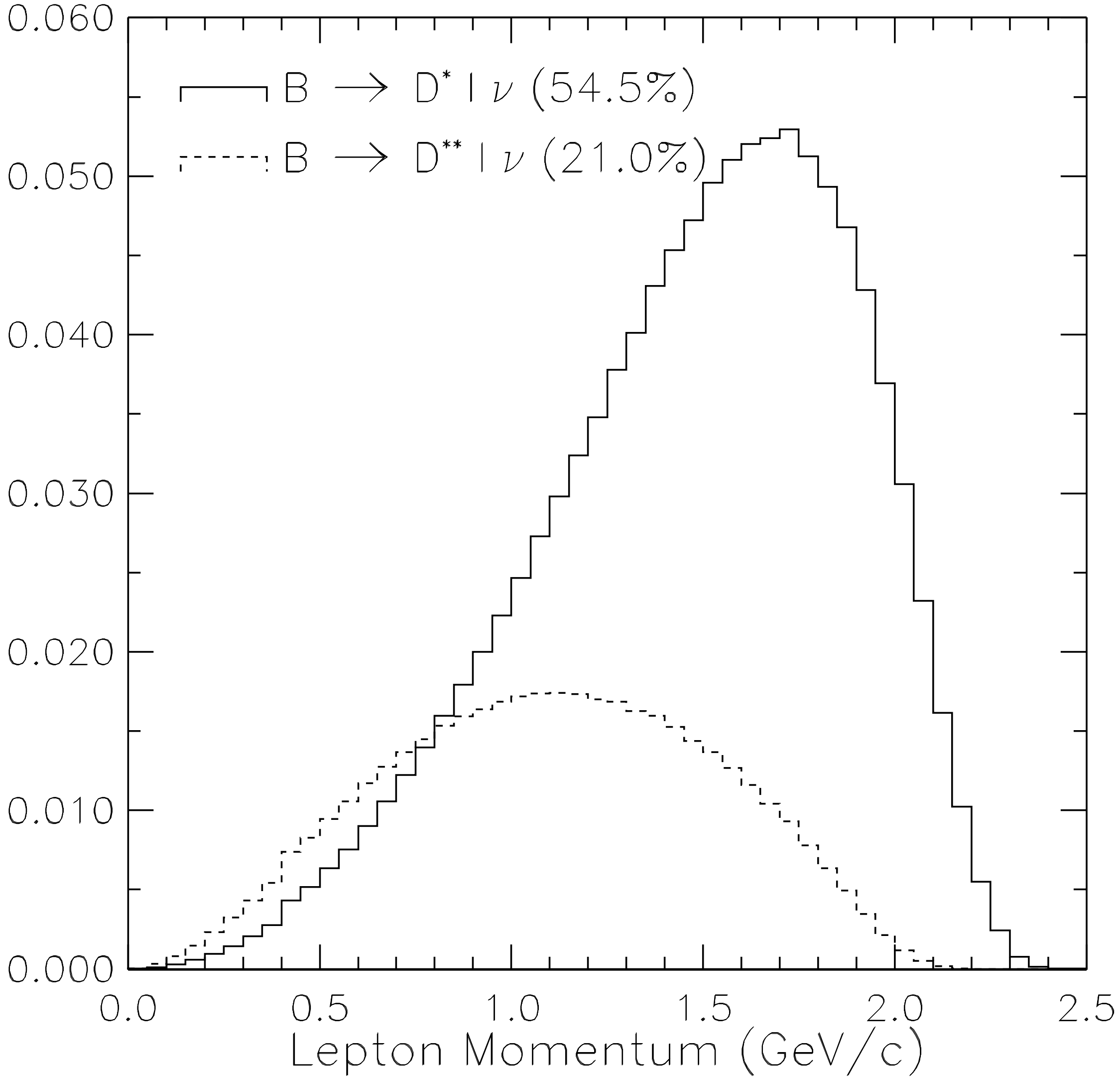

Figure 5.3: Momentum spectra of leptons from $\overline{B} \to D^* \ell^- \overline{\nu}$ and $\overline{B} \to D^{**} \ell^- \overline{\nu}$.

$\overline{B} \to D^*(D^{**})\ell^-\overline{\nu}$ lepton spectrum above a given minimum lepton momentum, and the fraction of all primary leptons above the given momentum assuming $D/D^*/D^{**}$ production fractions of 24.5/54.5/21 [55]. The last column shows the percent contamination of the $\widetilde{M}_\nu^2$ signal for the given minimum momentum requirement on the tag lepton, assuming no nonresonant production of $\overline{B} \to D^*\pi\ell^-\overline{\nu}$ and that D^{**} always decays to $D^*\pi$, not to $D\pi$. With the 1.8 GeV/c requirement, we estimate that the B^- contamination of the tags from D^{**} feeddown is therefore less than 5%.

5.5 Tag Sample

We examine the $\widetilde{M}_\nu^2$ distribution and evaluate background from several sources. The continuum contribution is estimated using the data collected at energies off resonance, corrected for luminosity and energy differences. The distribution of the background due to incorrect combinations in $\overline{B}B$ is obtained via Monte Carlo simulation. The shape is defined almost entirely by the phase space distribution. Its normalization is obtained by fitting to the data in the sideband region, $-20 < \widetilde{M}_\nu^2 < -4$ (GeV/c^2)^2. The number of tags is determined by counting candidates in the signal region ($\widetilde{M}_\nu^2 > -2$ (GeV/c^2)^2) and subtracting the backgrounds. The $\widetilde{M}_\nu^2$ distribution obtained after continuum subtraction is shown in Figure 5.4, with $\overline{B}B$ background distributions. We find 7119 ± 143 tags.

The signal peak is narrower (0.6 (GeV/c^2)^2) than the peak in the mixing analysis of Chapter 4 (0.9 (GeV/c^2)^2) . This is a consequence of requring a higher momentum lepton in the tag. When calculating $\widetilde{M}_\nu^2$, the uncertainty on the D^* 4-momentum becomes less important as the lepton momentum increases.

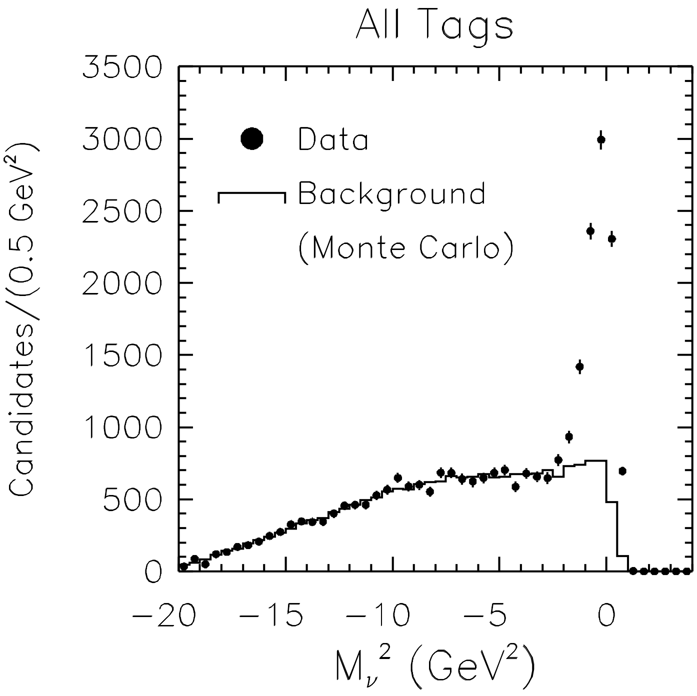

Figure 5.4: $\widetilde{M}_\nu^2$ distribution for data (off-subtracted) and for Monte Carlo $B\overline{B}$ background.

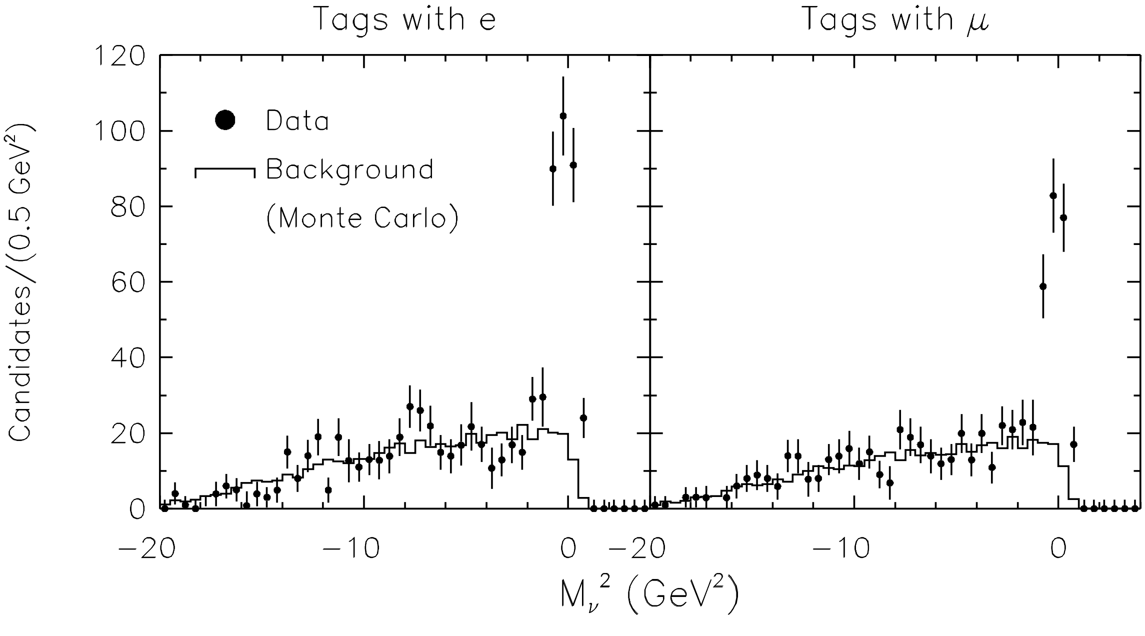

Figure 5.5: $\widetilde{M}_\nu^2$ distribution for data (off-subtracted) and for Monte Carlo $B\overline{B}$ background, for tags with an additional lepton.

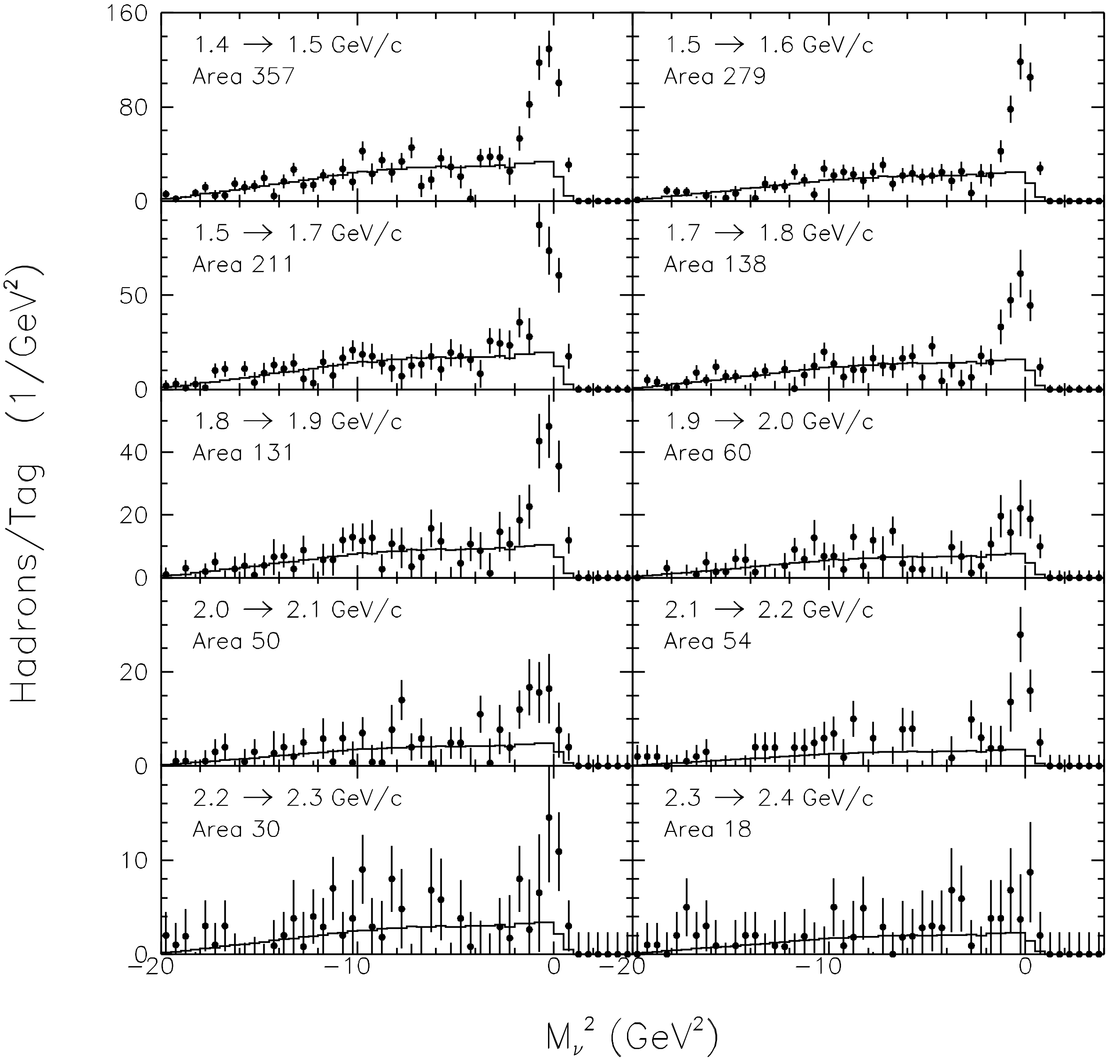

Figure 5.6: Fake determination: number of hadrons per tag for each hadron momentum bin.

5.6 Additional Leptons

Additional leptons in tagged events are required to have a momentum in the range $1.4 < p_\ell < 2.4$ GeV/c. The same $\widetilde{M}_\nu^2$ plotting procedure is applied to tagged events with an additional lepton, and the results are shown in Figure 5.5. In such events there are two leptons, and we require that the cosine of the angle between them be less than 0.99, to eliminate single tracks which are reconstructed as two.[2] The shape of the $\overline{B}B$ background is determined by Monte Carlo simulation.

The background to tags with an additional primary lepton occurs when the reconstructed tag is correct but the additional lepton is either a fake or a secondary lepton from charm decay.

5.6.1 Fakes

The number of fakes is determined as follows. First, a $\ell^+\pi^-$ tag combination is formed in the usual way. Next, a search is made for all tracks within the lepton fiducial $|\texttt{CZCD}| < 0.707$ and with $1.4 < P < 2.4$ GeV/c, but which fail electron and muon identification criteria. For every such hadron candidate encountered, the value of $\widetilde{M}_\nu^2$ is recorded in one of ten separate plots. Each plot corresponds to a different 100 MeV/c wide hadron momentum bin between 1.4 and 2.4 GeV/c. Figure 5.6 shows these ten plots. The sideband regions are then fitted to the same background shape as was used in Figure 5.4 to obtain the signal sizes in the region $\widetilde{M}_\nu^2 > -2$ GeV^2. These signal sizes represent the number of hadrons in each momentum bin across from signal tags. The appropriate electron (muon) fake rate per track is then used as

---

[2] This opening angle cut is different from the one used in the mixing measurement, which was later determined to be unnecessarily restrictive.

a weight for each hadron momentum bin to give the number of electron (muon) fakes at that momentum. The yields are then integrated from 1.4 to 2.4 GeV/c to obtain the total numbers of fakes.

5.6.2 Secondaries

After subtracting the estimated contribution from fakes, a correction is applied for the contribution of secondary leptons to the sample of neutral B's. Of all leptons from inclusive $\overline{B}B$ decay with momentum above 1.4 GeV/c, the fraction arising from secondary decay is taken to be 0.028 ± 0.008. After accounting for detection efficiencies, the fraction among detected leptons is $0.027 \pm 0.008(0.022 \pm 0.007)$ for electrons (muons). However, the situation in tagged events is different than in the inclusive environment mentioned above. After tagging, the probability of encountering a secondary leptons is twice as large because the undetected D^0 can also contribute to secondary leptons. Therefore, in this analysis the fraction of all additional leptons which are secondaries is taken to be 0.054 for electrons and 0.044 for muons.

5.6.3 Biases and Lepton Efficiency

Bias from `NTRKCD` requirement

Selecting events based on a given `NTRKCD` biases the branching fraction measurement, since the efficiency to pass the cut is different for numerator and denominator. Figure 5.7 shows the `NTRKCD` distributions in monte carlo for all tags and for tags with an additional lepton. Mean value of `NTRKCD` is slightly lower for tags with additional leptons, because the charged multiplicity of a semileptonic B decay is lower than for a generic B decay. The efficiency to pass the requirement `NTRKCD`≥ 5 is 0.5% lower for

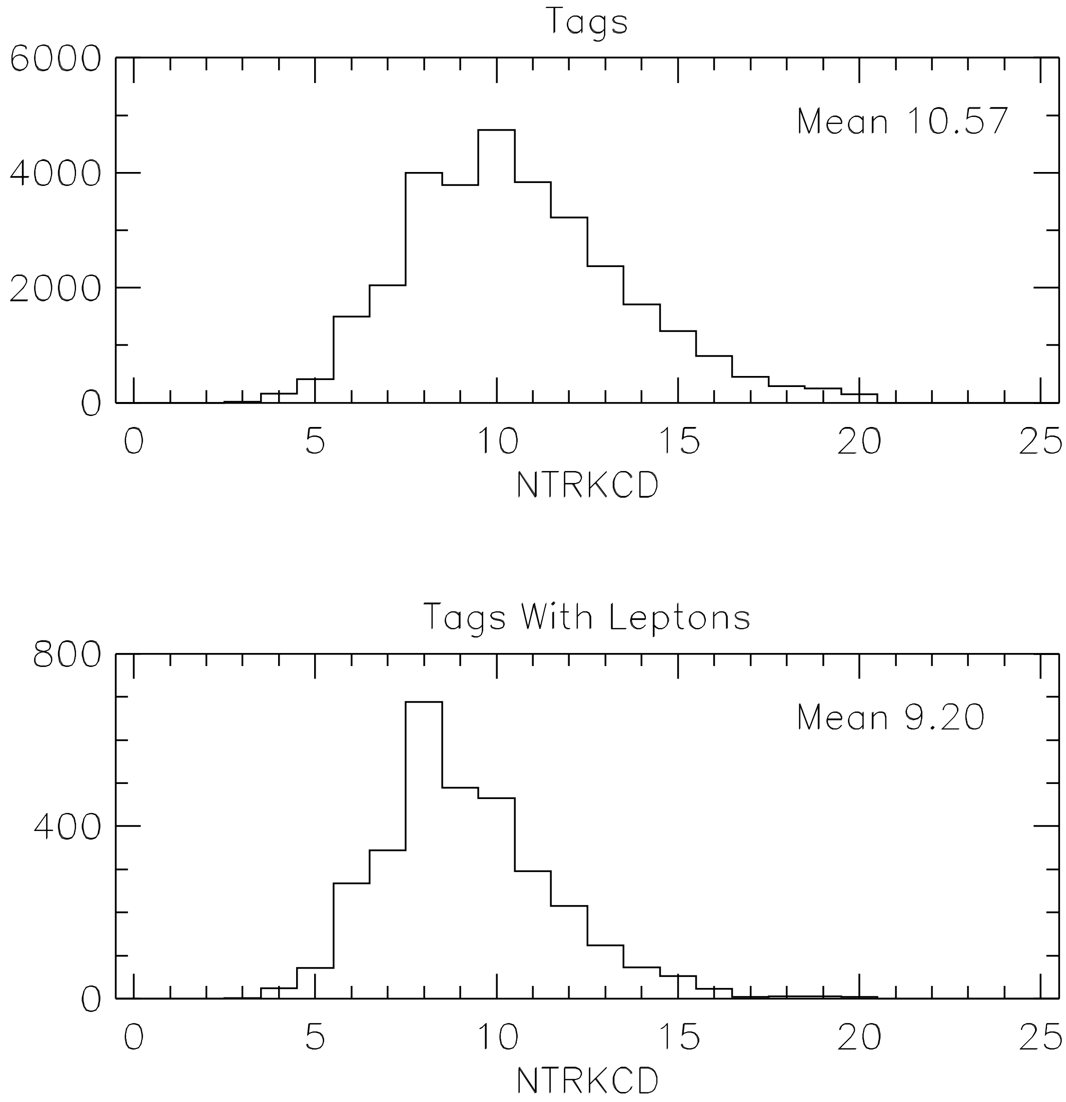

Figure 5.7: `NTRKCD` distribution for all tags and tags with an additional lepton.

tags with leptons than it is for all tags. To correct for this bias we apply a correction of +0.5% to the yield of leptons N_ℓ.

Bias from tagging efficiency

There is a bias due to different tagging efficiencies in numerator and denominator. As mentioned above, there are more tracks per event when the opposite B decays generically. The efficiency for DUET to reconstruct a track depends on the multiplicity of the environment in which the track is embedded. That is, it is more difficult to reconstruct a tag in a high multiplicity than in a low one. This mostly affects the efficiency to reconstruct the soft pion of the tag, not the lepton. This is expected because the pion track overlaps with many other tracks in the event. Thus, the efficiency to reconstruct the soft pion is more sensitive to the details about the event environment than the fast lepton. Since the average charged track multiplicity is different for events in the numerator and denominator of the branching fraction, then the average efficiency to reconstruct a tag is different for both. There is a systematic uncertainty in the size of this non-cancelation of tagging efficiency.

We determine the size of the correction for this bias by comparing the distributions of generated charged multiplicity for generic $\overline{B^0}$ decays, and for the second undetected B in a tagged event. Figure 5.8(a) and (b) shows the generated charged multiplicity of generic $\overline{B^0}$ decays in monte carlo, along with the generated charged multiplicity of B^0 across from reconstructed tags. Note the downward shift in the mean for the latter. This is due to the variation of tagging efficiency with the multiplicity of the opposite B. These two distributions have somewhat different shapes because there is a deficit in the lower plot at large multiplicities. The small difference in shapes can be seen by taking the ratio of the two distributions, shown in Figure 5.9. (Since

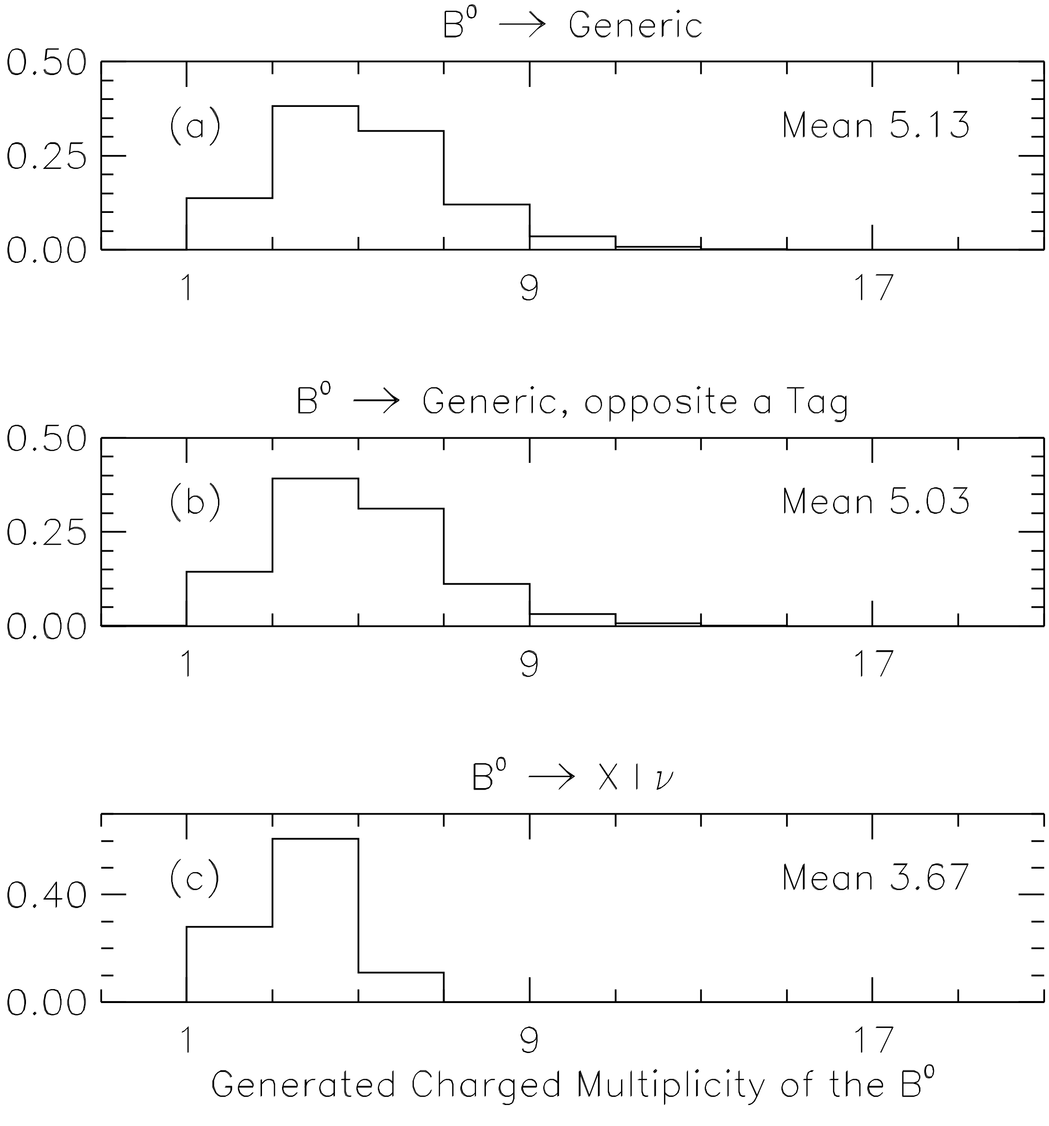

Figure 5.8: Generated charged multiplicity for (a) generic $\overline{B^0}$ decay for (b) the second B^0 in a tagged event and (c) for semileptonic $\overline{B^0}$ decay.

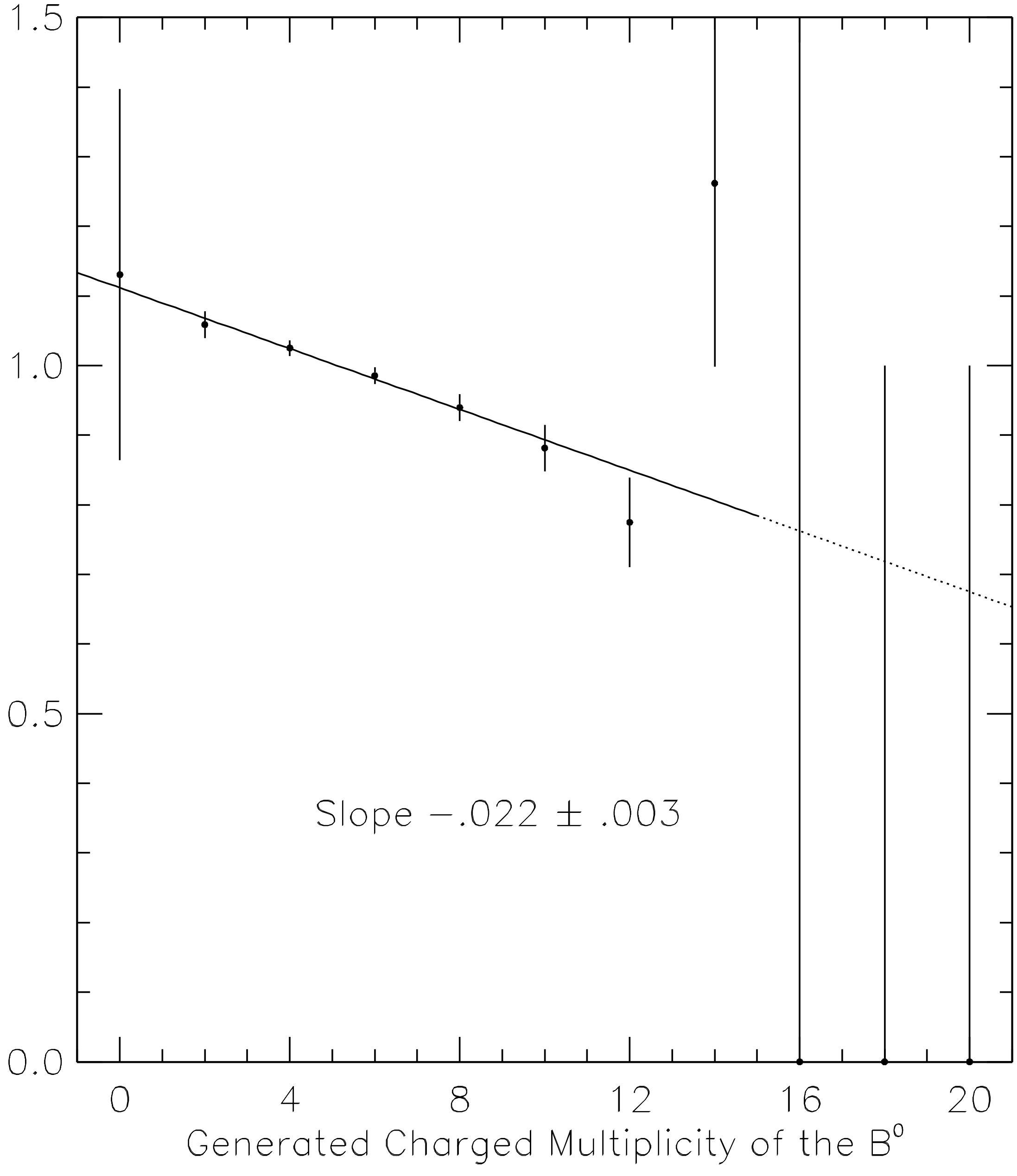

Figure 5.9: Ratio of Figure 5.8(b) to Figure 5.8(a) which determines the variation of tagging efficiency with generated charged multiplicity of the event. The slope indicates that the tagging efficiency drops by 2.2% of it's value for every extra generated charged track in the event.

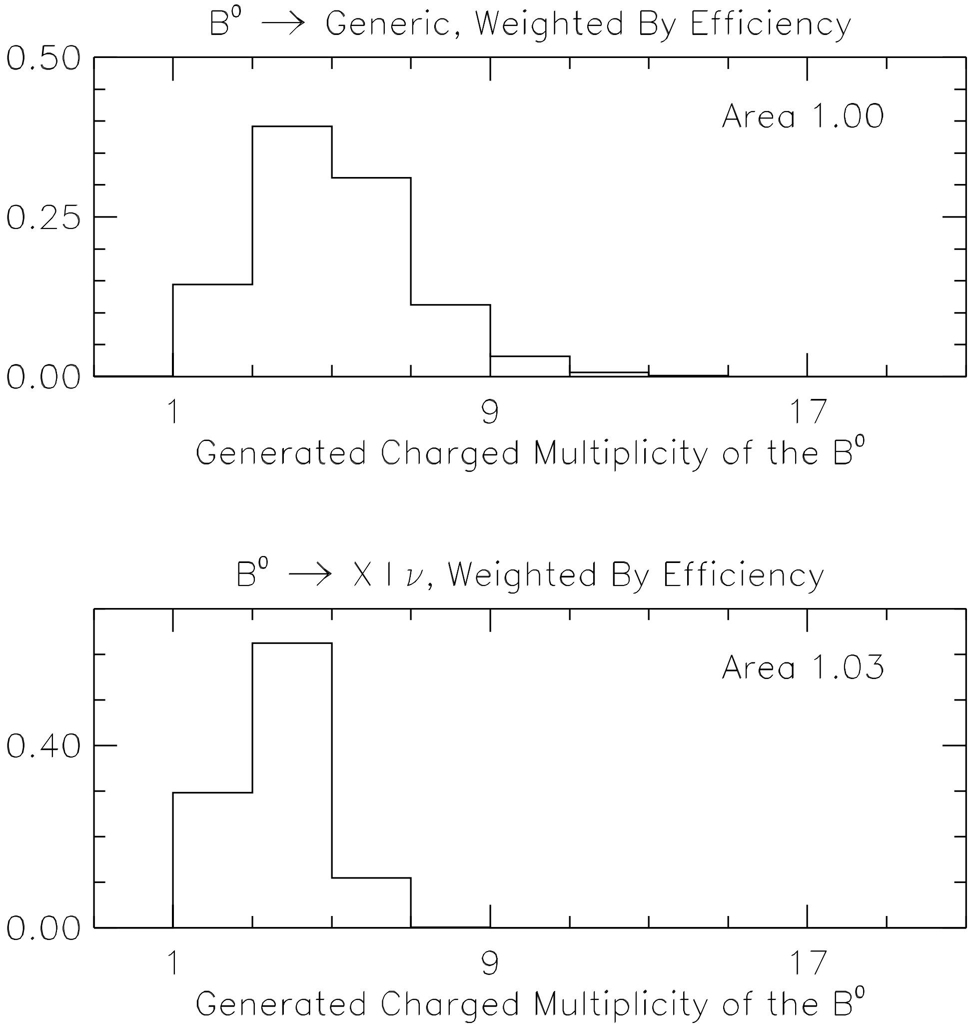

Figure 5.10: Generated charged multiplicity for generic $\overline{B^0}$ decays (upper) and for semileptonic $\overline{B^0}$ decays, weighted by relative tag reconstruction efficiency.

the initial plots both had unit area, the ratio is equal to unity at the midrange.) A linear fit to this plot gives a slope of -0.022 ± 0.003. This indicates that the tagging efficiency drops by 2.2% of its value for every extra generated charged track from the opposite B.

Figure 5.8(c) shows the generated charged multiplicity for semileptonic $\overline{B^0}$ decay. Note the shift in the means of the distribution. On average, a semileptonic $\overline{B^0}$ decay in the monte carlo has $5.1 - 3.7 = 1.4$ fewer tracks than a generic $\overline{B^0}$ decay. Thus, we expect the average tagging efficiency when the second B decays semileptonically to be $2.2\,\%/\text{track} \times 1.4\,\text{tracks} = 3.1\%$ lower than the tagging efficiency when the second B decays genericly. To properly determine the correction, we take the two distributions in Figure 5.8(a) and (c) which both have unit area, and multiply them by the relative efficiency curve of Figure 5.9. The results are shown in Figure 5.10. After weighting by the efficiency in this way, the ratio of areas is found to be 1.000/1.030. Therefore, we apply a -3.0% correction to the values for N_ℓ.

Lepton efficiency

To obtain the total numbers of primary leptons in the tag samples, N_ℓ, these raw numbers of detected primary leptons are corrected for detection efficiency in the observed momentum region, $p_\ell > 1.4$ GeV/c, then extrapolated to the unobserved region. The detection efficiency includes effects of geometric acceptance, track reconstruction and identification criteria. We find it to be 65.1% for electrons and 50.7% for muons, not yet including a reduction of 1.1% due to the requirement on the dilepton opening angle and to effects of the track multiplicity cut. To account for the unobserved portion of the spectrum, we use the ISGW model which predicts that B meson semileptonic decay consists primarily of three exclusive modes, $\overline{B} \to D\ell\nu$,

$\overline{B} \to D^{*}\ell\nu$ and $\overline{B} \to D^{**}\ell\nu$, in the percentages 27/62/11. However, based on CLEO's preliminary measurement of the inclusive lepton momentum spectrum which yields slightly different rates,[42] we take the proportions to be 24.5/54.5/21 [55]. For electrons (muons) the fraction of the spectrum above 1.4 GeV/c is found to be 48.1% (51.4%). Details of the efficiency calcluation are given in Appendix B.

Assuming lepton universality, we average the electron and muon totals to obtain N_{ℓ}. Shown in Table 5.7 are the raw numbers of tags, with and without leptons, and the various corrections applied to arrive at the semileptonic branching fraction.

5.7 Statistical and Systematic Uncertainties

About 5% of the tags are found to be identified more than once because the soft pion curls and is reconstructed as more than one track. Although this has no systematic effect on the measurement, there is some overcounting of tags both in the numerator and denominator, which is accounted for by increasing the statistical error by 2.5% of its value.

Several sources of systematic error are present in the measurement. These include the uncertainties in the lepton spectrum extrapolation, in the efficiencies for tracking and lepton identification, in the two bias corrections, in the number of fake and secondary leptons, and finally in the fits to the signal sizes in the $\widetilde{M}_{\nu}^{2}$ distributions.

The single largest contribution to the systematic error is the uncertainty in the shape of the primary lepton spectrum in order to determine the fraction of the spectrum below the momentum cutoff of 1.4 GeV/c. The error was originally conservatively estimated by changing the percentage of $\overline{B} \to D^{**}\ell\nu$ from 0% to 30% of the total semileptonic branching fraction in the ISGW model, giving an uncertainty of 8% on the result. This uncertainty can be greatly reduced in future measurements. The tagged lepton spectrum of Figure 5.2 can be used to determine directly from the data what fraction of the spectrum lies below 1.4 GeV/c, effectively eliminating all model dependence. Based on the statistical error bars in Figure 5.2 which uses the `4S1` through `4S8` datasets, the fraction of the spectrum below 1.4 GeV/c can be determined with an uncertainty of 3%, already a substantial improvement over the conservative 8% uncertainty we choose for this result.

Uncertainties in lepton identification and tracking efficiencies are 2.5% and 2.0%, respectively. The systematic uncertainty on the correction for the bias introduced by the `NTRKCD` cut is taken to be the full size of the correction, 0.5%. The systematic uncertainty on the correction for the bias introduced by the noncanceling tagging efficiencies is also taken to be the full size of the correction, 3.0%. The uncertainty in both the rates of fakes and of secondary leptons is taken to be 30%.

The remainder of this section will be devoted to a detailed discussion of the systematic uncertainty on the fits to the $\widetilde{M}_\nu^2$ distributions. In order to justify the technique of determining the systematic errors on the fits, one must first understand some details about the $\widetilde{M}_\nu^2$ distribution. The $\overline{B}B$ background of the $\widetilde{M}_\nu^2$ distribution may be separated according to their general origin – a correlated and an uncorrelated component. The correlated portion is where the lepton and pion are decay products of the same B. More specifically, the lepton is likely a primary lepton from B decay (not necessarily $\overline{B} \to D^{*+}\ell^-\overline{\nu}$), but the pion is a product of the D decay. The uncorrelated portion is where the lepton and pion originate from different B's. Again, the lepton is primary, but the pion comes either from the D *or* from the hadronization of the W. Thus, uncorrelated background consists of pions from two sources, but correlated background has pions from only one.

The correlated and uncorrelated components of the $\widetilde{M}_{\nu}^{2}$ background have different shapes, shown in Figure 5.13. This can be understood by first looking at the distribution of the cosine of the opening angle between the lepton and pion, $\cos\theta_{\ell\pi}$. Figure 5.11 shows the opening angle distribution for uncorrelated and correlated background. As expected, the uncorrelated background is nearly flat in $\cos\theta_{\ell\pi}$. The slight dip at the center is from detector acceptance effects, not a deviation from isotropy. The correlated background, however, is not isotropic and shows a clear enhancement towards $\cos\theta_{\ell\pi} = -1$. This is because the D tends to be boosted away from the lepton, and consequently the decay products of the D preferentially populate the hemisphere opposite the lepton. The "slope" of this enhancement towards $\cos\theta_{\ell\pi} = -1$ depends primarily on the momentum of the D and the charged multiplicity of the D decay. If the monte carlo correctly reproduces these, then the predicted shape for the correlated background should be reliable.

The missing mass squared is a function of lepton and pion momenta, and of their opening angle

$$\widetilde{M}_{\nu}^{2} = f(P_{\ell}, P_{\pi}, \cos\theta_{\ell\pi}). \tag{5.2}$$

Figure 5.12 shows the relationship between $\cos\theta_{\ell\pi}$ and $\widetilde{M}_{\nu}^{2}$ for the range of lepton and pion momenta passing our selection criteria for the right-sign Monte Carlo background with the prominent signal removed. If the lepton and pion are parallel, a wide range of $\widetilde{M}_{\nu}^{2}$ values are possible. On the other hand, if the pion is opposite the lepton, the value of $\widetilde{M}_{\nu}^{2}$ is forced to zero. Due to this funneling effect, the correlated background is enhanced in the $\widetilde{M}_{\nu}^{2}$ distribution near zero, shown in Figure 5.13. The uncorrelated background does not produce such a bump, but rather exhibits a plateau-like behavior in the region $-8 < \widetilde{M}_{\nu}^{2} < 0$.

	Correlated	Uncorrelated
Right-sign	32 %	68 %
Wrong-sign	18 %	82 %

Table 5.3: Composition of right-sign background and wrong-sign distribution

The right-sign ($\ell^+\pi^-$) and wrong-sign ($\ell^+\pi^+$) $\widetilde{M}_\nu^2$ background distributions are expected to have different ratios of correlated:uncorrelated components. This is simply due to arguments of charge conservation. Consequently, the overall shapes of the right and wrong-sign distributions are *different*. This is the reason why the wrong-sign distribution is not used to model the shape of the right-sign. Rather, the monte carlo right-sign background shape is used to estimate the background in data under the signal. Table 5.3 shows the relative abundance of correlated and uncorrelated components of the right and wrong-sign distributions as predicted by monte carlo.

There is another consequence which follows from the above discussion. Recall that two kinds of plots are made. First, the right-sign $\widetilde{M}_\nu^2$ distribution is plotted for all $\ell^+\pi^-$ pairs passing our cuts. Then the subset of the initial distribution is considered for which there exists a second fast lepton (e or μ), presumably from the semileptonic decay of the second B. As was shown above, the uncorrelated fraction of the background for the full sample was about two-thirds. For the lepton subsamples, the correlated:uncorrelated mixture is expected to be different. In the lepton subsamples, it is no longer possible to get an uncorrelated pion from the hadronization of the W, since the W is decaying to a lepton and neutrino. Therefore the two components should be more nearly equal in size. This will result in the lepton subsample having a slightly different background shape than the full sample. We take advantage of the fact that there should be little, if any, difference between the muon and electron subsamples. This allows the sum of the monte carlo electron

	Correlated	Uncorrelated
Right-sign (full sample)	32 %	68 %
Right-sign (lepton subsample)	46 %	54 %

Table 5.4: Composition of right-sign background for the full sample and for the lepton subsample.

subsample and muon subsample background shapes to be taken, and used to fit each of the electron and muon subsamples in data. The two shapes are combined in order to reduce the statistical error bars by a factor of $\sqrt{2}$. Table 5.4 shows the composition of the right-sign background for the full sample and the lepton subsamples, as predicted by monte carlo.

In order to quantify the systematic error on the estimates of the background sizes (and thus the signal sizes), the agreement between the shapes of the *wrong-sign* distributions in monte carlo and data is examined. The same fitting procedures are applied to the wrong-sign distributions as are used in the right-sign, and a comparison is made between the monte carlo prediction for the background size in the region $\widetilde{M}_\nu^2 > -2$ with the known value from data. The size of the discrepancy, if any, is taken to be the size of the systematic error on the right-sign background estimates. In doing so, we make the assumption that the monte carlo can correctly model the right-sign distribution if it can correctly model the wrong-sign distribution. *This is a valid assumption.* We have shown above that the two distributions contain the *same* physics processes (correlated and uncorrelated components), except in somewhat different mixtures.

Figure 5.14 shows the wrong-sign distribution in data, with the wrong-sign monte carlo shape fit in the sideband region $-20 < \widetilde{M}_\nu^2 < -4$. Based on this fit, the predicted area in the region $-2 < \widetilde{M}_\nu^2$ is 3416 ± 52. The actual area is 3336 ± 83. The

	$\ell^+\pi^+$ (all)	$\ell^+\pi^+$ (with μ)	$\ell^+\pi^+$ (with e)
MC prediction, $\widetilde{M}_\nu^2 > -2$	3416 ± 52	105.1 ± 7.7	124.0 ± 8.4
Actual area, $\widetilde{M}_\nu^2 > -2$	3336 ± 83	101.5 ± 12.1	133.5 ± 13.4
Actual − predicted	-80 ± 97	-3.6 ± 14.3	$+9.5 \pm 15.8$
Actual − predicted (%)	-2.3 ± 2.9	-3.4 ± 13.6	$+7.7 \pm 12.7$
Worst case difference (%)	5.2	17.0	20.4
	$\ell^+\pi^-$ (all)	$\ell^+\pi^-$ (with μ)	$\ell^+\pi^-$ (with e)
MC background prediction	3587	82.2	95.3
Uncertainty, from above	186	14.0	19.4
Signal size	7120	197.7	271.9
Systematic error on signal (%)	2.6	7.1	7.1

Table 5.5: Determination of systematic errors on signal sizes

difference measured − predicted is -80 ± 97. Converting this to a percentage of the predicted area, the actual area differs from the predicted area by $-2.3 \pm 2.9\%$. This is consistent with zero, and does not indicate any problem with the monte carlo. On the other hand, the discrepancy could be at worst $\mathrm{ABS}(-2.3) + 2.9\% = 5.2\%$. To be conservative, this is taken to be the systematic error on the size of the background in the right-sign distribution. Unfortunately, this is not the number we are ultimately interested in. What is desired is the fractional systematic error on the signal size. The monte carlo prediction for the background size in the right-sign is 3587. Taking 5.2% of this number, the systematic error is found to be 186. The central value for the signal size is 7120. Therefore, the percent systematic error on the signal size is $186/7120 = 2.6\%$.

A similar procedure is used for the wrong-sign lepton subsamples. This is done separately for the muon and electron subsamples. The $\widetilde{M}_\nu^2$ distribution is plotted for $(\ell^+\pi^+)$ pairs when there is an additional fast muon present, and separately when there is an additional fast electron present. The shape which is used to fit both these

Source	% error
Fit to number of tags	2.6
Fit to number of tags with leptons	7.1
Fake leptons	0.2
Secondary leptons	1.6
Correction for event selection bias	0.5
Correction for tagging efficiency bias	3.0
Spectrum shape	8.0
Tracking efficiency	2.0
Lepton identification efficiency	2.5
Total	12.0

Table 5.6: Systematic errors on branching fraction.

distributions is the sum of the two wrong-sign lepton subsamples in the Monte Carlo. The fits are shown in Figures 5.15 and 5.16, and the result are shown in Table 5.5, along with the above numbers already described. The percent systematic error on the signal sizes for the lepton subsamples is found to be 7.1% in both cases. We assume that this potential systematic error is 100% correlated between the two subsamples and will not cancel when taking the lepton average. Thus, the overall error on the signal sizes in the lepton subsample is taken to be 7.1%.

In this way, the systematic error on the monte carlo fits is determined by directly comparing the monte carlo with data. Note also that these systematics errors are largely determined by the *statistics of the test*, which is limited by the size of the data, not the monte carlo. Thus, these systematic errors should decrease with more data, unless and until a discrepancy between monte carlo and data becomes apparent.

We add the sources in quadrature for the total systematic error. The systematic uncertainties are summarized in Table 5.6

lepton requirement	
none	7119 ± 143
e	271.9 ± 22.7
fake	1.5 ± 0.4
secondaries	14.6 ± 4.3
primary observed	255.8 ± 23.1
corrected e (N_e)	801.2 ± 72.4
μ	197.7 ± 20.7
fake	8.3 ± 2.5
secondaries	8.3 ± 2.7
primary observed	181.1 ± 21.0
corrected μ (N_μ)	681.5 ± 79.1
N_ℓ average	746.8 ± 53.4
$\mathrm{Br}(\overline{B^0} \to X\ell^-\overline{\nu})$	10.5 ± 0.8

Table 5.7: Numbers of decays reconstructed without and with a requirement of additional leptons, with corrections applied to obtain semileptonic branching fraction.

5.8 Result

The neutral B semileptonic branching fraction measurement using these tags is then

$$\mathrm{Br}(\overline{B^0} \to X\ell^-\overline{\nu}) = (10.5 \pm 0.8 \pm 1.3)\% \tag{5.3}$$

where all systematic uncertainties have been added in quadrature. This is the world's most precise measurement of the $\overline{B^0}$ semileptonic branching fraction. This tagged measurement does not depend on assumptions about non-$\overline{B}B$ decays of the $\Upsilon(4S)$. Because we make the approximation that the tag sample is pure $\overline{B^0}$, there is a small dependence on the ratio f_+/f_0 from B^- contamination via D^{**} feeddown, but this dependence vanishes if the lifetime ratio is unity.

5.9 The Ratio of Lifetimes

The rate of exclusive semileptonic decay in $\Upsilon(4S)$ events is proportional to the product of the semileptonic branching fraction and the production rate of the parent particle. The ratio of rates from charged and neutral B's is then equal to $(b_+ f_{+-})/(b_0 f_{00})$, where f_{+-} and f_{00} are the production fractions, and has been measured by CLEO and ARGUS[56, 57]. This may be considered a measurement of b_+/b_0 under the assumption that $f_{+-}/f_{00} = 1$, but the uncertainty on this assumption is a major source of systematic error.

Three similar tagged semileptonic branching fraction measurements have been made by other collaborating members of the CLEO experiment using the same dataset but different tagging techniques. It is beyond the scope of this thesis to discuss their work in great detail, but their results are presented here for completeness in order to arrive at an overall measurement of the lifetime ratio. These other results include two additional measurements of b_0, and the first measurement of b_+.

The first of these three additional measurements uses a partial reconstruction technique applied to the hadronic decay $\overline{B^0} \to D^{*+}\pi^-, D^{*+} \to D^0\pi^+$. As in the method presented in this thesis, the mode is identified without benefit of the D^0 reconstruction. Starting with the two pions, energy conservation gives the D^0 energy, and consequently the opening angle θ between the D^0 and π^+ in the laboratory. The only remaining unknown is the azimuthal angle ψ of the π^+ relative to the D^{*+} boost axis, and this is chosen to maximize the apparent reconstructed B meson mass, or pseudomass. For true $\overline{B^0} \to D^{*+}\pi^-$ events, this quantity will lie in a narrow region between the mass of the B meson and the beam energy. Using this technique, a total of 822 ± 53 tags are reconstructed. Corrections must be made for biases introduced by event shape cuts, and by noncanceling tag efficiency. All tag combinations are accepted in this analysis, so there is no bias introduced from choosing a best candidate. The neutral B semileptonic branching fraction obtained using this method is $(10.2 \pm 2.0 \pm 1.3)\%$.

The second measurement uses fully reconstructed hadronic decays of neutral B mesons as a tag. The eight reconstruction modes are $\overline{B^0} \to D^+\pi^-$, $D^{*+}\pi^-$, $D^+\rho^-$, $D^{*+}\rho^-$, $D^+a_1^-$, $D^{*+}a_1^-$, ψK_s^0, ψK^{*0}. The daughter particle momenta $\mathbf{p}_i$ and energies E_i are summed to form $\mathbf{p}_B$ and E_B. Two figures of merit are calculated which are used to identify signal. First, the beam constrained mass M_B is defined as $M_B = \sqrt{E_{\rm beam}^2 - (\mathrm{p}_{\mathbf{i}})^2}$. Second, the normalized energy difference $\delta(\Delta E)$ is taken to be $(E_{\rm beam} - E_B)/\sigma(\Delta E)$, where $\sigma(\Delta E)$ is the expected resolution on the energy difference for a particular decay mode. The signal is taken to be the size of the peak in the M_B distribution at the B meson mass after requiring $\delta(\Delta E) \simeq 0$. The sidebands of the $\delta(\Delta E)$ distribution are used to estimate the M_B background. In this manner, 515 ± 31 neutral B tags are reconstructed. A correction must be made for bias introduced by event shape cuts. The additional bias introduced by tag efficiency variation is found to be twice as large for this tagging method as for the partially reconstructed tags, 6% averaged over all decay modes. Finally, unlike the other tags, a decision is made which tag combination to retain among all possibilities in the event, and extra systematic error is assigned to account for any potential bias. This method obtains a neutral B semileptonic branching fraction of $(13.5 \pm 2.6 \pm 2.0)\%$.

The third measurement is the only one of the charged B semileptonic branching fraction. This tag is similar to the previous one, fully reconstructing the hadronic decay modes $B^- \to D^0\pi^-$, $D^{*0}\pi^-$, $D^0\rho^-$, $D^{*0}\rho^-$, $D^0a_1^-$, $D^{*0}a_1^-$, ψKM, ψK^{*-}. Unlike the neutral B tags, additional leptons of only one sign are accepted, eliminating the need for the small correction for secondary leptons from charm decay. In all other respects, this technique is the same as the previous one. The number of charged B tags is 834 ± 42, and the charged B semileptonic branching fraction is measured to be $(10.1 \pm 1.8 \pm 1.5)\%$.

In summary, the four measurements are

$$\begin{array}{rll} \mathrm{Br}(\overline{B^0} \to X\ell^-\bar{\nu}) = & (10.5 \pm 0.8 \pm 1.3)\% & \text{This Thesis,} \\ \mathrm{Br}(\overline{B^0} \to X\ell^-\bar{\nu}) = & (10.2 \pm 2.0 \pm 1.3)\% & \text{Partial Hadronic,} \\ \mathrm{Br}(\overline{B^0} \to X\ell^-\bar{\nu}) = & (13.5 \pm 2.6 \pm 2.0)\% & \text{Full Hadronic,} \\ \mathrm{Br}(B^- \to X\ell^-\bar{\nu}) = & (10.1 \pm 1.8 \pm 1.5)\% & \text{Full Hadronic.} \end{array}$$

We average the three B^0 measurements, using the quadratic sum of statistical and uncorrelated systematic errors to determine the relative weights. The final CLEO results for the charged and neutral B branching fractions are therefore

$$\begin{array}{rll} \mathrm{Br}(B^- \to X\ell^-\bar{\nu}) = & (10.1 \pm 1.8 \pm 1.5)\%, & \text{CLEO} \\ \mathrm{Br}(\overline{B^0} \to X\ell^-\bar{\nu}) = & (10.9 \pm 0.7 \pm 1.1)\%. & \text{CLEO} \end{array}$$

Both are consistent with our measurement of the average B branching fraction, $(10.96 \pm 0.07 \pm 0.22)\%$[42].

In taking the ratio, the systematic uncertainties of the lepton spectrum shape, tracking efficiency and lepton identification cancel, yielding

$$\frac{b_+}{b_0} = 0.93 \pm 0.18 \pm 0.12. \tag{5.4}$$

This result was published in reference [58] and is consistent with lifetime ratios from ALEPH $(1.00^{+0.14}_{-0.13} \pm 0.08)$[59], DELPHI $(1.02^{+0.13+0.13}_{-0.10-0.10})$ [60], OPAL $(0.94 \pm 0.12 \pm 0.07)$ [60] and CDF $(1.02 \pm 0.16 \pm 0.05)$ [61], as well as with theoretical expectations. It is also in agreement with CLEO's other result [56] and the ARGUS measurement [57] under the assumption that $f_{+-}/f_{00} = 1$.

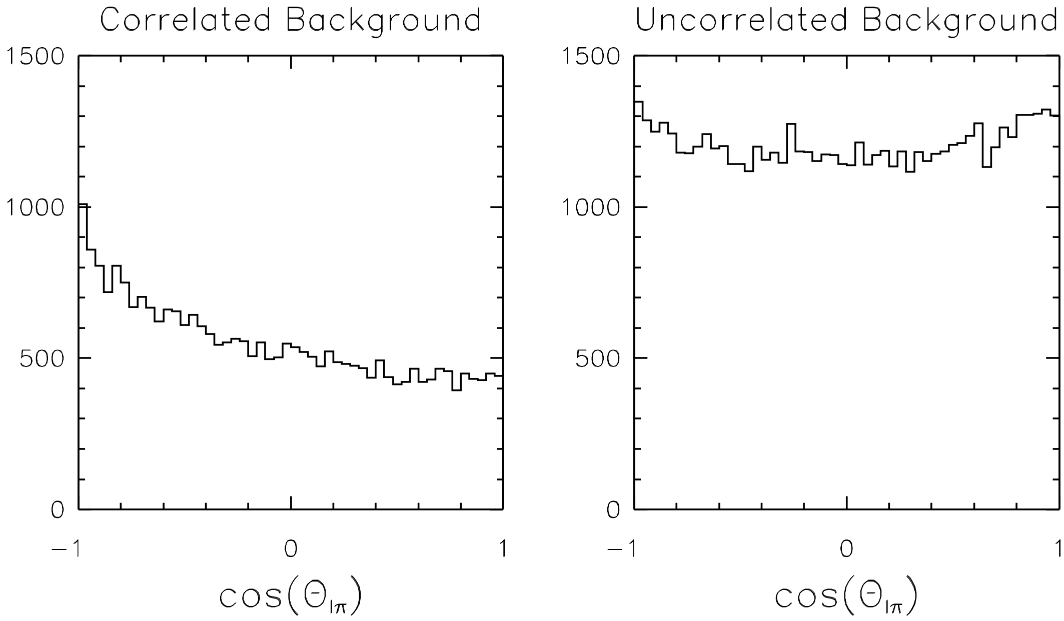

Figure 5.11: Cosine of opening angle between lepton and pion for correlated and uncorrelated background.

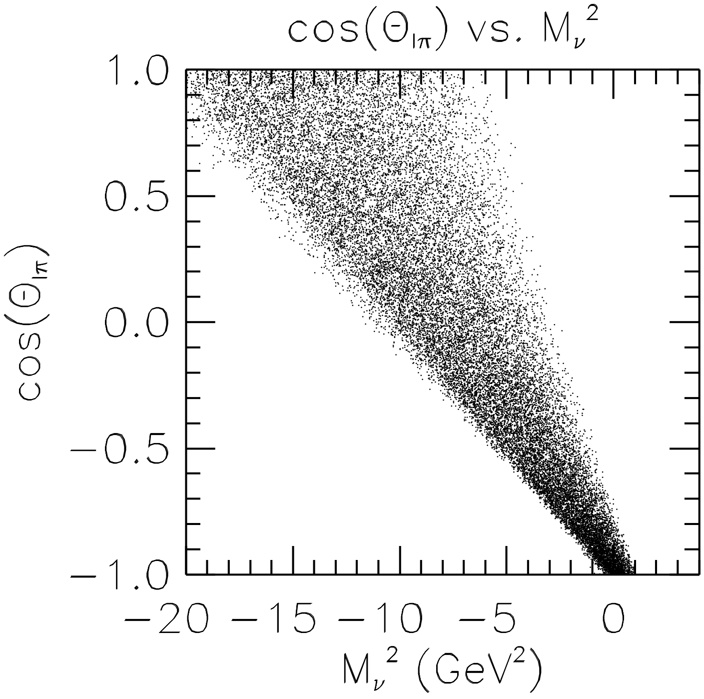

Figure 5.12: Relationship between cosine of opening angle and $\widetilde{M}_\nu^2$ for the momenta passing our requirements.

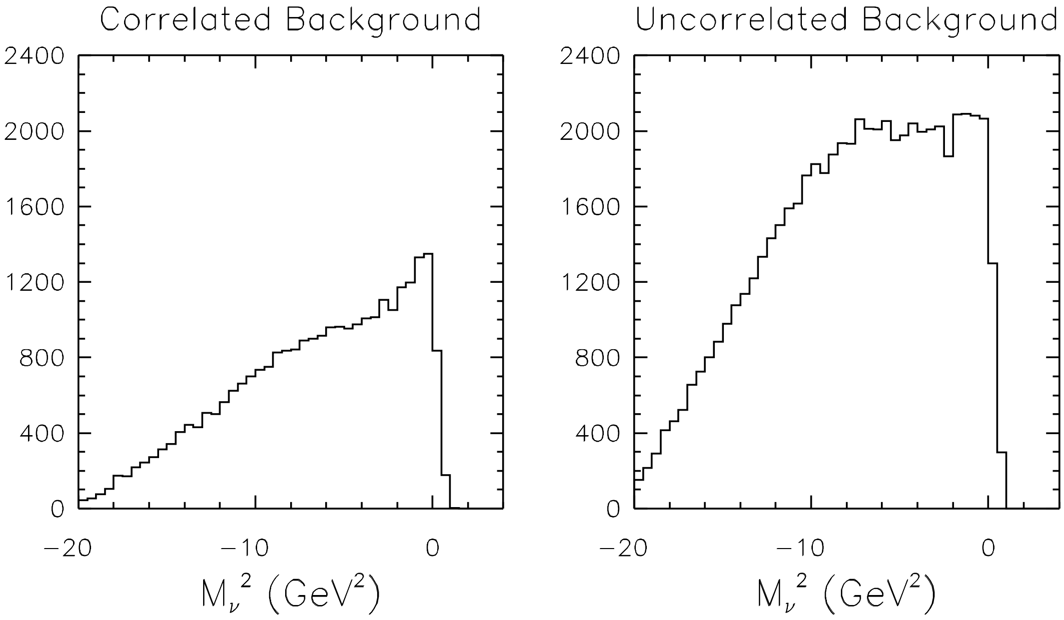

Figure 5.13: $\widetilde{M}_\nu^2$ for correlated and uncorrelated background.

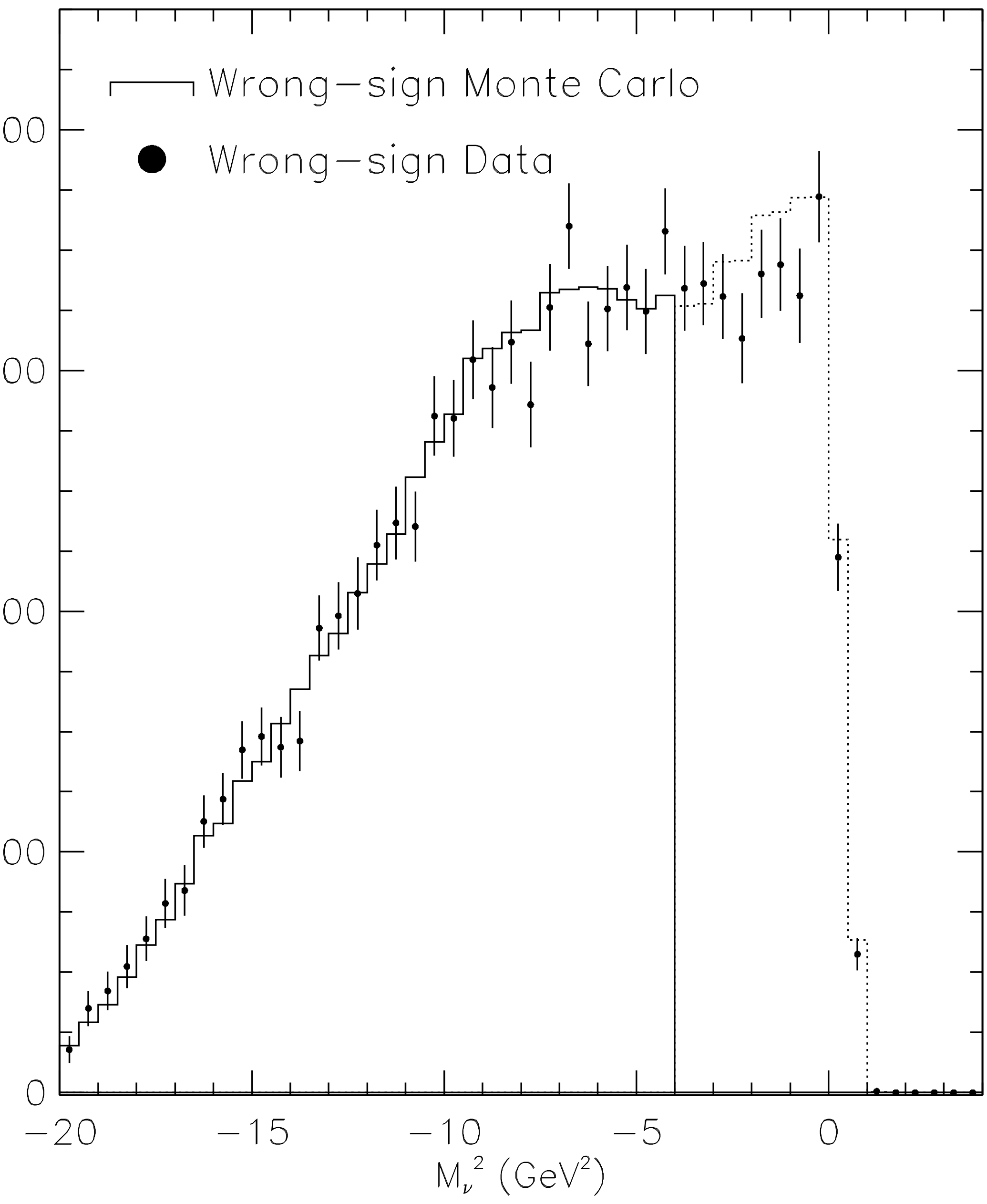

Figure 5.14: Fitting the wrong-sign monte carlo to the wrong-sign data. Results listed in first column of Table 5.5, top half.

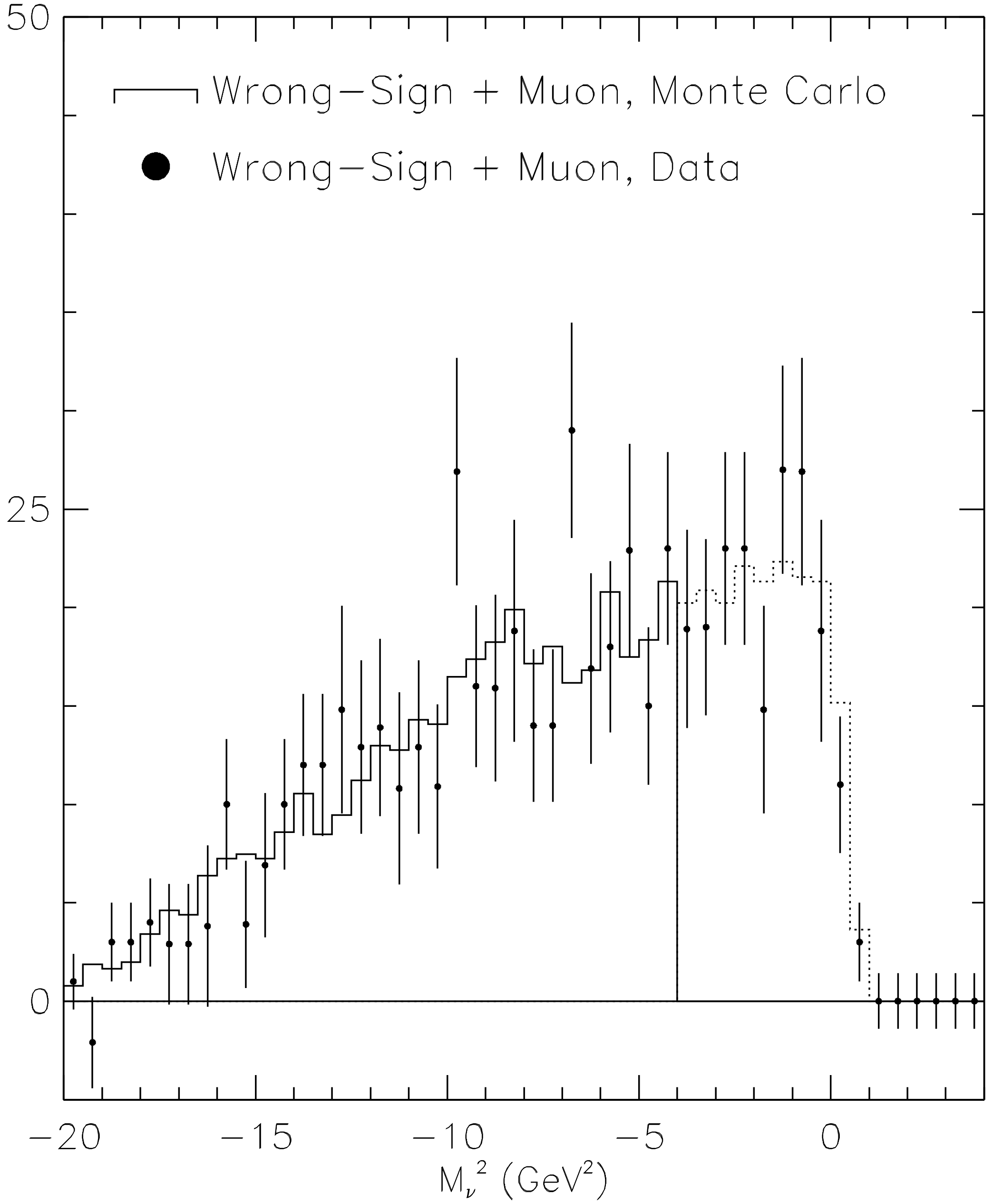

Figure 5.15: Fitting the wrong-sign monte carlo to the wrong-sign data, muon subsample. Results listed in second column of Table 5.5, top half.

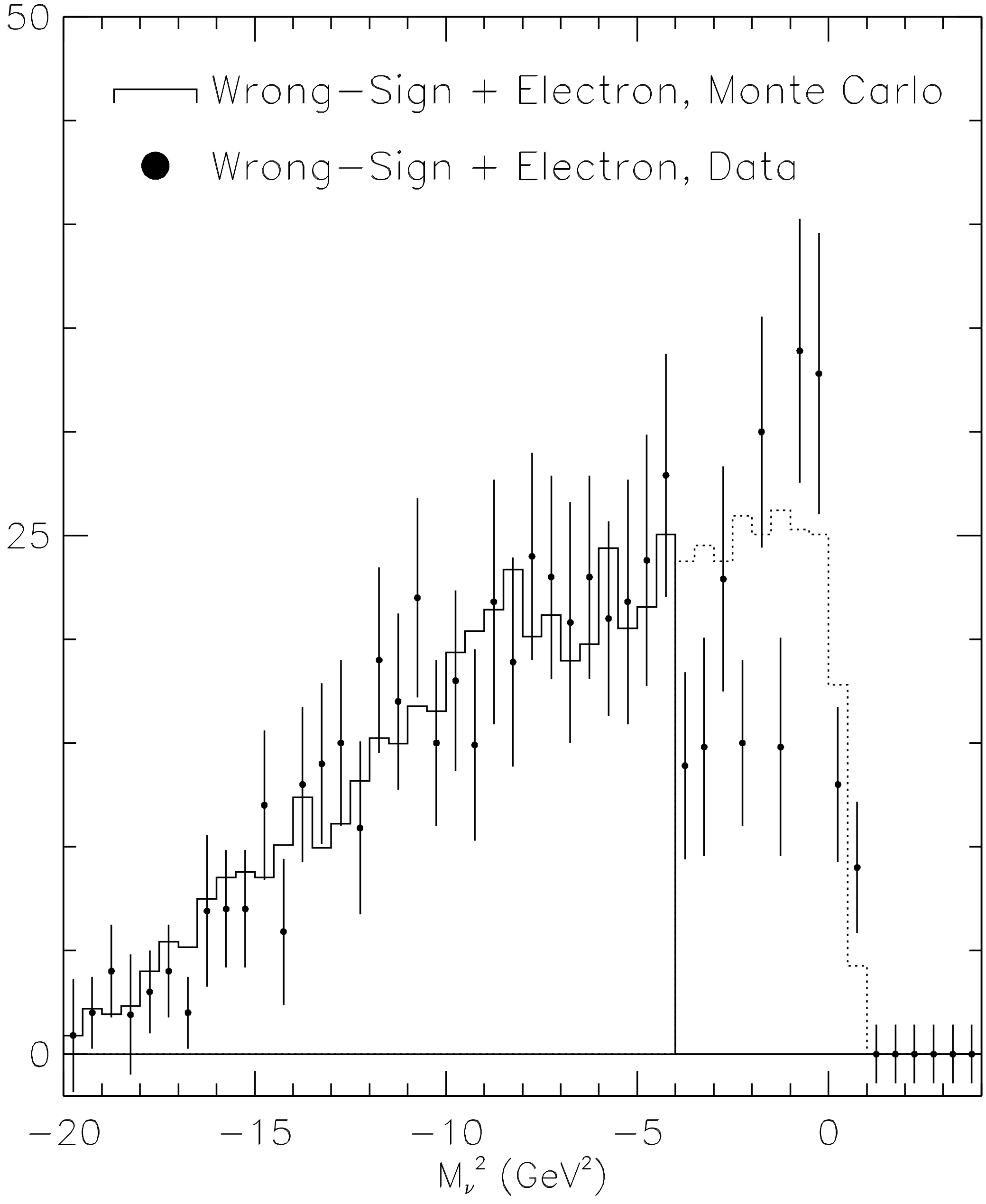

Figure 5.16: Fitting the wrong-sign monte carlo to the wrong-sign data, electron subsample. Results listed in third column of Table 5.5, top half.

Chapter 6

Conclusion

This thesis has presented measurements of two properties of the neutral B_d meson, the mixing probability χ_d and the semileptonic branching fraction $\overline{B^0} \to X\ell^-\bar{\nu}$. We find

$$\chi_d = 0.149 \pm 0.023 \pm 0.019 \pm 0.010 \tag{6.1}$$

and

$$\mathrm{Br}(\overline{B^0} \to X\ell^-\bar{\nu}) = (10.5 \pm 0.8 \pm 1.3)\%. \tag{6.2}$$

The tagged measurement of χ_d has a systematic error due to uncertainty in $\Lambda = f_+b_+^2/(f_+b_+^2 + f_0b_0^2)$ which is significantly smaller than for the alternative dilepton method. Using a value of the B^0 lifetime measured at other experiments, the mass difference between the eigenstates of CP, ΔM, is extracted. There is a significant uncertainty on the determination of the CKM matrix element V_{td} due to imprecise knowledge of the decay constant f_B. A better determination of V_{td} cannot be made until f_B is known with more precision. The constraint imposed by this mixing measurement on the allowed region of the $\rho - \eta$ plane is consistent with measurements of charmless semileptonic B decay and from measurement of $|\epsilon|$ from CP-violating neutral kaon decays.

Additional data from the $\Upsilon(4S)$ may aid in a more precise determination of $|V_{td}|$ through a somewhat indirect means. More data will given an improved measurement of the purely leptonic decay rate $\Gamma(D_s \rightarrow \mu^+\nu_\mu)$ and consequently the decay constant f_{D_s}. This is an unambiguous test of lattice QCD, and should in turn help in the determination of f_B from the lattice.

The $\overline{B^0}$ semileptonic branching fraction measurement is consistent with CLEO's measurement of the inclusive lepton production at the $\Upsilon(4S)$, suggesting that non-$\overline{B}B$ decays of the $\Upsilon(4S)$ are probably not contributing to the puzzle of the semileptonic branching fraction. It is also consistent CLEO's model-independent lepton tagged measurement of the average B semileptonic branching fraction. Combining this tagged $\overline{B^0}$ branching fraction with measurements made by other collaborators of the B^- and $\overline{B^0}$ semileptonic branching fractions, an value of the lifetime ratio is obtained which is consistent with unity.

This branching fraction measurement is less than the minimum 12.5% which has has recently been expected by theory, adding to the growing body of evidence that the discrepancy is a real one. One must then determine if the shortcoming lies with the measurements, the calculations, or both.

Many hypotheses have been proposed to explain this discrepancy. A sampling include the presence of uncounted portions of the semileptonic branching fraction, the presence of unusually large nonspectator contributions to the hadronic width, an unexpectedly small charm quark mass, and unexpectedly large higher order contributions to the nonperturbative QCD corrections.

The discrepancy is unlikely to be due to unobserved semileptonic B decays involving either τ leptons or baryons. ALEPH has measured the B semi-tauonic branching fraction $\mathrm{Br}(\overline{B} \rightarrow X\tau^-\bar{\nu}_\tau) = (2.76 \pm 0.47 \pm 0.43)\%$ which is consistent with expectations[62]. A search was made by the ARGUS collaboration for semileptonic decay $\overline{B^0} \rightarrow \Lambda_c^+ \bar{p}\ell^-\overline{\nu}$ by searching for a lepton and proton in an event tagged by another fast lepton tag. No events were found and they set an upper limit of 0.16% for this branching fraction[54].

If anomalously large non-spectator processes occurred in B decay, the semileptonic branching fraction could be reduced. CLEO has set an upper limit on the purely leptonic channel $B^- \rightarrow \tau^-\bar{\nu}_\tau$ of 2.2×10^{-3}[23]. The charmless hadronic decays $B \rightarrow K\pi$ and $B \rightarrow \pi\pi$ have contributions from hadronic penguins, and CLEO has evidence for their existence at the level of 10^{-5}[63]. Another rare process, the electromagnetic penguin decay $B \rightarrow K^*\gamma$ has been observed with a branching fraction of approximately 10^{-5}[64]. All of these results are consistent with expectations and do not indicate any evidence for enhanced non-spectator processes contributing to the total width of the B meson.

Another means of enhancing the hadronic width is to lower the mass of the charm quark, increasing the rate for the transition $b \rightarrow c\bar{c}s$. Although a smaller charm mass would drive the semileptonic branching fraction in the desired direction, it would increase the average number of charm quarks produced per B decay. For a nominal charm quark mass, the expected charm content of B decay lies in the range 1.1 – 1.2, while CLEO has measured the content to be 1.10 ± 0.06 charm and anticharm quarks per B meson decay[24]. If the charm quark were lowered to solve the semileptonic branching puzzle, the expected yield would rise, creating an inconsistency with the data. Therefore, a low charm quark mass alone seems to be an unacceptable means of explaining the semileptonic branching fraction puzzle.

It has been suggested that if the resolution of the puzzle were due to unusually large higher-order nonperturbative corrections, then the ratio of lifetimes would be expected to differ significantly more from unity than shown in Equation 2.39[65]. Yet the lifetime ratio measured by CLEO and other experiments seems to be consistent with unity and theoretical expectations, tending to discount this possibility. This serves to remind us that measurement of the lifetime ratio is an important element to the understanding of the semileptonic branching fraction puzzle.

There have been recent developments with the calculation of next-to-leading order radiative QCD corrections to the hadronic width which take into account the finite mass of the charm quark[66, 67]. The authors account for effects in both $b \to c\bar{u}d$ and $b \to c\bar{c}s$ transitions. The authors predict a B meson semileptonic branching fraction of $(12.0 \pm 1.4)\%$ using pole quark masses, or alternatively $(11.2 \pm 1.7)\%$ using running $\overline{\mathrm{MS}}$ masses.

In spite of these intriguing possibilities, there is as yet no consensus in the physics community as to the source of the discrepancy, and the issue remains a controversial one. This thesis has presented additional evidence that, like the average B semileptonic branching fraction, the $\overline{B^0}$ branching fraction as well is below 12.5%.

Appendix A

Full Form for χ_d

The relationship betwen χ_d and M is

$$\chi_d = \frac{aM - b}{cM + d}. \tag{A.1}$$

When $f_+/f_0 = b_+/b_0 = 1$, the coefficients are

$$a = (1 - F^R) + NF^R(1 - f^f)(1 - f_c)(\epsilon_u^{\mathrm{eff}} + \frac{\epsilon_+^{\mathrm{tag}}}{\epsilon_u^{\mathrm{tag}}}\epsilon_+^{\mathrm{eff}}) + F^R(1 - f^f)f_c \tag{A.2}$$

$$b = F^R(1 - f^f)f_c \tag{A.3}$$

$$c = (1 - F^R)(1 - 2f^{**}/3) + NF^R(1 - f^f)(1 - f_c)\epsilon_u^{\mathrm{eff}} - F^R(1 - f^f)f_c/2 \tag{A.4}$$

$$d = (1 - F^R)(1 - 2f^{**}/3) + NF^R(1 - f^f)(1 - f_c)\frac{\epsilon_m^{\mathrm{tag}}}{\epsilon_u^{\mathrm{tag}}}\epsilon_m^{\mathrm{eff}} - F^R(1 - f^f)f_c/2. \tag{A.5}$$

These expressions become more complicated if the dependences on f_+/f_0 and b_+/b_0 are included. These must be included in order to evaluate the sensitivity of χ_d to variations in Λ. The full expressions are

$$\begin{aligned} a = \; & (1 - F^R)(1 - f^{**} + f^{**}(1 + 2\alpha\beta)/(1 + 2\alpha)) + \\ & NF^R(1 - f^f)(1 - f_c)(\epsilon_u^{\mathrm{eff}}\alpha\beta\frac{\epsilon_+^{\mathrm{tag}}}{\epsilon_u^{\mathrm{tag}}}\epsilon_+^{\mathrm{eff}}) + \\ & F^R(1 - f^f)f_c(1 + \beta)/2 \end{aligned} \tag{A.6}$$

$$b = F^R(1 - f^f)f_c(1 + \beta)/2 \tag{A.7}$$

$$\begin{aligned} c = \ & (1 - F^R)(1 - 2\alpha f^{**}/(1 + 2\alpha)) + NF^R(1 - f^f)(1 - f_c)\epsilon_u^{\mathrm{eff}} - \\ & F^R(1 - f^f)f_c/2 \end{aligned} \tag{A.8}$$

$$\begin{aligned} d = \ & (1 - F^R)(1 - 2\alpha f^{**}/(1 + 2\alpha)) + NF^R(1 - f^f)(1 - f_c)\frac{\epsilon_m^{\mathrm{tag}}}{\epsilon_u^{\mathrm{tag}}}\epsilon_m^{\mathrm{eff}} - \\ & F^R(1 - f^f)f_c/2 \end{aligned} \tag{A.9}$$

where $\alpha = \frac{f_+ b_+}{f_0 b_0}$ and $\beta = \frac{b_+}{b_0}$.

Appendix B

Lepton Efficiency Calculation

The lepton efficiency correction involves four steps:

- Determine the primary lepton spectrum as a function of reconstructed momentum,
- Determine the efficiency for tracking and lepton identification as a function of reconstructed momentum,
- Multiply the spectra by the efficiency and then integrate the area between 1.4 GeV/c and 2.5 GeV/c,
- Apply additional correction factors.

B.1 Shape of primary lepton spectrum

First, the lepton spectrum is generated in the B meson rest frame using the model of ISGW with $D/D^{*}/D^{**}$ fractions of 24.5/54.5/21.0. This is done separately for electrons and muons.

Next, the spectrum is convoluted to include the effects of B motion at the $\Upsilon(4S)$. A weighted average of two different boosts are taken, corresponding to the beam energies of the `4S2` and `4S3` datasets. Recall that the neutral B semileptonic branching fraction measurement is based on the `4S1` through `4S5` datasets.

Thirdly, electroweak radiative corrections are applied to the spectrum according to the prescription of Marciano and Atwood[68]. The radiative correction factor $f_{\mathrm{EW}}(E_l)$ which multiplies the lepton spectrum is

$$f_{\mathrm{EW}}(E_l) = (\frac{E_{\max} - E_l}{C E_l})^r \tag{B.1}$$

where

$$r = \frac{2\alpha}{\pi}[\ln(\frac{2E_l}{m_l}) - 1] \tag{B.2}$$

and m_l and E_l are the lepton mass and energy. C is related to the average and maximum energies of the lepton through

$$C = (E_{\max} - \overline{E}_l)/\overline{E}_l. \tag{B.3}$$

After applying the radiative correction, the spectrum represents the momentum of primary leptons leaving the interaction point. More specifically, the spectrum has not yet been modified by either effects of bremsstrahlung in the detector material or by measurement resolution. These two effects are accounted for by constructing a nearly-diagonal smearing matrix with Monte Carlo using tagged leptons which maps generated momentum to the reconstructed momentum. The matrices for electrons and muons are shown in Figure B.1. Every column has unit area. The spectrum is then multiplied by the smearing matrix to produce the primary spectrum expressed as a function of reconstructed momentum, shown in Figure B.2. The discontinuities at 0.4 GeV/c for electrons and about 1.3 GeV/c for muons are due to the fact that the smearing matrices are defined to be diagonal below these momenta.

B.2 Determine efficiency for tracking and lepton ID

Next the efficiency to observe a lepton at a given reconstructed momentum is determined. This efficiency includes three contributions:

- The efficiency for the lepton track to enter the proper lepton fiducial region,
- The efficiency for DUET to reconstruct a lepton track and then for the track to pass quality cuts,
- The efficiency for the lepton track to pass lepton identification requirements.

The tracking efficiency as a function of generated lepton momentum, $\epsilon_{\rm TR}(\rm QQ)$, is defined to be the ratio of two spectra. The denominator of the ratio is the generated momentum spectrum of all generated leptons[1] with a generated cosine $P_z/P < 0.707$. The numerator is the generated momentum spectrum of all DUET tracks passing tracking cuts which are matched to a generated lepton by tagging subroutines, and with a generated cosine $P_z/P < 0.707$. Due to occasional tracking errors, it is possible to match multiple DUET tracks to a single generated lepton. This definition of the tracking efficiency includes this slight over efficiency. Figure B.3 shows $\epsilon_{\rm TR}(\rm QQ)$ for electrons and muons. This is the tracking efficiency as a function of generated momentum.

What is required is actually the tracking efficiency as a function of reconstructed momentum $\epsilon_{\rm TR}(\rm DUET)$. We make the approximation that

$$\epsilon_{\rm TR}(\rm DUET) \simeq \epsilon_{\rm TR}(\rm QQ) \tag{B.4}$$

---

[1] Here, the term generated lepton excludes leptons from gamma conversions and decays in flight.

which is the same approximation made by the analysis of the inclusive single lepton spectrum. To be exact, the efficiency $\epsilon_{\mathrm{TR}}(\mathrm{QQ})$ should be multiplied by the smearing matrices of Fig. B.1 to obtain $\epsilon_{\mathrm{TR}}(\mathrm{DUET})$. However, this detail is not necessary if the efficiency is sufficiently flat.

The lepton identification efficiency as a function of reconstructed lepton $\epsilon_{\mathrm{ID}}(\mathrm{DUET})$ is defined to be the ratio of two spectra. The denominator is the reconstructed momentum spectrum of all DUET tracks passing tracking cuts which are matched to a generated lepton by tagging subroutines with a reconstructed cosine $|\mathtt{CZCD}| < 0.707$. The denominator is the reconstructed momentum spectrum of the subset of these tracks which pass the lepton identification requirements. Figure B.4 shows $\epsilon_{\mathrm{ID}}(\mathrm{DUET})$ for electrons and muons.

The overall efficiency for tracking and lepton identification as a function of reconstructed momentum $\epsilon_{\mathrm{TR+ID}}(\mathrm{DUET})$ is the product of the two efficiencies $\epsilon_{\mathrm{TR}}(\mathrm{DUET})$ and $\epsilon_{\mathrm{ID}}(\mathrm{DUET})$, and is shown in Fig. B.5 for electrons and muons. Note that these efficiencies do not include the factor of 0.707 for the fiducial cut.

B.3 Multiply spectrum by efficiency

We multiply the spectra of unit area found in section A.1 by the (tracking + ID) efficiency from section A.2 to obtain the spectra in Fig. B.6. The area above 1.4 GeV/c is the efficiency to detect a primary lepton inside the fiducial region $|\mathtt{CZCD}| < 0.707$, and is found to be 0.443 for electrons and 0.368 for muons. Thus, the overall efficiencies for detecting a primary lepton after tracking, fiducial and PID cuts are equal to

$$\epsilon_e = 0.707 \times 0.443 = 0.313 \tag{B.5}$$

$$\epsilon_\mu = 0.707 \times 0.368 = 0.260. \tag{B.6}$$

B.4 Correction factors

Additional correction factors must be applied to the above efficiencies. As discussed in Section 5.6.3, these include corrections for the bias due to event selections, correction for the dilepton opening angle cut, and a correction for the bias due to tagging efficiencies. Table B.1 summarizes these correction factors. Table B.2 shows the overall efficiency corrections for each tag obtained by multiplying the results of section B.3 by the corrections in Table B.1.

Event Selection	0.995
Opening Angle	0.994
Tag Efficiency	1.030
Overall Correction	1.019

Table B.1: Correction factors to lepton efficiencies

ϵ_e	0.319
ϵ_μ	0.265

Table B.2: Efficiencies with all corrections

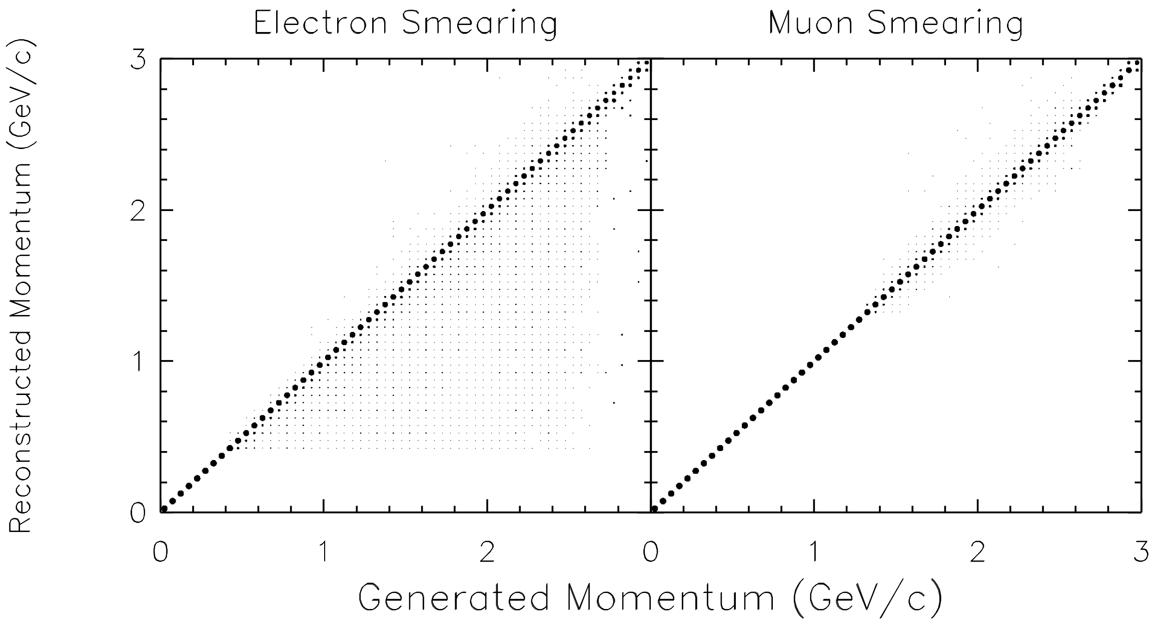

Figure B.1: Electron and muon momentum smearing matrices

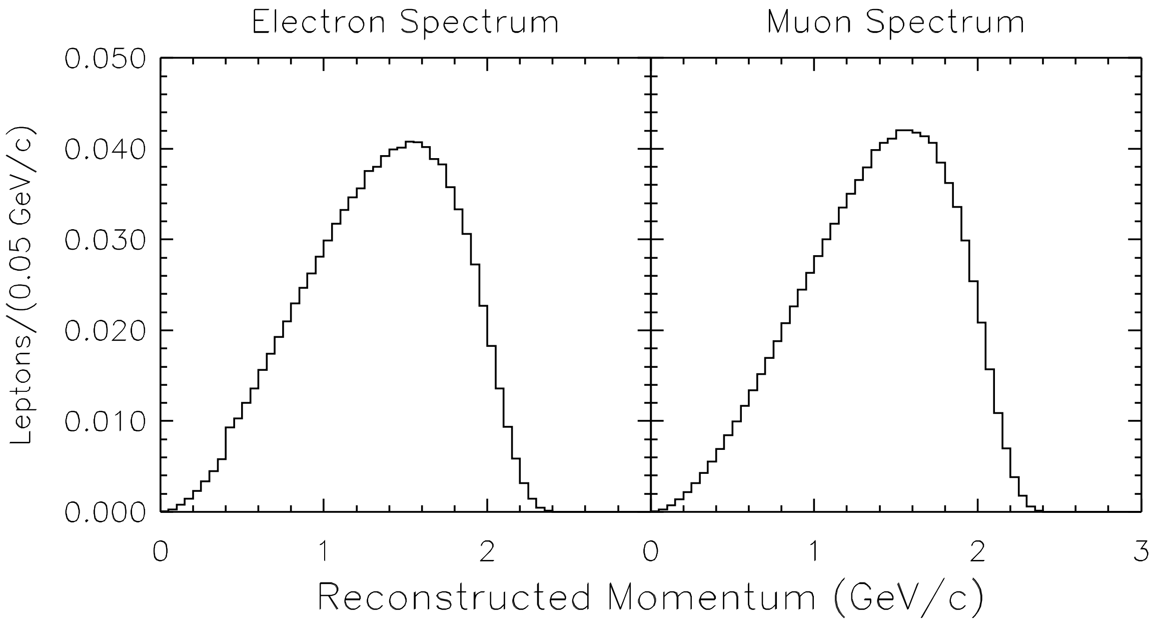

Figure B.2: Reconstructed momentum spectra for electron and muons in the ISGW model with 21% D^{**}.

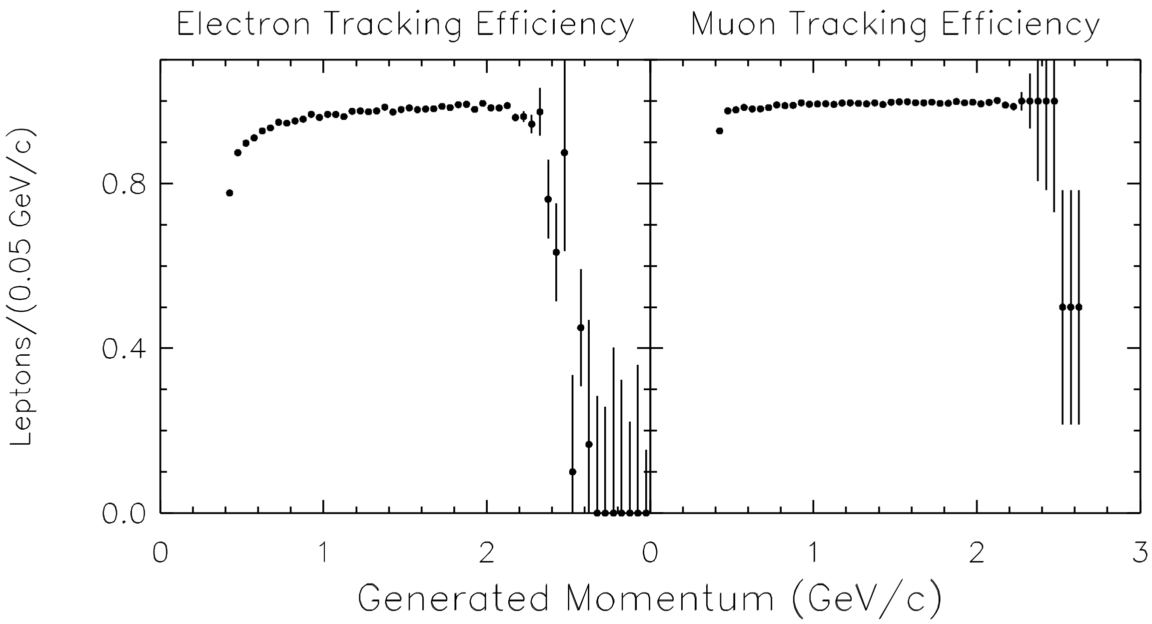

Figure B.3: Electron and muon tracking efficiencies

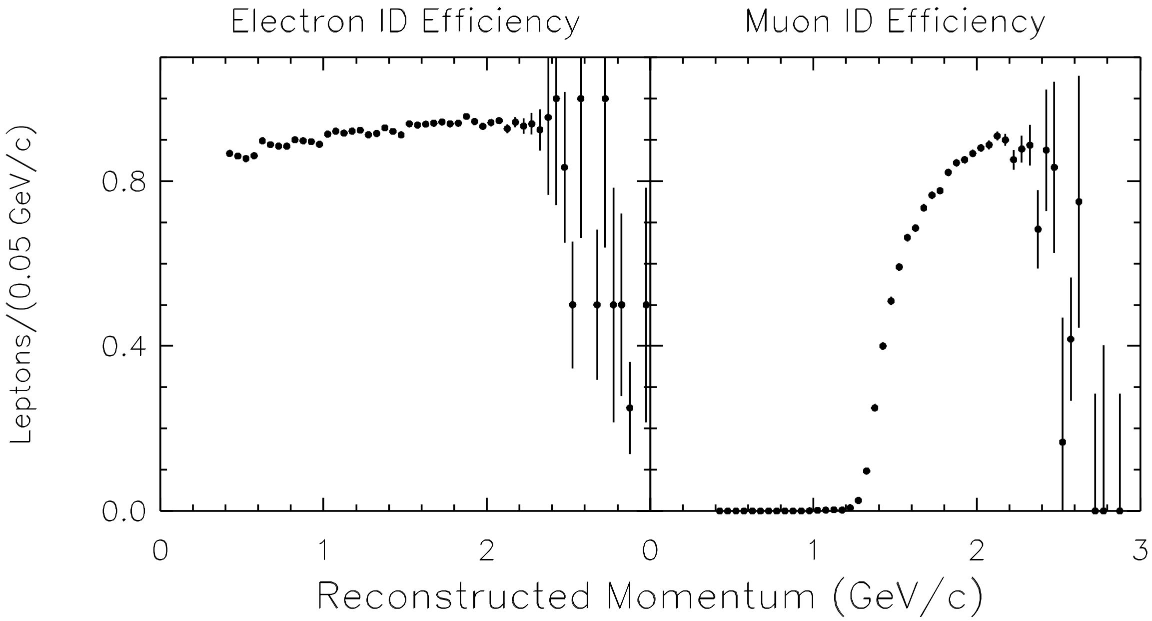

Figure B.4: Electron and muon identification efficiencies

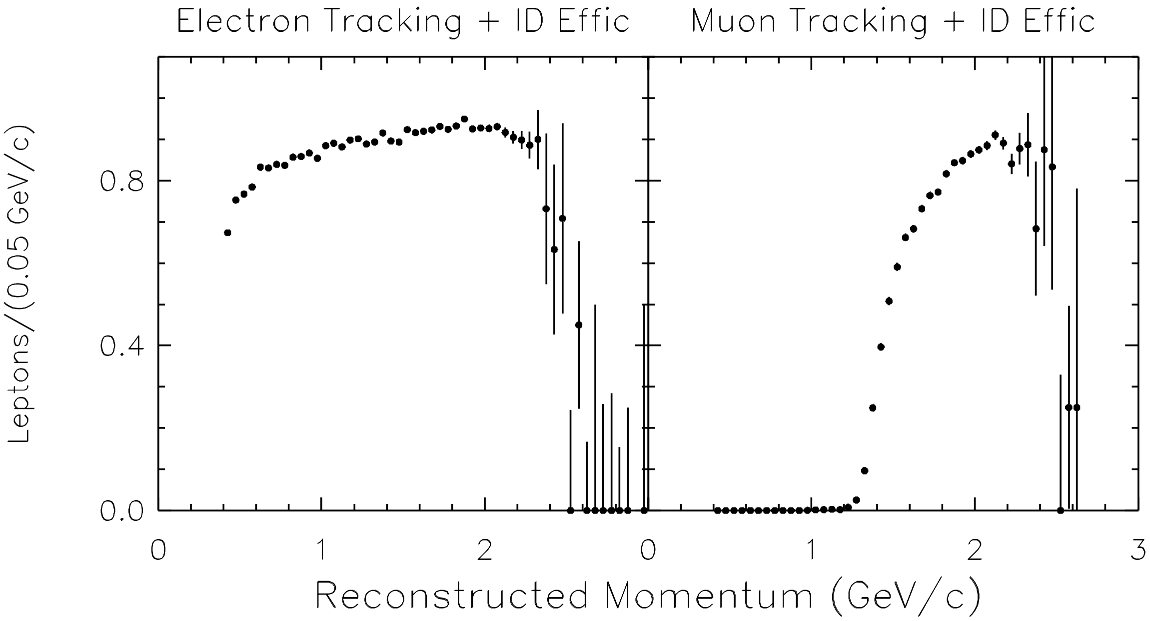

Figure B.5: Electron and muon tracking + identification efficiencies

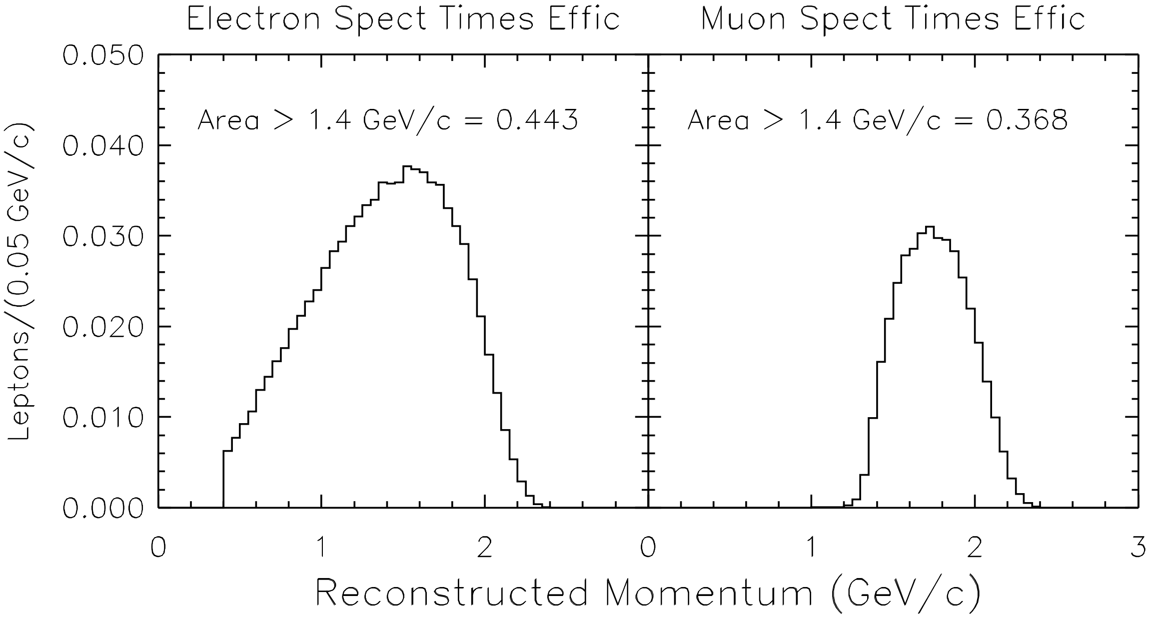

Figure B.6: Electron and muon spectra times (tracking + identification) efficiencies

Appendix C

CLEO Terminology

1. Datasets

Name	Dates	pb^{-1}	Comment
`4S1`	27May90-08Oct90	130	Included BB^* scan
`4S2`	11Nov90-04Jun91	672	Changed to Single Interaction Point
`4S3`	18Sep91-17Feb92	680	Installed DAQ90
`4S4`	10Apr92-26May92	318	DME gas in PTL
`4S5`	09Jul92-05Oct92	343	–
`4S6`	03Nov92-12Jan93	317	New RF cavities for CESR
`4S7`	16Mar93-06Jul93	461	–
`4S8`	01Aug93-27Sep93	274	–

2. Event

`NTRKCD`	number of charged tracks in CD (PT+VD+DR).
`R2GL`	Ratio of second to the zeroth Fox-Wolfram moments.

3. Track

`PQCD`	track momentum with electric charge as sign.
`CZCD`	$\cos\theta$ of track where z is beam axis.
`DBCD`	track impact parameter in $r-\phi$.
`ZOCD`	track impact parameter in $r-z$.
`RESICD`	RMS residual in tracking fitting.
`TRKMAN`	program to kill false tracks.
`KINCD`	general quality of track candidate, 0 — track from primary vertex, 2 — track from secondary vertex,
`IQALDI`	quality of dE/dx for a track, 1 — good, more than 11 hits.
`NHITPT`	number of hits in PT for a track.
`NHITVD`	number of hits in VD for a track.
`RHITDR`	pecentage of DR hits over expected for a track.

4. Lepton Identification

`R2ELEC`	likelihood for electron candidates.
`MUQAL`	quality of muon chamber hits matching CD track, 0 — good, match in all layers, 10K — fair, unsatisfactory match in one layer.
`DPTHMU`	depth of MU hits in unit of nuclear interaction length.

Appendix D

Comments on a B^- Tag

The neutral B tag used in this thesis is lepton/pion pair of opposite charge with $\widetilde{M}_\nu^2 \simeq 0$. It is worth noting that a charged B tag with a similarly high efficiency unfortunately *cannot* be made from a lepton/pion pair of the *same* charge with $\widetilde{M}_\nu^2 \simeq 0$, because the decay chain $B^- \to D^{*0}\ell^-\bar{\nu}$, $D^{*0} \to D^+\pi^-$ does not exist. In particular, energy conservation prevents D^{*0} from decaying to $D^+\pi^-$, as $(M_{D^+} + M_{\pi^-}) > M_{D^{*0}}$ by a mere 2.3 MeV/c^2.

However, a $\widetilde{M}_\nu^2$ tag made from combinations of ℓ^- and π^0 would be a linear combination of $\sim 2/3$ B^- and $\sim 1/3$ $\overline{B^0}$. Table D.1 shows the five possible decay modes of $B \to D^*\ell\overline{\nu}$ with the D^* branching fractions. Unfortunately, unlike the $\overline{B^0}$ tag, there is no incorrect, or "wrong-sign", way to pair the leptons and π^0.

One application for a ℓ/π^0 tag would be in the determination of f_+/f_0. The quantity f_0 (and thus f_+) can be measured by comparing the rate of events with a single ℓ^-/π^+ tag with rate for double tagged events. As an independent check, one could use single versus double ℓ/π^0 tags, for example, to also arrive at a value of f_+/f_0.

$\overline{B^0} \to D^{*+}\ell^-\overline{\nu}$	$D^{*+} \to D^0\pi^+$	68%
	$D^{*+} \to D^+\pi^0$	31%
	$D^{*+} \to D^+\gamma$	1%
$B^- \to D^{*0}\ell^-\overline{\nu}$	$D^{*0} \to D^0\pi^0$	64%
	$D^{*0} \to D^0\gamma$	36%

Table D.1: Decay modes of $B \to D^*\ell\overline{\nu}$

List of References

[1] M. Kobayashi and T. Maskawa, Prog. Theor. Phys. **49** (1973) 652.

[2] L. Wolfenstein, Phys. Rev. Lett. **51** (1983) 1945.

[3] Particle Data Group, K. Hikasa *et al.*, Review of Particle Properties, Phys. Rev. **D50** (1994) 1315.

[4] D. Andrews *et al.* (CUSB), Phys. Rev. Lett. **44** (1980) 1108.

[5] S. Okubo, Phys. Lett. **5** (1963) 165;
G. Zweig, CERN Reps. TH-401 (1964) 412 ;
J. Iizuka, Suppl. Prog. Theor. Phys. **37-38** (1966) 21.

[6] M. Gell-Mann and A. Pais, Phys. Rev. **97** (1955) 1387.

[7] K. Lande *et al.*, Phys. Rev. **105** (1957) 1925.

[8] Anjos *et al.*, Phys. Rev. Lett. **60** (1988) 1239.

[9] H. Albrecht *et al.* (ARGUS), Phys. Lett. **192B** (1987) 245.

[10] D. Buskulic *et al.* (ALEPH), Phys. Lett. **311B** (1993) 425.

[11] A.J. Buras, W. Slominski and H. Steger, Nucl. Phys. **245B** (1984) 369.

[12] P. Bouchaud *et al.*, Phys. Rev. **D41** (1990) 3541.

[13] F. J. Gilman and M. B. Wise, Phys. Rev. **D27** (1983) 1128.

[14] M. I. Vysotzki, Sov. J. Nucl. Phys. **31** (1980) 797.

[15] A. J. Buras, M. Jamin and P. H. Weisz, Nucl. Phys. **347B** (1990) 491.

[16] C. Bernard, J. Labrenz and A. Soni, Phys. Rev. **D49** (1994) 2356.

[17] R. M. Baxter *et al.* (UKQCD), Phys. Rev. **D49** (1994) 1594.

[18] C. Alexandrou, S. Guesken, F. Jegerlehner, K. Schilling and R. Sommer, Z. Phys **C62** (1994) 659.

[19] A. Abada *et al.*, Nucl. Phys. **376B** (1992) 172.

[20] S. Hashimoto, HUPD-9403, March 1994; Nucl. Phys. **B34** (1994) 441.

[21] A. Duncan, E. Eichten, J. Flynn, B. Hill, G. Hockney and H. Thacker, FERMILAB-PUB-94/164-T, July 1994.

[22] C. R. Allton *et al.* (APE), ROME Preprint 94/981.

[23] CLNS 95-1331, CLEO 95-5.

[24] T. Browder and K. Honscheid, Preprint UH 511-816-95.

[25] D. Acosta *et al.* (CLEO), Phys. Rev. **D49** (1994) 5690.

[26] N. Cabibbo and N. Maiani, Phys. Lett. **79B** (1978) 109.

[27] M. Suzuki, Nucl. Phys. **145B** (1978) 420.

[28] C. Quigg and J. Rosner, Phys. Rev. **D19** (1979) 1532.

[29] G. Altarelli and L. Maiani, Phys. Lett. **52B** (1974) 351.

[30] M. K. Gaillard and B. W. Lee, Phys. Rev. Lett. **33** (1974) 108.

[31] A. J. Buras, J. M. Gerard and R. Rückl, Nucl. Phys. **268B** (1986) 16-26.

[32] B. Blok and M. A. Shiftman, Yad. Fiz. 45: 211, 478, 841 (1987), and ITEP Reports 9, 17, 37 (1986).

[33] G. Altarelli and G. Petrarca, Phys. Lett. **61B** (1991) 303.

[34] I. Bigi, N. Uraltsev, A. Vainshtein, Phys. Lett. **293B** (1992) 430;(E) **297B** (1993) 477.

[35] B. Blok, M. Shifman, Nucl. Phys. **399B** (1993) 441.

[36] I. Bigi, B. Block, M. Shifman and A. Vainshtein, Phys. Lett. **323B** (1994) 408.

[37] G. Altarelli, N. Cabibbo, G. Corbo, L. Maiani, and G. Martinelli, Nucl. Phys. **208B** (1982) 365.

[38] A. Ali, Zeit. Phys. **C1** (1979) 25.

[39] N. Isgur, D. Scora, B. Grinstein and M. Wise, Phys. Rev. **D39** (1989) 799.

[40] I. I. Bigi, in *The Fermilab Meeting DPF92,* C. Albright, P. Kasper, R. Raja and J. Yoh, eds. (World Scientific, Singapore, 1992), p.610.

[41] Y. Kubota *et al.*, Nucl. Instrum. Methods **A320** (1992) 66.

[42] R. Wang, *"Measurements of the Inclusive Semileptonic Branching Fraction of B Mesons at the Upsilon(4S) Resonance"*, Ph.D. Thesis, University of Minnesota (1994).

[43] H. Albrecht *et al.*(ARGUS Collaboration), Phys. Lett. **324B** (1994) 249.

[44] G. Fox and S. Wolfram, Phys. Rev. Lett. **41** (1978) 1581.

[45] A hadronic event must contain at least 3 well-fitted charged tracks, have a measured energy of at 0.15 times the center-of-mass energy and have an event vertex consistent with the known e^+e^- interaction point.

[46] D. Bortoletto, *"Exclusive and Inclusive Semileptonic Decays of the B Meson"*, Ph.D. Thesis, Syracuse University (1989).

[47] M. Bauer and M. Wirbel, Z. Phys. **C42** (1989) 671.

[48] J. Bartelt *et al.* (CLEO), Phys. Rev. Lett. **71** (1993) 1680.

[49] Akers *et al.* (OPAL), Phys. Lett. **327B** (1994) 411.

[50] F. Abe *et al.*, FERMILAB-PUB-95/022-E, February 1995.

[51] J. Bartelt *et al.* (CLEO), Phys. Rev. Lett. **71** (1993) 4111.

[52] A. Khodjamirian, S. Rudaz and M. Voloshin, Phys. Lett. **242B** (1990) 489.

[53] S. Henderson *et al.* (CLEO), Phys. Rev. **D45** (1992) 2212.

[54] H. Albrecht *et al.* (ARGUS), Phys. Lett. **249B** (1990) 359.

[55] At the time this analysis was performed, the fit to the CLEO II inclusive lepton spectrum indicated a D^{**} fraction of 21%. More recently, CLEO's final fit to the spectrum indicates a slightly higher D^{**} fraction of 23%. This difference has a small effect on the results presented herein.

[56] R. Fulton *et al.* (CLEO), Phys. Rev. **D43** (1991) 651.

[57] H. Albrecht *et al.* (ARGUS), Phys. Lett. **232B** (1989) 554.

[58] M. Athanas *et al.* (CLEO), Phys. Rev. Lett. **73** (1994) 3503;(E) **74** (1995) 3090.

[59] 1994 Meeting of International Conference on High Energy Physics, Glasgow Scotland, Ref. 0579.

[60] 1994 Meeting of the Divsion of Particles and Fields, Albuquerque NM.

[61] F. Abe *et al.* (CDF), Phys. Rev. Lett. **72** (1994) 3456.

[62] D. Busculic *et al.* (ALEPH), Phys. Lett. **298B** (1993) 479.

[63] M. Battle *et al.* (CLEO), Phys. Rev. Lett. **71** (1993) 3922.

[64] R. Ammar *et al.* (CLEO), Phys. Rev. Lett. **71** (1993) 674.

[65] I. Bigi, B. Blok, M. Shifman, A. Vainshtein, Preprint CERN-TH.7082/93.

[66] E. Bagan, P. Ball, V. M. Braun, P. Gosdzinsky, Preprint UAB-FT-347/R.

[67] E. Bagan, P. Ball, B. Fiol, P. Gosdzinsky, Preprint UAB-FT-360.

[68] D. Atwood and W. Marciano, Phys. Rev. **D41** (1990) 1736.